The Dissertation Committee for Karl Joseph Kreder III Certifies that this is the approved version of the following dissertation:

Synthesis and electrochemical characterization of novel electroactive materials for lithium-ion batteries

Committee:

Arumugam Manthiram, Supervisor

John B. Goodenough

Guihui Yu

Gyeong S. Hwang

Paulo J. Ferreira

Synthesis and electrochemical characterization of novel electroactive materials for lithium-ion batteries

by

Karl Joseph Kreder III

Dissertation

Presented to the Faculty of the Graduate School of
The University of Texas at Austin
in Partial Fulfillment
of the Requirements
for the Degree of

Doctor of Philosophy

The University of Texas at Austin

August 2017

Acknowledgements

Firstly, I would like to thank all members of the Manthiram research group whom I have worked with over the past 5 years. Specifically, I would like to thank Dr. Zachary Moorehead-Rosenberg, Dr. Arturo Gutierrez, Dr. James Knight, Dr. Michael Kline, Guarav Assat, and Brian Heligman. Specifically, I would like to acknowledge Dr. Michael Kline for his assistance with both Transmission Electron Microscopy (TEM) energy dispersive X-ray (EDS) experiments seen in both Chapters 5 and 6. I would like to thank Guarav Assat for his help with the work on $LiCoPO_4$ cathodes presented in chapters 3 and 4. Finally, I would like to thank Brian Heligman for his help with the work presented in chapter 7.

I would also like to thank my supervisor, Arumugam Manthiram, my professors, and my committee for providing education and guidance to enable me to be a successful researcher. Professor Manthiram has been a superb advisor, both with his guidance and practical approach to solving difficult problems, and also the degree of autonomy he allowed me in pursuing new ideas. The professors at the University of Texas have also provided me with the formal education that I needed to successfully push forth the state-of-the-art research into batteries and electrochemistry. Specifically, I would like to acknowledge the late Llewellyn Rabenberg, for whom I was a teaching assistant. My work with him creating an undergraduate lab on copper-silver eutectic alloys was a key inspiration for conceptualizing the work presented in chapter 7. Finally, I would like to acknowledge each of my committee members for their guidance in my research, specifically, Dr. Arumugam Manthiram, Dr. John B. Goodenough, Dr. Guihui Yu, Dr. Gyeong S. Hwang, and Dr. Paulo J. Ferreira.

I would also like to recognize the various funding sources that made this work possible. The work in Chapters 3 & 4 was funded by office of Vehicle Technologies of the U.S. Department under the BATT program. The work in Chapters 5, 6 & 7 was

funded by the U.S. Department of Energy, Office of Basic Energy Sciences, Division of Materials Sciences. Additionally, I would like to recognize the Cockrell School of Engineering for providing me a Doctoral Fellowship, specifically the Virginia and Earnest Cockrell, Jr. Fellowship. This was instrumental in helping me have the financial resources possible to attend graduate school.

Lastly, I would like to express my eternal gratitude to my wife and family for both their financial and emotional support over the past 5 years of graduate school. I am grateful for the opportunity they gave me to return to school and continue my education.

Synthesis and electrochemical characterization of novel electroactive materials for lithium-ion batteries

Karl Joseph Kreder III, Ph.D.

The University of Texas at Austin, 2017

Supervisor: Arumugam Manthiram

Lithium-ion batteries (LIBs) have become ubiquitous as energy storage devices for mobile electronics, electric vehicles, and are beginning to be used for electric grid-scale energy storage. Lithium-ion batteries offer higher efficiencies, energy density, and longer life compared to incumbent technologies such as lead-acid and nickel metal hydride. Applications in which LIBs are used are continuing to demand better performing batteries at lower cost, which requires improvement in electroactive materials. This dissertation investigates the low temperature synthesis and modification of $LiCoPO_4$ as a potential high-voltage and therefore higher energy density polyanion cathode material for LIBs, as well as a new class of interdigitated metal foil anodes which promises to be an inexpensive, higher energy density, alternative to graphite.

Chapter 1 is a brief introduction to lithium-ion batteries and the principle of operation of intercalation type electrochemical energy storage devices. The components of lithium ion batteries are introduced, specifically the anode, cathode, separator, and electrolyte. Some of the shortfalls of the current technologies are discussed and areas of research interest are highlighted.

Chapter 2 is a brief overview of the various experimental methods that are generally applicable to more than one of the subsequent chapters. Methods which are specific to a given study are discussed in their respective chapters.

Chapter 3 presents work on the low temperature microwave-assisted solovthermal synthesis (MW-ST) of three unique polymorphs of $LiCoPO_4$, specifically the polymorphs belonging to the *Pnma*, *Cmcm*, and *$Pn2_1a$* space groups. Prior to this work, only the *Pnma* polymorph had been reported via MW-ST method, and electrochemistry had not yet been reported for either the *$Pn2_1a$* or *Cmcm* polymorph. The dependence of the polymorphs on both the water content, and ammonium hydroxide content of the solvent was shown. Although, the electrochemistry of both the *$Pn2_1a$* and *Cmcm* polymorphs was found to be inferior to the *Pnma* polymorph, the ability to synthesize phase pure materials was crucial to conducting the work presented in chapters 4 and 5.

Chapter 4 presents the aliovalent substitution of V^{3+} for Co^{2+} in LiCoPO4 via a low-temperature MW-ST process. Substitution of up to 7% vanadium for cobalt was demonstrated and verified by changes in the lattice parameters with vanadium content. Both the ionic and electronic conductivity of $LiCoPO_4$ was enhanced with increasing vanadium substitution, which was attributed to the introduction of both charge carriers as well as inter-tunnel cobalt vacancies. Finally, the first cycle capacity was enhanced (from 69 mAh/g to 115 mAh/g) as well as the capacity retention over cycling.

Chapter 5 demonstrates a novel technique of MW-ST assisted coating of a thin (2-5nm) conformal coating of $LiFePO_4$ on vanadium substituted $LiCoPO_4$. Although the vanadium substitution was able to independently increase the performance of $LiCoPO_4$, the materials still suffers from severe side reactions with the electrolyte. The coating of $LiFePO_4$ effectively raises the Fermi energy of the cathode material above the high occupied molecular orbital (HOMO) of the electrolyte preventing side reactions and increase the coulombic efficiency to nearly 100%.

Chapter 6 introduces a novel method of producing high surface area, electrically conductive, metal nanofoams via a MW-ST process. Nickel, copper, and silver metal nanofoams are made via an inexpensive yet scalable process whereby metal acetates are reduced by polyglycol under microwave irradiation. The nanofoams were characterized via BET, SEM, XRD, EDS, and TEM. The nanofoams have potential uses in many clean energy applications, particularly lithium-ion batteries.

Chapter 7 introduces a new framework for making a new class of high capacity, low-cost alloying anodes for lithium ion batteries. A novel interdigitated metal foil anode (IMFA) in which a nanosized active material, such as tin, is interdigitated with an electrically conductive matrix, such as aluminum, is presented. The foils are formed by the rolling of a eutectic Al-Sn alloy into a foil, which is an extremely cheap and scalable process. The anodes demonstrate an approximately 70% increase in capacity compared to graphite over 100 cycles, at reasonably fast rates (C/5), and high coulombic efficiency (>99%).

Finally, Chapter 8 gives a brief overview of the results of the prior work and proposes areas for future research.

Table of Contents

List of Figures

List of Tables

Chapter 1: Introduction

1.1 Motivation

The rising costs of fossil fuels and greater concern for the environmental impact of using carbon-based sources of energy have led to extensive research into alternative forms of energy, including nuclear, wind, solar, and hydroelectric. The rise of alternative forms of energy generation requires new energy storage technologies to fully take advantage of these resources.[1] The proliferation of mobile computing over the last 20 years was enabled by the high energy density, high power density, and long cycle life of lithium ion batteries (LIBs). Lithium ion batteries provide significant advantages over the previous conversion energy storage technologies, such as lead-acid and nickel metal hydride (NiMH). LIBs have both higher voltages enabled by non-aqueous electrolytes as well as the intrinsic advantage of intercalation reactions compared to conversion reactions.[2,3] The normalized cost of using a lithium ion battery to store energy over its life is better than other technologies and is quickly approaching the point where it is cost effective to use in both transportation as well as electrical grid scale storage.[4]

1.2 Lithium-ion Battery

A lithium ion battery is compromised principally of four different components, namely the cathode, the anode, the electrolyte, and the separator. During operation lithium ions are shuttled via the electrolyte from the anode to cathode during discharge and the cathode to anode during charge. Simultaneously, electrons, whose electrical potential is dictated by the difference in chemical potential between the anode and cathode, flow through an external circuit performing useful work. During discharge electrons are liberated by an oxidative change of state of a transition metal, M, from M^{+x} to M^{+x+1}, while there is a simultaneous reduction reaction at the anode. The principal benefit of lithium ion batteries over prior battery chemistries is the oxidation and reduction reactions take place through a process called intercalation rather than conversion. Intercalation is arguably the biggest driver of the dramatic increase in cyclability achieved in lithium ion chemistries relative to incumbent technologies. Specifically, during intercalation reactions the crystal structure of the electroactive

material is maintained while lithium ions are inserted and removed from the lattice. In contrast, conversion type electroactive materials do not maintain a consistent crystal structure but rather undergo chemical interconversion from metal to metal oxides, metal hydroxides, or metal sulfates. The process of chemical conversion causes the electrode to lose integrity over time (known as shedding in lead acid batteries), which in turn causes the loss of active material and an increase in internal cell impedance ultimately leading to capacity loss and eventually failure.[5]

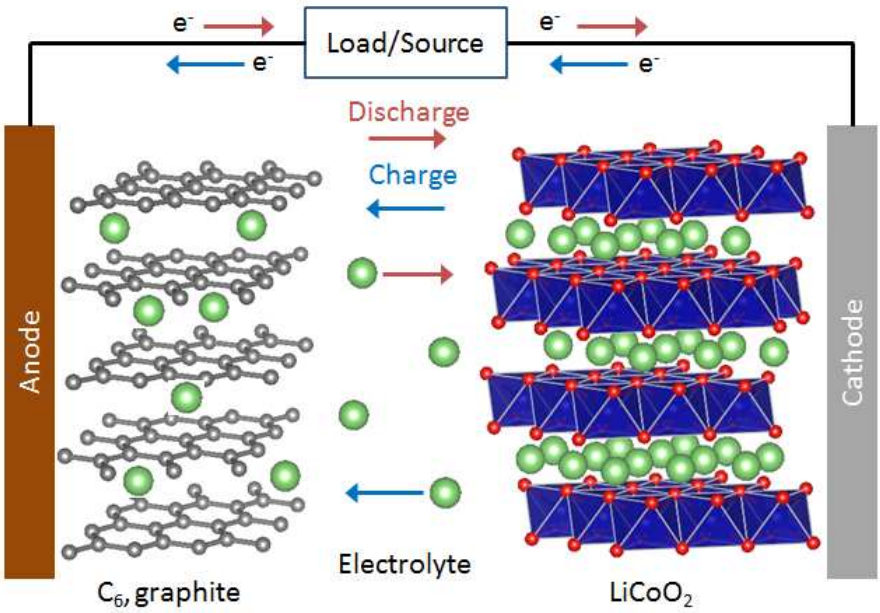

Figure 1.1. Illustration of the operation of a typical lithium ion battery

The process of intercalating lithium ions without conversion reactions is known as a rocking chair battery and is illustrated in

Figure 1.1.[6] In addition to the reversibility achieved by intercalation reactions, lithium ion batteries performance also benefits from the use of non-aqueous electrolytes. Non-aqueous electrolytes have a larger window of electrochemical stability compared to aqueous electrolytes. The stability is dictated by the bandgap between the highest occupied molecular orbital (HOMO) and the lowest un-occupied molecular orbital (LUMO), shown in Figure 1.2.[7]

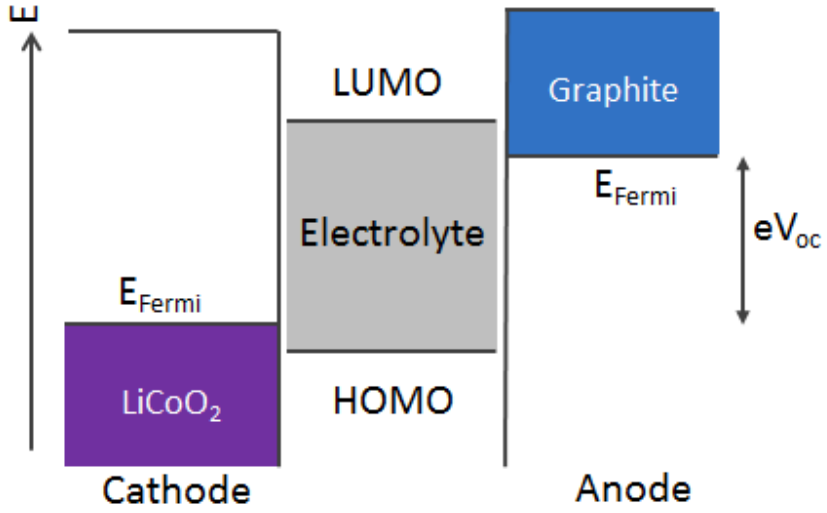

Figure 1.2. Illustration of the electrochemical requirements for creating a compatible cathode/anode/electrolyte system.

This enables lithium ion batteries to have a higher operating voltage which intern increases both the gravimetric and volumetric energy densities.

1.3 Cathode Materials

Stanley Whittingham introduced the first intercalation cathode material TiS_2 in 1974 while working at Exxon's Corporate Research Laboratories.[8] Although this was the first demonstration of an intercalation compound for an energy storage device, it suffered from major safety problems which prevented commercialization. TiS_2 does not contain lithium atoms so they must be introduced from an outside source to discharge the battery. At the time the only known anode to work with TiS_2 was lithium metal which suffered from dendritic growth during charge causing safety concerns.[9–11] Subsequently, in 1981 John Goodenough introduced layered lithium cobalt oxide ($LiCoO_2$), a lithium containing cathode material, which did not have to be paired with a metallic lithium anode.[12] Lithium cobalt oxide still serves as an archetype for what defines a good cathode material, namely that it contains lithium, has an open structure that reversibly intercalates lithium,

has a high electrochemical potential relative to lithium, has high electronic conductivity, high ionic conductivity, and is thermally stable. Since the introduction of $LiCoO_2$, there have been a number of new materials discovered. However, the commercially viable cathode materials all fall within three broad structural groups, specifically, layered, olivine, and spinel. The prototypical material for each one of these systems is $LiCoO_2$, $LiFePO_4$, and $LiMn_2O_4$, respectively.[13–15] Interestingly the number of dimensions through which lithium can diffuse is 1D, 2D, 3D for the olivine, layered, and spinel structures, respectively.

1.3.1 Olivine ($LiMPO_4$) cathodes

Lithium metal phosphate cathodes, $LiMPO_4$ (M = Fe, Mn, Co, Ni), take on what is known as the ordered olivine structure.[16–25] The polymorph which has the best electrochemical performance belongs to the *Pnma* space group. In this structure, the transition metal is found in the 3^+ ($M^{3+}PO_4$) when charged and in the 2^+ ($LiM^{2+}PO_4$) when discharged. The phosphate has a 5^+ charge and is tetrahedrally coordinated by 4 oxygen atoms, while the transition metal atom is octahedrally coordinated by 6 oxygen atoms. Lithium diffusion in the olivine structure is only able to happen in 1-dimension along the b-axis as seen in Figure 1.3. Lithium diffusion can be further hampered by sarcopside defects which is when an M atom moves into the Li position blocking diffusion in the channel.[26]

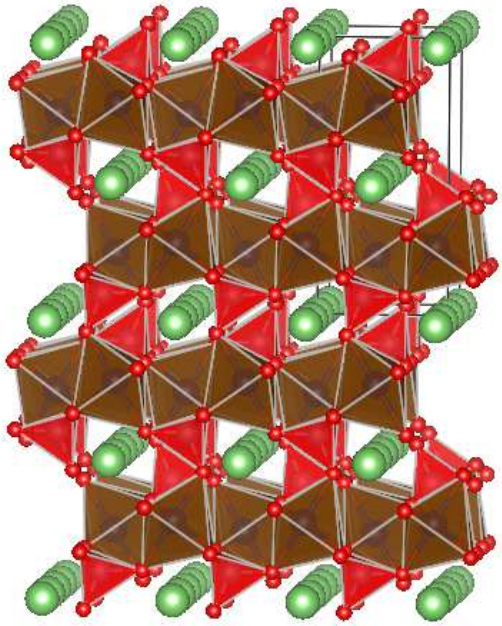

Figure 1.3. Lithium metal phosphate (LiMPO4) structure, showing the lithium diffusion channels along the b-axis.

In addition, to the problems with lithium ion diffusion in the olivine structure, the electrical conductivity is much lower compared to the metallic like conduction observed in $LiCoO_2$. Unlike $LiCoO_2$ metal phosphates have low electronic conductivity on the order of 10^{-9}.[27] Finally, $LiMPO_4$ also undergoes significant volume change (~7%) during cycling which can lead to electrochemical milling of the material.[28] Fortunately, all of these problems can be addressed, at least for $LiFePO_4$, through both nano-sizing particles, which increases ionic conductivity and prevents electrochemical milling, and carbon coating which increase electrical conductivity.[16,29,30]

Although, nano-sized $LiFePO_4$ has had tremendous commercial success as a high-power low-cost cathode material, it suffers from lower energy density compared to the layered cathodes, partly due to its lower potential (~ 3.4 V). The $LiMPO_4$ materials where M = Mn, Co, Ni have higher $2^+/3^+$ redox potentials of 4.1, 4.8, 5.2 V, respectively, which leads to proportionally higher energy densities. While $LiNiPO_4$ has the highest potential and therefore theoretical energy density, it is not a good candidate for research because its potential is outside the stability window of known non-aqueous carbonate electrolytes.[31] Both $LiMnPO_4$ and $LiCoPO_4$ are promising candidates for further research

and optimization focused on overcoming their lower ionic/electronic conductivity, as well as instabilities with the electrolyte experienced at higher voltages.

1.4 Anode Materials

The introduction of graphite as an intercalation anode in the 1990's by both Sony and Moli cell enabled the commercialization of the lithium ion battery.[32–34] Graphite anodes offer both high energy density, low cost and long cycle life and are material of choice in commercial cells today. During charging of a lithium ion battery lithium ions from the cathode are inserted into graphite to form Li_xC_6 at a potential of ~100 mV. The theoretical gravimetric energy density of graphite is 372 mAh/g however; it has a relatively low tap density of ~ 1 g/cm3.[35]

Although the electrochemical potential of graphite is well above the LUMO of most electrolytes, the serendipitous formation of a meta-stable layer known as the solid-electrolyte-interphase (SEI) enables stable cycling.[36–38] The SEI layer enables cycling but is only meta-stable, therefore it continues to react with the electrolyte over-time leading to capacity fade and increase in cell impedance.[38] Additionally, when graphite is charged at very high rates, the over polarization at the anode causes the formation of lithium metal which causes dendrites potentially leading to catastrophic cell failure. The formation of dendrites is mitigated if the electrochemical potential of a given anode material is higher than that of lithium (~3.05 V vs. SHE). Even though graphite meets these criteria under static/low-rate operation, a material which has a slightly higher potential would provide a greater safe operating margin particularly at high rates and low temperatures.[39]

1.4.1 Alloying Anodes

Alloying anodes are a promising area of research because they have dramatically increased theoretical gravimetric and volumetric energy densities compared to graphite. There are a number of known lithium alloying materials which generally belong to the late transition metal series and metalloids including: Si, Ge, Al, Sn, Pb, Sb, Bi, Zn, Cd, Ag.[40] All of these materials have 1 or more voltage plateau's which are higher than

graphite meaning they can potentially be used to make safer anodes. The most promising materials are Si, Sn, and Sb which have theoretical energy densities of 3579, 960, and 660 mAh/g, respectively.[41] The lower voltage plateaus where Si, Sn, and Sb derive most of their capacity are 0.2, 0.4, and 0.78 V, respectively. These alloying potentials are significantly higher than the 100 mV at which lithium intercalates into graphite, meaning that the alloying materials are less prone to undergo lithium plating. There are a number of known challenges posed by the alloying materials in a practical lithium ion battery, including low first cycle coulombic efficiencies, low lithium ion diffusion rates, and large volume change during cycling.[42] There have been a number of strategies devised to address these well-known problems. Nanosizing of the active material allows the particles to undergo a greater amount of volume change without electrochemical milling and therefore prevents rapid capacity fade. The strategy of nanosizing has been further enhanced by the use of electrically conducting coatings or additives such as carbon black, carbon nanowire, or graphene.[43–46] The purpose of the conductive additives seems to be to prevent the loss of electrical contact of the active alloying material with cycling. Nanosizing also addresses the low rate capabilities of the alloying materials caused by poor diffusion kinetics.[47] Another strategy that has been successfully employed with alloying anodes is the addition of an buffer matrix.[48] The buffer materials often include reactive intermetallic phases and/or non-active materials. Although there have been numerous strategies and combinations thereof to improve the performance of lithium alloying materials, none to date have been practical enough to have met commercial success.

1.5 Objectives

The primary objective of this research is to increase the gravimetric energy density of lithium ion batteries via novel cathode and anode systems. The secondary objectives being to increase the cycle life, safety, efficiency, while decreasing cost. Although, the primary objective is the most challenging in lithium ion battery research today, it cannot be taken by itself, and must be considered holistically with the other metrics. The first half of this work focuses on increasing the energy density of the cathode through the

modification of the solid state properties of $LiCoPO_4$. The second half of this work focuses on the development of novel anode architectures which have higher energy density and are cheaper compared to graphite.

The second chapter focuses on the MW-ST synthesis of phase pure $LiCoPO_4$ at low temperatures to enable the work of modification of $LiCoPO_4$ presented in the subsequent 2 chapters. Although there has been extensive work on $LiMPO_4$ cathodes, prior to this work, the non-olivine polymorphs via MW-ST synthesis had not been reported. Three polymorphs of $LiCoPO_4$ belonging to space groups *Pnma, Cmcm,* and $Pn2_1a$ are reported. Synthesis conditions for producing phase pure materials of each one of the polymorphs are presented.

The third chapter looks to enhance the electrochemical performance of $LiCoPO_4$, by modifying the solid state properties through aliovalent substitution of V^{3+} for Co^{2+}. $LiCoPO_4$ has yet to achieve the theoretical density of 167 mAh/g. Increasing both the electrical and ionic conductivity of $LiCoPO_4$ should increase the practical capacity while also decreasing the amount of polarization allowing cycling at higher rates. Low temperature MW-ST synthesis is key to producing phases of materials which would not otherwise be stable at higher temperatures.

The electrochemical potential of $LiCoPO_4$ is ~ 4.8 V which readily causes the breakdown of carbonate electrolytes via side reactions with the cathode during charge. These side reactions can be so severe that the reported coulombic efficiencies for $LiCoPO_4$ cathodes are routinely ~90%. Adding a coating to the surface of the $LiCoPO_4$ which lowers the electrochemical potential of the cathode interface with the electrolyte may be one approach to mitigating side reactions. A low temperature MW-ST method of conformal coating $LiCoPO_4$ nanoparticles is explored in chapter 5.

Recently there have been a number of attempts to make high rate batteries, lithium metal anodes, and alloying anodes which have leveraged the use of nanoscale conducting metal substrates. The biggest drawback to these approaches is the relative expense and complexity involved in making the substrate. In chapter 6 a novel inexpensive MW-ST method of forming metal nanofoams is explored.

Although, a nanoscale conductive matrix can demonstrate marked improvement in the cycling of both lithium metal anodes and alloy anodes, there are a number of practical drawbacks, beyond cost, which would inhibit their commercial implementation. Specifically, the mechanical handling of materials that would easily shed metal particles would be impossible to work with in a battery factory at scale. Any small metal particle introduced to the cell could potentially puncture the separator causing a catastrophic short. Therefore, a new framework for forming interdigitated metal foil anodes which addresses many of these issues is explored in chapter 7.

Finally, chapter 8 summarizes the results of the work discussed in chapters 3 through 7 and briefly outlines areas for continued work.

Chapter 2: Experimental Methods

2.1. Materials Characterization

2.1.1. X-ray Diffraction

Powder X-ray diffraction (XRD) patterns were recorded with a Bragg-Brentano type diffractometer (Rigaku Miniflex 600) with copper $K\alpha_1$ radiation (λ = 1.4505 Å) in continuous mode over various ranges of 2θ at different rates. Typical ranges of scanning were from 0 – 100^o 2θ at rates ranging from 1- 4 degrees per minute. The XRD patterns were analyzed by Rietveld refinement using the Fullprof software.

2.1.2. Scanning Electron Microscopy

Scanning electron micrographs (SEM) were recorded with a JEOL JSM-5610 instrument at 20 keV accelerating voltage after sputter coating the samples with gold. Powdered SEM samples were prepared by dispersing the powder on carbon tape either mechanically or via a suspension of the materials in isopropanol. Non-powdered samples were prepared by manual sectioning and mounting on carbon tape.

2.1.2.1. Energy Dispersive X-Ray Spectroscopy

Energy dispersive spectroscopy (EDS) was performed on the JEOL JSM-5610 with an Oxford Instruments detector while operating in the scanning transmission electron microscopy (STEM) mode. Composite EDS maps were generated by using Matlab software's image processing to combine the various elemental maps into a single image.

2.1.3. Transmission Electron Microscopy

The transmission electron microscopy (TEM) was carried out with a JEM-2100F microscope with an accelerating voltage of 200 kV. The energy dispersive x-ray spectroscopy (EDS) was performed with the JEM-2100F microscope equipped with an Oxford Instruments EDS detector while operating in the scanning transmission electron microscopy mode. The samples were prepared by making a dilute suspension of powder in isopropanol and dropping it on a copper grid with carbon lace.

2.1.4. Inductively Coupled Plasma Optical Omission Spectroscopy

Inductively coupled plasma optical emission spectroscopy (ICP-OES) was carried out on a Varian 715-ES to determine the precise stoichiometry of the samples. The ICP-OES samples were prepared by dissolving ~ 10 mg of the sample with adequate amounts of aqua regia and diluting the resulting solution with 250 mL of water The Varaian 715-ES instrument was calibrated with standards made from 10,000 ppm standard solutions (Ricca Chemical). Four standard solutions were used for calibration which encompassed the expected concentration range of the samples being measured. All values reported have an error of <2%.

2.1.5. Thermogravimetric Analysis

Thermogravimetric analysis (TGA) and differential scanning calorimetry (DSC) was used to determine the temperature at which materials underwent phase transformations as well as determining if weight was gained or lost during heating. TGA and DSC data were collected simultaneously on a Netzsch Jupiter STA 449 F3 in various inert and oxidizing atmospheres. Depending on the specific requirements of an experiment heating rates ranging from 3 ^{o}C/min to 10 ^{o}C/min were used.

2.1.6. Surface Area Analysis

The surface area of the samples was determined with a Quantachrome autosorb iQ2 Brunauer, Emmett, and Teller (BET) analyzer. Approximately 100 mg of each of the samples was placed in a 10 mL sample holder, outgassed at 100 ^{o}C overnight, and subjected to a multi-point BET adsorption/desorption test. The surface areas were then calculated with the multi-point BET method. The correlation coefficients for all of the BET surface area fits were greater than 0.999.

2.1.7. Spectroscopy

2.1.7.1. Fourier Transform Infrared Spectroscopy

Fourier transform infrared (FTIR) spectroscopic data were collected with a Thermo Scientific Nicolet iS5 operating in transmission mode. Potassium bromide

windows were made by pressing (1.5 Mpa) dry KBr which had been mixed with each sample (~ 0.5 mg) by grinding in an agate mortar.

2.1.7.2. Raman Spectroscopy

Raman spectroscopic data were collected with a Witec Alpha 300 micro-Raman confocal microscope with a 488 nm laser. The scans were collected at a 100x magnification with a 25 second integration time. The Raman slides were prepared by drop casting dilute suspensions of the materials in isopropyl alcohol onto a polished stainless steel slide.

2.1.7.3. X-Ray Photoelectron Spectroscopy

X-ray photoelectron spectroscopy was performed with Al Kα radiation (υ = 1486.5eV) with a power of 150 W at a current of 10 mA and a potential of 15 kV. The electron energies were measured with a concentric hemispherical analyzer. A charge neutralizer was used to prevent charge buildup on the insulating powder samples. The spectra were subsequently corrected such that the adventitious carbon 1s peak was set at an energy of 284.6 eV, corresponding to a correction of 1.9 eV. Individual region spectra were collected with 20 eV pass energy and 0.1 eV step sizes with a 1500 ms dwell-time. CasaXPS software was used to analyze the collected XPS spectra. The spectra were fit with a 70% Gaussian 30% Lorentzian character after the background had been compensated with a Shirley-type fit.

2.2. Electrochemical Testing

2.2.1. Cell Construction

Stainless steel CR 2032 coin cells were constructed to carry out the electrochemical characterization of the materials. The cells were assembled in a glove box having a dry and inert (H_2O < 2 ppm and O_2 < 10 ppm) argon atmosphere. The dry inert atmosphere prevented contamination and oxidation of the highly reactive lithium metal used as the counter electrode. Metallic lithium discs were used as the anodes and glass fiber pre-filters (Millipore APFA04700) were used as separators. An electrolyte comprising a mixture of linear or cyclic carbonates containing a lithium salt, such as

Lithium hexafluorophosphate ($LiPF_6$) or bis(trifluoromethane)sulfonimide lithium (LiTSFI), was used. Additionally, depending on the experiment, a number of electrolyte additives were used to either create passivation layers or to remove water from the cell. The cells were kept for at least 24 h prior to testing. The constructed cells were then tested using an Arbin BT-2000 battery test system.

2.2.2. Electrode Preparation

The positive electrodes contained 70 wt.% active material, 20 wt.% carbon, and 10 wt.% polytetrafluoroethylene (PTFE) binder. The electrodes were made by mixing the PTFE, active material, and carbon with ethanol in an agate mortar. The resulting electrode gum was rolled to a desired thickness, cut to ~ 1 cm^2 discs, and pressed at 1500 psi on a stainless steel mesh. All of the electrodes contained 5 to 7 mg of active material. The electrodes were dried in a vacuum oven at 150 ^oC for > 24 h prior to making cells.

2.2.3. Galvanostatic Cycling

Galvanostatic cycling of the CR2032 coin cells was conducted on an Arbin instruments BT-2000 battery test system. In a typical test, the cells were charged and discharge at a constant current until they reached an upper or lower cutoff voltage. The rate used for cycling was cited as a C-rate which was relative to the nominal theoretical capacity determined by the active material weight. Typical C-rates for testing ranged from C/5 to C/20.

2.2.4. Cyclic Voltammetry

Cyclic voltammetry was performed on the Arbin instruments BT-2000 battery tests system. The CR2032 cells were charged and discharged using a voltage ramp at a constant rate, typically 0.00005 V/s. The ramp was terminated once the potential reached an upper or lower cutoff voltage specific to the given experiment.

2.2.5. Electrochemical Impedance Spectroscopy

Electrochemical impedance spectroscopy (EIS) was performed on the cells with a Solartron 1260A impedance analyzer. The cells were held in a Cr2032 30mm coin cell holder from Arbin instruments and 4-point Kelvin clips were used to interface with the

impedance analyzer. The impedance was measured over a frequency sweep range of 1 MHz to 100 mHz with 6 steps per decade.

Chapter 3: Three Polymorphs of $LiCoPO_4$[1]

3.1. Abstract

Many investigations have been conducted on polyanion cathodes for lithium-ion batteries, specifically $LiMPO_4$ (M = Fe, Mn, Co, Ni), but a majority of which were restricted to the olivine polymorph with the *Pnma* space group. This study presents the synthesis and characterization of three orthorhombic polymorphs of $LiCoPO_4$ belonging to the space groups *Pnma*, $Pn2_1a$, and *Cmcm*. The three polymorphs were synthesized with a microwave-assisted solvothermal (MW-ST) synthesis method at a relatively low temperature of 260℃. The properties and morphology of the materials were characterized with x-ray diffraction, inductively coupled plasma - optical omissions spectroscopy, Raman and infrared spectroscopy, scanning electron microscopy, thermogravometric analysis, galvanostatic charge/discharge, and cyclic voltammetry. The electrochemical properties of the *Cmcm* polymorph and nano-sized $Pn2_1a$ polymorph are reported for the first time.

3.2. Introduction

Lithium-ion batteries are a key enabling technology in both portable electronics as well as next-generation electric vehicles. Following the investigations of first $Fe_2(SO_4)_3$ and $Fe_2(MO_4)_3$ (M = Mo and W) in the 1980s's[49,50] and then $LiFePO_4$ in the 1990's, much effort has been focused on polyanion cathodes, specifically $LiMPO_4$ where M = Fe, Mn, Co, and Ni.[51,23,52,53] Cathodes with M = Mn, Co, and Ni are promising materials due to the higher operating voltage of the $M^{2+/3+}$ redox couples, 4.1, 4.8, and 5.2 V versus lithium, respectively, compared to 3.6 V for M = Fe. The currently available organic

[1] The majority of the work discussed in this chapter was carried out by Karl Kreder. Gaurav Assat provided assistance in conducting experiments. This chapter is based on previously published work: K. Kreder, G. Assat, A. Manthiram, "Microwave-Assisted Solvothermal Synthesis of Three Polymorphs of $LiCoPO_4$ and Their Electrochemical Properties," *Chemistry of Materials*, 17, 5543-5549 (2015).

liquid electrolytes are not stable above 5 V, which prevents the electrochemical characterization and use of $LiNiPO_4$.[54] Moreover, it has been shown that a small hole polaron may not form in $LiNiPO_4$ preventing lithium migration.[55] Therefore, both $LiMnPO_4$ and $LiCoPO_4$ are potential candidates for higher voltage, higher energy density insertion cathodes.

Low-temperature synthesis techniques such as microwave-assisted solvothermal (MW-ST), microwave-assisted hydro-thermal (MW-HT), sol-gel, and iono-thermal methods may produce metastable phases which are not otherwise accessible by high-temperature solid-state methods. Previously, Klingeler et al[56], reported hydrothermal synthesis of $LiCoPO_4$ ($Pn2_1a$) and the electrochemical activity of micrometer-sized particles. Small particle size (nanoscale) is preferred with polyanion cathodes due to their low electronic ($<10^{-9}$ S-cm^{-1}) and ionic (< 10-12 cm^2-s^{-1}) conductivity[51,16]. Additionally, $LiCoPO_4$ (*Cmcm*) has been reported via the conversion of $LiCoPO_4$ (*Pnma*) at high pressure (15 GPa) but with no electrochemical data is available.[57] Furthermore, there have been a number of reports of low-temperature solvothermal synthesis of $LiMPO_4$ employing poly-glycols, including tetraethylene glycol, which have not yet reported or characterized the dependence of the produced polymorphs on the presence of water.[58–61] Here, we report the low-temperature, MW-ST synthesis of $LiCoPO_4$ (*Cmcm*) and LiCoPO4 ($Pn2_1a$) nano-particles and their electrochemical activity, for the first time. The already-known *Pnma* phase (olivine) of LiCoPO4 is also prepared by the MW-ST process at the same temperature of 260℃, and the three crystalline forms are compared. During synthesis, the amount of water as well as ammonium hydroxide plays a critical role in determining which polymorph is formed.

3.3. Experimental

All three polymorphs of $LiCoPO_4$ were formed by the MW-ST synthesis with tetra-ethylene glycol (TEG) (Sigma-Aldrich 99%) as the solvent. For both *Pnma* and $Pn2_1a$ polymorphs, stoichiometric ratios (1 : 1 : 1) of lithium hydroxide monohydrate (Alfa Aesar, 98%), cobalt acetate tetrahydrate (Acros Organics 98+%), and phosphoric

acid (Fisher Scientific, 85%) precursors were measured and dissolved in 12 mL of TEG. For the *Cmcm* polymorph, anhydrous phosphoric acid (Aldrich 99.999%) was used instead of the liquid 85% phosphoric acid. Approximately, 100 mg (2.38 mmol) of lithium hydroxide monohydrate was used in all reactions. Fresh, clear TEG was dried with anhydrous magnesium sulfate (~ 1 : 3 volume ratio) immediately prior to starting all reactions. The solution was stirred for 1 hour, allowed to settle for 3 hours, then decanted and centrifuged to separate out the remaining magnesium sulfate. In addition to the precursors, one-half of an equivalent of ammonium hydroxide was added to produce the $Pn2_1a$ polymorph. One-half of an equivalent of ammonium hydroxide and six equivalents of water were added to form the *Pnma* polymorph. The precursors were placed in a 30 mL borosilicate microwave vessel and stirred, for approximately 2 hours, until the precursors dissolved. The solutions were then heated in an Anton Paar Monowave 300 as quickly as possible to 260℃, as measured by the infrared temperature sensor. The solution was heated with up to 800 W of power corresponding to a heating rate of ~100 ^{o}C-min^{-1}. The reaction mixture was held at 260 ^{o}C for 30 minutes while being stirred at 600 RPM. The synthesized samples were washed 3 times with acetone and subjected to 5 minutes of ultra-sonication to break up agglomerations prior to centrifugation. The samples were then dried in an air oven at 100℃.

Powder X-ray diffraction (XRD) patterns were collected from 10 - 120° 2θ at 1.2 degrees per second. Thermogravimetric analysis (TGA) was performed in an inert argon atmosphere at a heating rate of 10℃/min. The ICP-OES was calibrated with standard solutions (Ricca Chemical Company) of lithium, cobalt, and phosphorous. Coin cells were made with commercial Purolyte A6 series (Novolyte Technologies) electrolyte comprised of a 1 : 1 mixture of ethylene carbonate (EC) and dimethyl carbonate (DMC) and 1 M lithium-tetrafluorophosphate ($LiPF_6$). The cells were rested for 24 h before testing. Electrochemical tests, cyclic voltammetry (CV), and galvanostatic charge/discharge were performed with an Arbin Instruments battery test system.

3.4. Results and Discussion

3.4.1. Structure and Morphology

The as-synthesized materials formed in three distinct colors, dark pink, dark blue, and light pink, as shown in Figure 3.1, corresponding, respectively, to *Pnma*, *Pn*2_1*a*, and *Cmcm* polymorphs. The SEM micrographs showed that the *Pnma* and *Pn*2_1*a* polymorphs have a similar nano-rod morphology with ~ 200 nm width and up to 1 μm length. The *Cmcm* polymorph formed with a nano-sheet morphology with ~ 50 nm thick, 200 nm wide, and 1 to 3 μm length. This morphology is favorable to perform electrochemical measurments on $LiMPO_4$ materials.[62] The three $LiCoPO_4$ polymorphs all belong to the orthorhombic crystal system. The powder XRD patterns of the three polymorphs are shown in Figure 3.2.

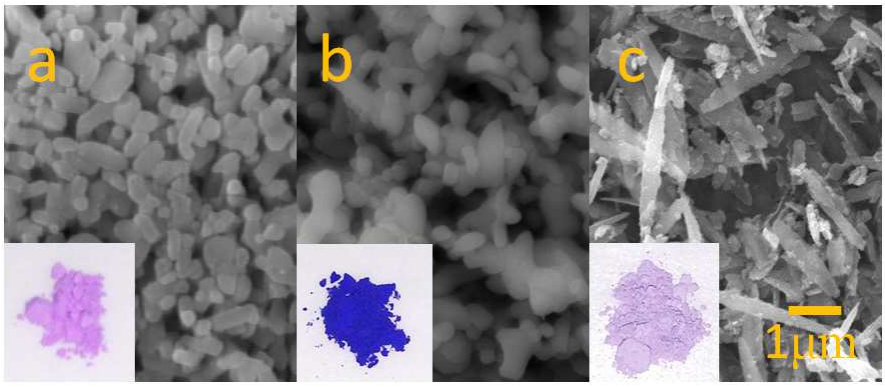

Figure 3.1. SEM micrographs and color photos of the three polymorphs of $LiCoPO_4$: (a) *Pnma*, (b) *Pn*2_1*a*, (c) *Cmcm.*

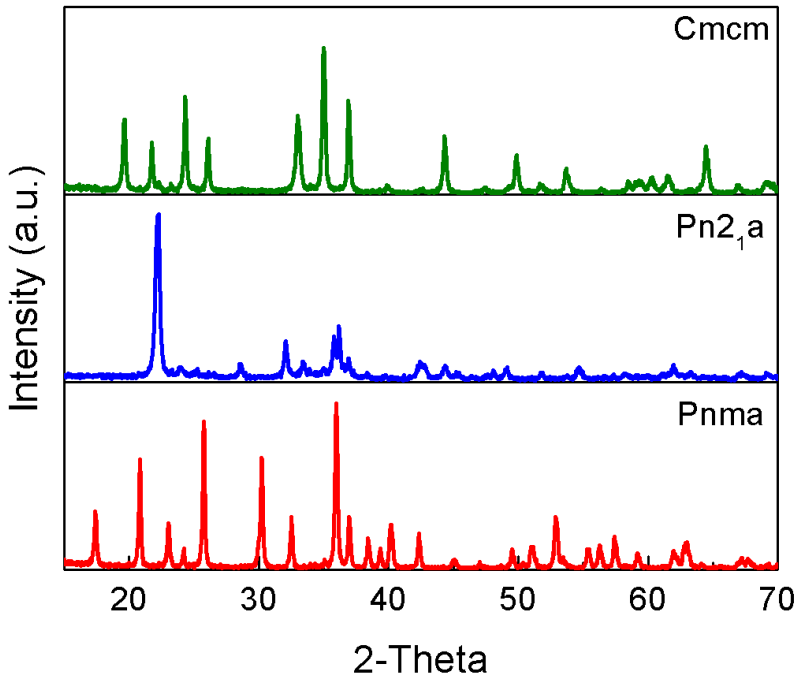

Figure 3.2. Powder XRD patterns of the three polymorphs of $LiCoPO_4$.

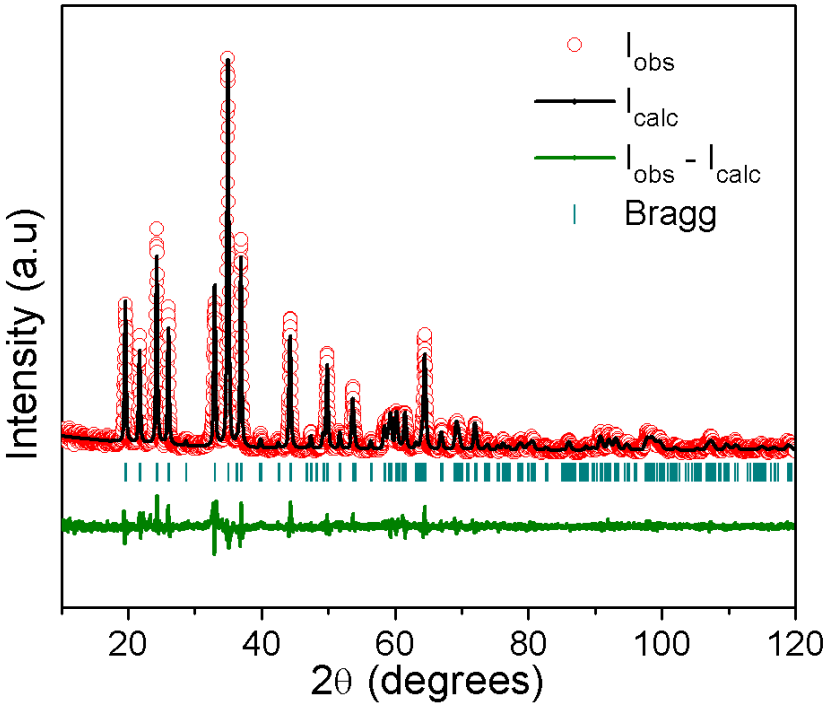

Figure 3.3. Rietveld refinement results of $LiCoPO_4$ (*Cmcm*). Green line shows the difference between observed and calculated intensities.

The $LiCoPO_4$ (*Pnma*) and (*Cmcm*) polymorphs were synthesized in pure forms with little or no mixing between them, as indicated by the absence of alternate phase peaks. The $LiCoPO_4$ ($Pn2_1a$) polymorph formed with a slight $LiCoPO_4$ (*Cmcm*) impurity which was determined to be approximately 2.5 wieght % of the sample via multiphase Rietveld refinement. The *Pnma* space group was identified using the ICSD database. The $Pn2_1a$ and the *Cmcm* space groups were identified via the Rietveld method using $LiZnPO_4$ (ICSD No. 01-083-0264) and β-$LiFePO_4$ (ICSD No. 01-072-7847) as prototypes, resepectively. Rietveld refinement was performed over a range of 10 - 120 degrees 2θ for all three $LiCoPO_4$ polymorphs. $LiCoPO_4$ (*Cmcm*) polymorph structure has been reported once previously[57] via a high pressure (15 MPa) synthesis, although it was referred to as a 'Na_2CrO_4-like' structure which belongs to the *Cmcm* space group. The Rietveld refinement results of the low-temperature MW-ST $LiCoPO_4$ (*Cmcm*) polymorph are shown in Figure 3.3. The observed pattern is shown as red circles, the calculated pattern is shown as a black line, and the difference between these two is indicated in green. The absence of non-indexed Bragg peaks suggests there are no impurity phases present in the sample. Furthermore, the low value of 1.06 for χ^2 indicates that the refined structure is in good agreement with the experimentally measured data. The crystallographic parameters of the refined $LiCoPO_4$ (*Cmcm*) phase are shown in Table 3.1 and the atomic positions are presented in Table 3.2. The empirical results of the Rietveld refinement were used to generate images of the crystallographic structure of $LiCoPO_4$ (*Cmcm*), shown in Figure 3.4, using the VESTA software. Rietveld refinement was also carried out on the *Pnma* and $Pn2_1a$ $LiCoPO_4$ polymorphs and is shown in Figure 3.5 and Figure 3.7, respectively. Moreover, images of the crystallographic of the *Pnma* and $Pn2_1a$ $LiCoPO_4$ polymorphs were also generated and are shown in Figure 3.6 and Figure 3.8, respectively.

Table 3.1. Crystallographic parameters of $LiCoPO_4$ (Cmcm) as determined by the Rietveld refinement

Crystallographic parameters of $LiCoPO_4$ (Cmcm)	
Empirical Formula	$LiCoPO_4$
Crystal System	Orthorhombic
Space group (No.)	Cmcm (63)
a (Å)	5.423(1)
b (Å)	8.161(1)
c (Å)	6.222(0)
V (Å)	275.40
2θ range (degrees)	10-120
2θ step increment (degrees)	continuous
Number of reflections	127
χ^2	1.71
R_{wp}	21.9

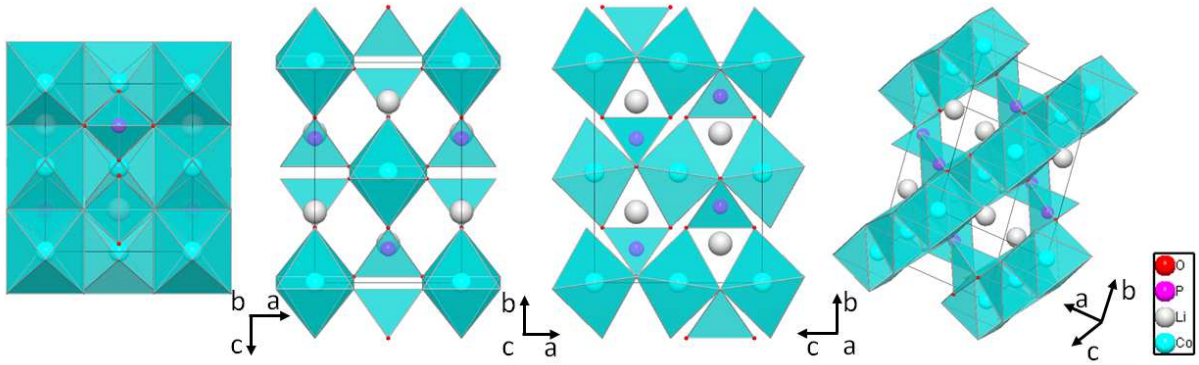

Figure 3.4. Illustration of the $LiCoPO_4$ (*Cmcm*) structure along *a*, *b*, and *c* crystallographic axes. Also, the projection illustrating the possible channels for lithium mobility is shown.

Table 3.2. Atomic positions of $LiCoPO_4$ (Cmcm)

	Wyck.	x/a	y/b	z/c	Occ.
Li	4*c*	0.0000	0.6766	0.2500	1.000
Co	4*a*	0.0000	0.0000	0.0000	1.000
P	4*c*	0.0000	0.3496	0.2500	1.000
O1	8*f*	0.2295	0.4657	0.2500	1.000
O2	8*g*	0.0000	0.2483	0.0478	1.000

Table 3.3. Atomic positions of $LiCoPO_4$ (*Pnma*)

Atom	Wyck.	x/a	y/b	z/c	Occ.
Li	4*a*	0.0000	0.0000	0.0000	1.000
Co	4*c*	0.2216	0.2500	0.5204	0.999
P	4*c*	0.4044	0.2500	0.0801	0.994
O1	4*c*	0.4048	0.2500	0.7587	1.000
O2	4*c*	0.0442	0.2500	0.2863	1.000
O3	8*d*	0.3325	0.0448	0.2178	1.000

Table 3.4. Crystallographic parameters of $LiCoPO_4$ (*Pnma*)

Crystallographic parameters of $LiCoPO_4$ - Pnma	
Empirical formula	$LiCoPO_4$
Crystal system	Orthorhombic
Space group	Pnma
Space group No.	62
a (Å)	10.199(4)
b (Å)	5.918(7)
c (Å)	4.699(6)
V ($Å^3$)	283.71
2θ range (^{o})	10-120
2θ step increment (^{o})	0.02
No. of reflections	238
R_{wp}	19.1
$\chi 2$	1.53

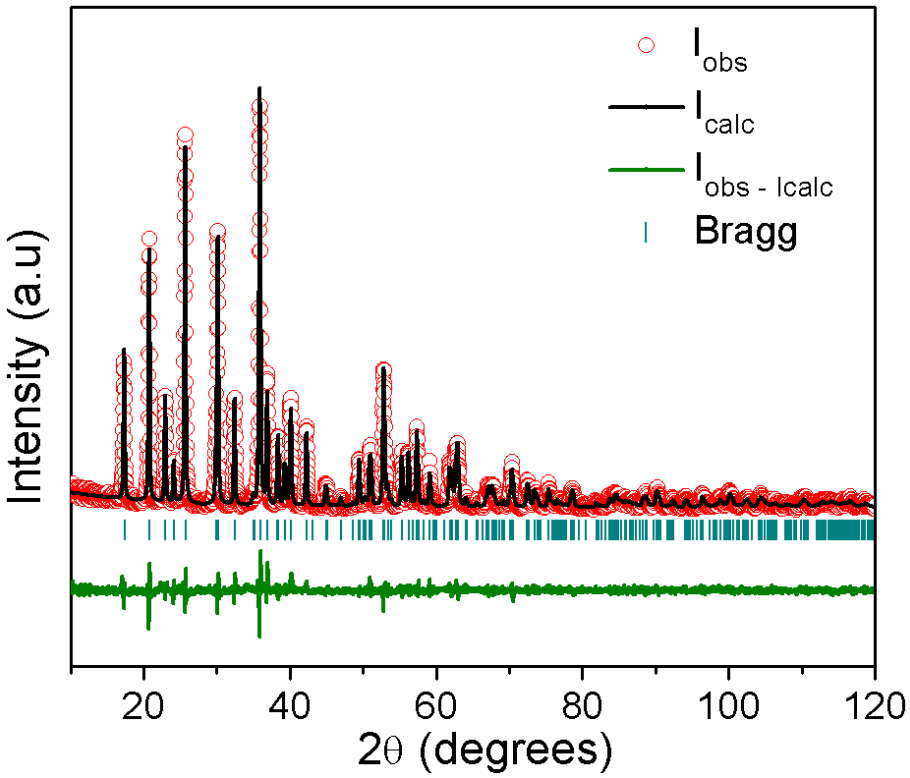

Figure 3.5. Rietveld refinement results of $LiCoPO_4$ (*Pnma*).

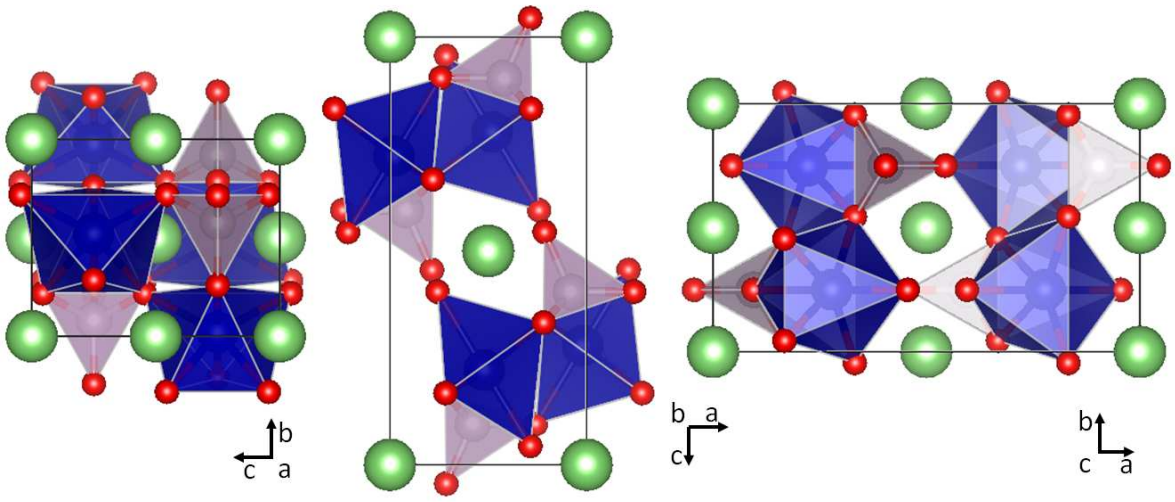

Figure 3.6. Crystal structure of $LiCoPO_4$ (*Pnma*).

Table 3.5. Atomic positions of $LiCoPO_4$ ($Pn2_1a$)

Atom	Wyck.	x/a	y/b	z/c	Occ.
Li	4*a*	0.8926	0.7453	0.3405	1.000
Co	4*a*	0.3456	0.2142	0.1978	1.000
P	4*a*	0.4120	0.4634	0.6705	1.000
O1	4*a*	0.3461	0.2949	0.8236	1.000
O2	4*a*	0.1645	0.2345	0.2923	1.000
O3	4*a*	0.3979	0.4578	0.3495	1.000
O4	4*a*	0.4308	0.0000	0.2396	1.000

Table 3.6. Crystallographic parameters of $LiCoPO_4$ ($Pn2_1a$)

Crystallographic parameters of $LiCoPO_4$ – $Pn2_1a$	
Empirical formula	$LiCoPO_4$
Crystal system	Orthorhombic
Space group	$Pn2_1a$
Space group No.	33
a (Å)	10.039(7)
b (Å)	6.712(3)
c (Å)	4.963(7)
V ($Å^3$)	334.50
2θ range (^{o})	10-120
2θ step increment (^{o})	0.02
No. of reflections	279
R_{wp}	31.4
$\chi 2$	1.78

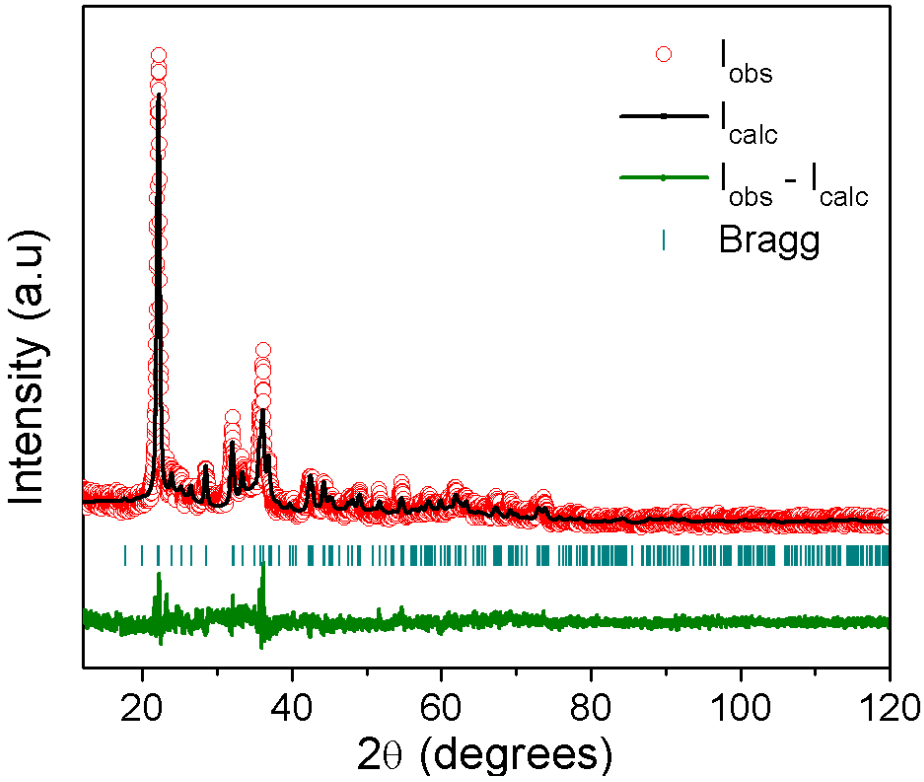

Figure 3.7. Rietveld refinement results of $LiCoPO_4$ ($Pn2_1a$).

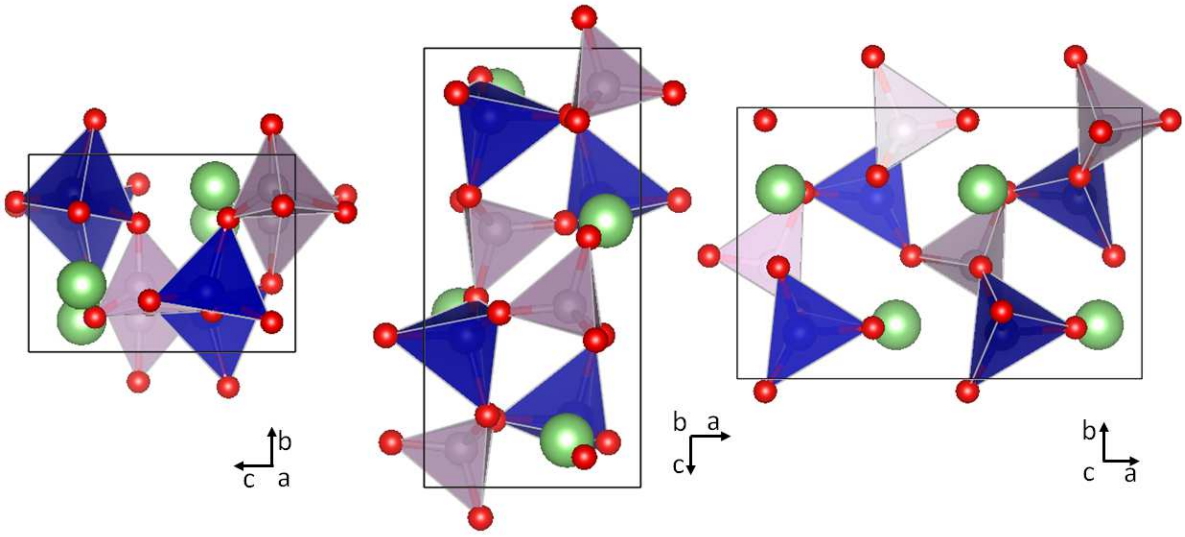

Figure 3.8. Crystal structure of $LiCoPO_4$ ($Pn2_1a$).

A comparison between the lattice parameters and unit cell volume of the three $LiCoPO_4$ polymorphs is presented in Table 3. The $Pn2_1a$ polymorph is the least dense, with the *Pnma* and *Cmcm* polymorphs having 15% and 17% higher densities, respectively.

Table 3.7. Comparison of the crystallographic parameters of the three polymorphs

Phase (No.)	a (Å)	b (Å)	c (Å)	V (Å^3)
Pnma (62)	10.199(4)	5.918(7)	4.699(6)	283.71
$Pn2_1a$ (33)	10.039(7)	6.712(3)	4.963(7)	334.50
Cmcm (63)	5.423(1)	8.161(1)	6.222(0)	275.40

The low density of the *Pn*2_1*a* polymorph is due to the corner-shared tetrahedral coordinated cobalt ions, which leads to a less dense packing compared to the edge-shared octahedral coordinated cobalt ions in the *Pnma* and *Cmcm* polymorphs. The *Cmcm* polymorph has the highest density among the three polymorphs and has smaller pathways for lithium ion migration, which may contribute to the lower observed electrochemical activity.

3.4.2. MW-ST Synthesis Parameters

The presence of water and ammonium hydroxide critically impacted which polymorph of $LiCoPO_4$ would form. TEG is hygroscopic and absorbs water from the ambient environment.[63] Therefore, it was critical to control the water content of the TEG to get reproducible synthesis conditions. Figure 5 shows the dependence of the wt. % of the phases formed on water content. These experiments were carried out by first drying the TEG with anhydrous $MgSO_4$ and then adding the indicated amount of deionized water. The weight percentages of the *Pnma* and *Cmcm* polymorphs were estimated with multi-phase Rietveld refinement. The use of anhydrous phosphoric acid and dry TEG during synthesis results in the formation of > 99% *Cmcm* polymorph by weight. The introduction of 2% water by volume (200 μL) results in ~ 22% *Pnma* and 78% *Cmcm* phases by weight. The preference of the production of the *Pnma* polymorph continues to increase with increasing water content, but has lower sensitivity, reaching ~ 29% *Pnma* by weight at 6 volume % water. Therefore, the ratio of the *Pnma* and *Cmcm* polymorphs are the most sensitive to water below 2 volume % water

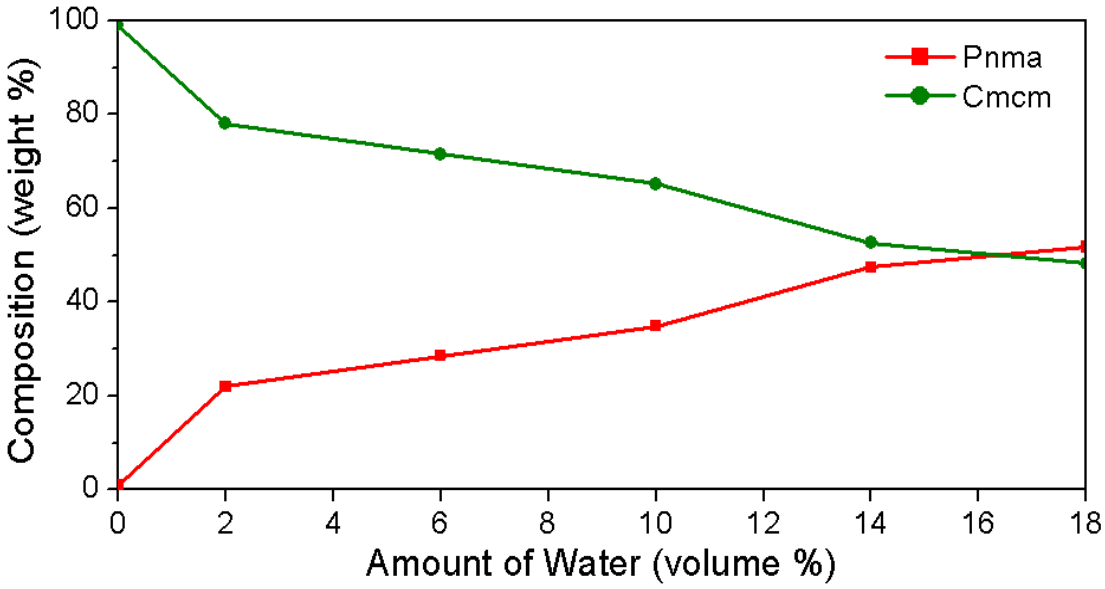

Figure 3.9. Dependence of the percentage of the *Pnma* and *Cmcm* phases on the volume percent water in TEG.

.

3.4.3. Materials Characterization

The stoichiometries of the three $LiCoPO_4$ polymorphs were measured with ICP-OES and the results are presented in Table 3.8. The stoichiometry of each of the polymorphs is close to the nominal stoichiometry of $LiCoPO_4$, with any variances within the range of experimental error.

Table 3.8. Verification of the chemical compositions of the three polymorph of $LiCoPO_4$

Phase	ICP stoichiometry		
	Li/P	Co/P	P
Pnma	1.03	1.03	1.00
$Pn2_1a$	1.04	1.02	1.00
Cmcm	1.04	0.96	1.00

The FTIR spectra of the three LiCoPO4 polymorphs are shown in Figure 3.10. The absorption peaks from 900 to 1200 cm^{-1} correspond to the bond stretching of the PO_4^{-3} anion group while the peaks from 400 to 700 cm^{-1} correspond to the bending

modes.[64] Specifically, for the *Pnma* polymorph, the 938 cm^{-1} band is the symmetric stretching υ_1 mode. The three bands from 1020 to 1170 cm^{-1} belong to the antisymmetric stretching υ_3 mode and are due to the site symmetry of the PO_4^{3-} anion in the *Pnma* structure.[65] The υ_1 mode of the *Pn*2_1*a* polymorph is inactive and the three υ_3 bands are present but shifted to lower wavenumbers. The *Pn*2_1*a* polymorph has a more covalent P-O bond due to the four-coordinated cobalt ions compared to the six-coordinated cobalt ions in the *Pnma* polymorph.[56] Consequently, due to the inductive effect across the P-O-Co bond group, the Co-O bond is likely less covalent in the *Pn*2_1*a* polymorph. The *Cmcm* polymorph has both the υ_1 and υ_3 stretching modes. The splitting of the υ_3 mode is suppressed due to the lower C_2 site symmetry in the *Cmcm* structure.

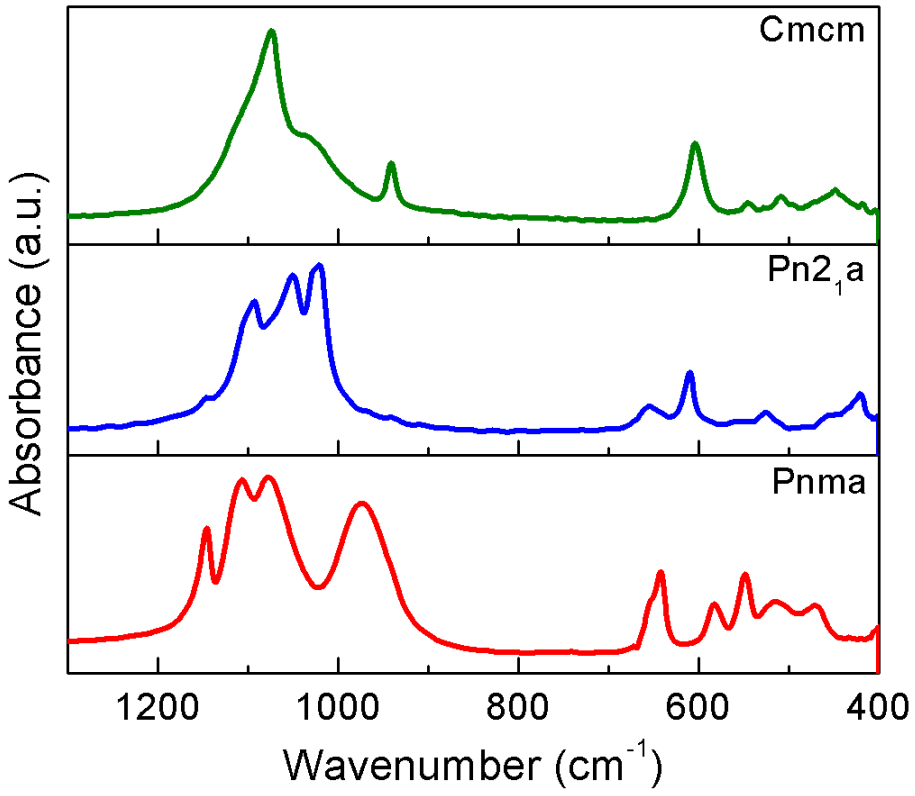

Figure 3.10. FTIR spectra of the three $LiCoPO_4$ polymorphs.

The Raman spectra of the three LiCoPO4 polymorphs are shown in Figure 3.11. Collecting Raman spectra was difficult because the laser had sufficient intensity to cause

both the *Pn*2$_1$*a* and *Cmcm* polymorphs to undergo phase transitions to the *Pnma* polymorphs. Scans were collected at the highest laser power at which the spectrum appeared to be stable over time. Furthermore, both the *Pn*2$_1$*a* and *Cmcm* polymorphs suffered from florescence, which increased the background noise in the spectra. The peaks in $LiCoPO_4$ (*Pnma*) at ~ 950 and ~ 1050 cm^{-1} are attributed to the antisymmetric stretching of PO_4^{3-} (υ_3) while the peak at 990 cm^{-1} belongs to the symmetric stretching υ_1. The bands at 580 and 625 cm^{-1} in the $LiCoPO_4$ (*Pnma*) correspond to the υ_4 bending modes, while the peak at 440 cm^{-1} corresponds to the υ_2 bending mode.[66] The precise assignment of the Raman peaks below 800 cm^{-1} for the *Cmcm* and *Pn2$_1$a* polymorphs would require the use of density functional theory simulations.[67]

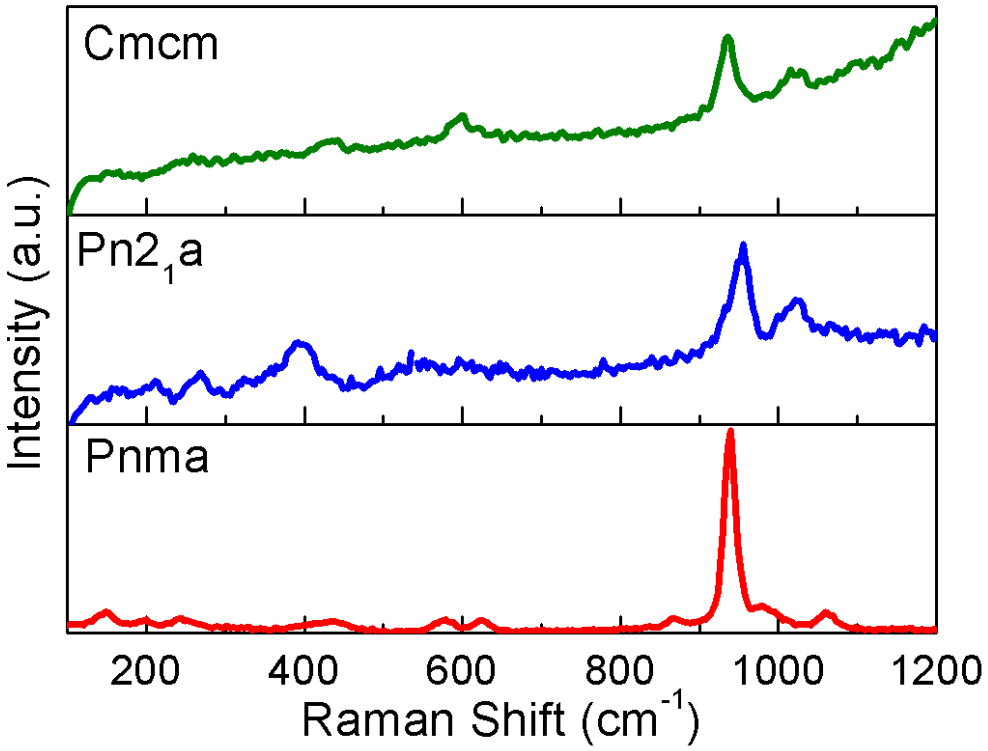

Figure 3.11. Raman spectra of the three $LiCoPO_4$ polymorphs.

The TGA/DSC data are presented in Figure 3.12. The *Pnma* polymorph was found to be stable up to 800℃ and did not experience any mass loss. The *Pn*2$_1$*a* polymorph had an endothermic event starting at 200℃ accompanied by a mass loss. The mass loss is attributed to entrained residual water or ammonia, remaining from synthesis,

coming off the sample. The presence of residual ammonia or water may lead to the formation of HF in the presence of $LiPF_6$, which would be detrimental to electrochemical cycleability. The endothermic event at ~ 340℃ does not have a mass loss and likely corresponds to the phase transformation of $Pn2_1a$ to *Pnma*.

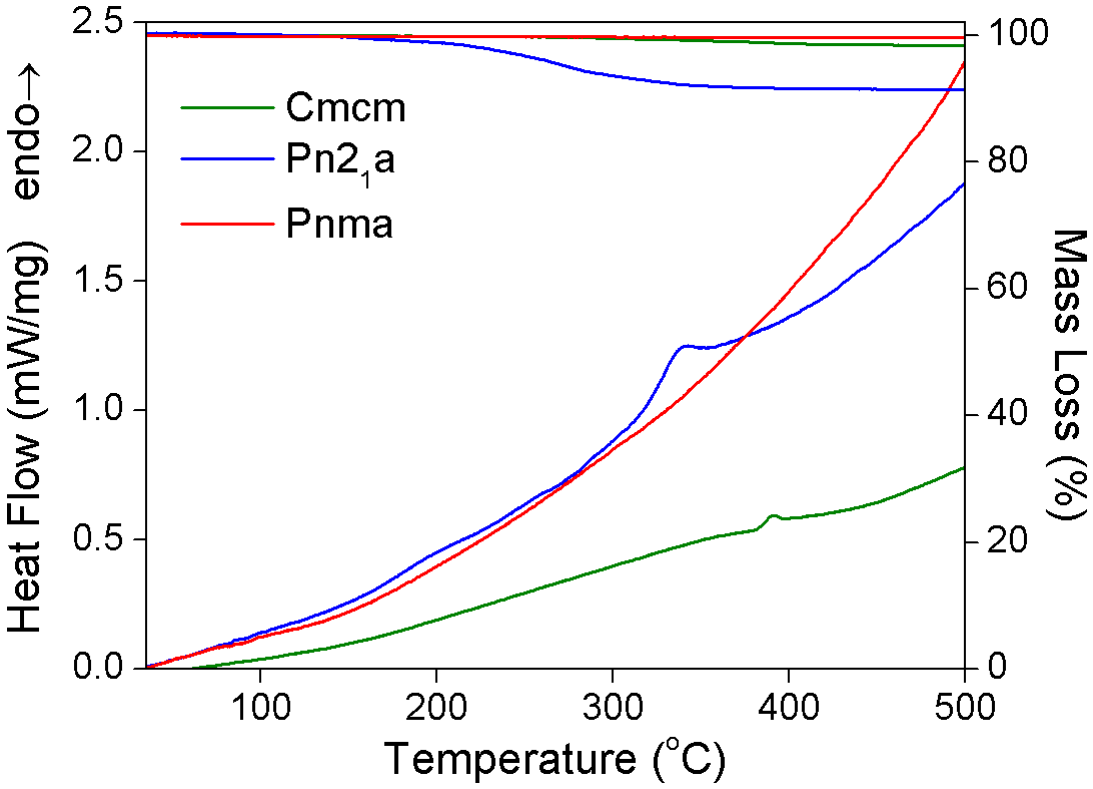

Figure 3.12. TGA plots of the as-synthesized $LiCoPO_4$ polymorphs. Only shown to 500 ^oC for clarity.

The *Cmcm* polymorph has an endothermic event at 400 ^oC with a small (< 0.5%) simultaneous mass loss, the cause of which is un-known. The *Cmcm* polymorph was heated to various temperatures (425℃ to 600℃ in 25℃ increments) for 8 h in an argon atmosphere and was found to transform to the *Pnma* polymorph upon heating. The start of the phase transition occurred ~ 475℃ and did not fully complete until 600℃. The morphology of the particles changed during the phase transition from nano-sheets to nano-rods.

3.4.4. Electrochemical Characterization

The three polymorphs were characterized by both galvanostatic charge/discharge as well as cyclic voltammetry. The results of the CV testing are shown in Figure 3.13. All of the tests were run at a rate of 0.05 mV-s^{-1}. The LiCoPO4 (*Pnma*) has the expected redox peaks at 4.8 and 4.9 V.[22] The $LiCoPO_4$ ($Pn2_1a$) polymorph nano-particles have one redox peak at 4.95 V. The $LiCoPO_4$ *(Cmcm*) polymorph has an irreversible redox peak at ~ 4.3 V, which agrees with the computationally predicted redox peak[68]. Although lithium was de-intercalated from $LiCoPO_4$ (*Cmcm*) at 4.3 V, this was not reversible as indicated by the absence of the corresponding redox peak on discharge. The peak at 4.3 V is not attributed to decomposition of the electrolyte because this is well below the upper potential of the electrolyte stability window,[69] as well as agreeing with computationally predicted potential. The $LiCoPO_4$ (*Pnma*) redox couples agree with previously published results and corresponds to the redox of two two-phase regions,[22] specifically $LiCoPO_4/Li_{0.66}CoPO_4$ and $Li_{0.66}CoPO_4/CoPO_4$. Both the $Pn2_1a$ and the *Cmcm* polymorphs have a single redox peak which indicates they do not have the $Li_{0.66}CoPO_4$ or any other line phase. The CV tests show that the three different phases of $LiCoPO_4$ have distinctly different electrochemical properties and redox potentials. The variation in the redox potentials is most likely due to the different bonding environment of the cobalt in the three different polymorphs. Furthermore, the higher potential of $Pn2_1a$ compared to *Pnma* polymorph observed via electrochemistry correlates with the $Pn2_1a$ Co-O bond being less covalent than the *Pnma* Co-O bond observed via Raman spectroscopy.

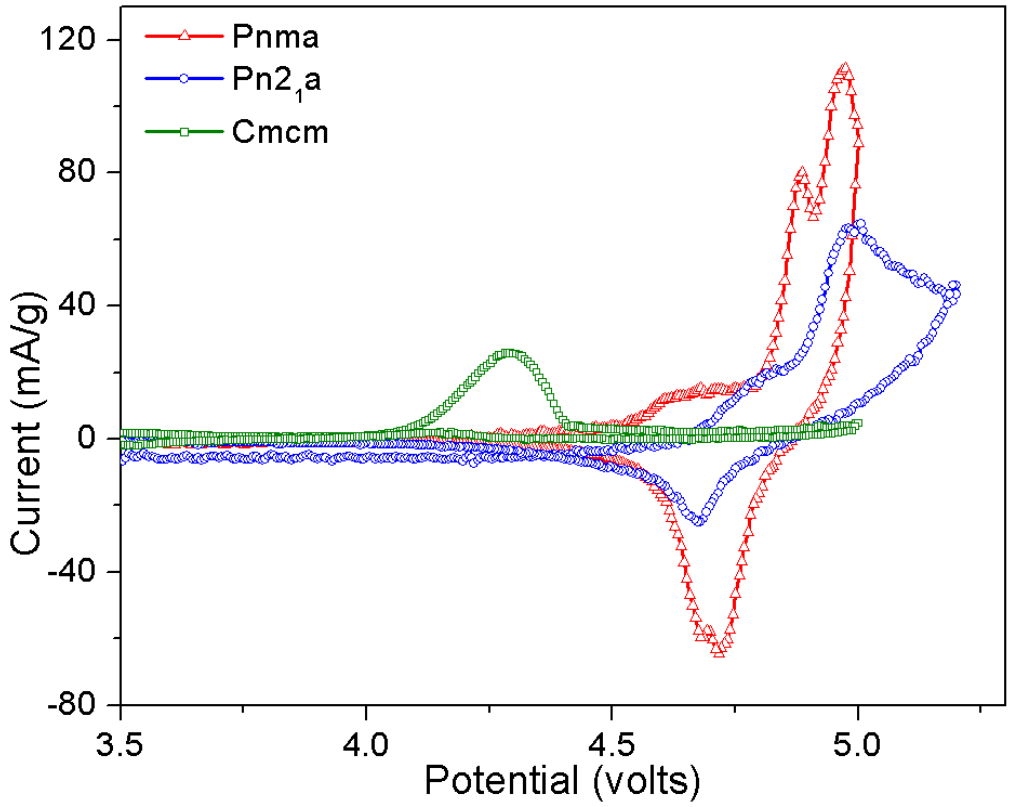

Figure 3.13. Cyclic Voltammagram of the three $LiCoPO_4$ phases. Cmcm and Pnma phases were run from 2.5 to 5 V and the $Pn2_1a$ phase was run from 2.5 to 5.3 V. All CVs were run at a rate of 0.05 mV-s^{-1}.

In addition to CV testing, galvanostatic charge discharge testing was also performed. No attempt was made to optimize the electrode performance. A number of methods have been demonstrated previously to increase the capacity of $LiCoPO_4$ (*Pnma*), including carbon coating, ball milling, or coating with a conductive polymer such as PDOT.[70–72]. Many of the optimization methods may not be compatible with the low-temperature $LiCoPO_4$ (*Cmcm)* and $LiCoPO_4$ (*Pn*2_1*a*) polymorphs. Therefore, the materials were tested by simply mixing with 20 wt.% carbon to avoid complications of the comparisons of the three phases. The three polymorphs of $LiCoPO_4$ showed first-cycle discharge capacities of 67, 33 and 6 mAh-g^{-1}, respectively, for the *Pnma*, *Pn*2_1*a*, and *Cmcm* polymorphs. The specific capacities are reported based on active material weight excluding the carbon and the binder. The $LiCoPO_4$ (*Pnma*) first cycle discharge capacity of 67 $mAhg^{-1}$ is significantly less than previously reported first discharge capacities in more optimized electrode/electrolyte systems of 120 - 130 $mAhg^{-1}$.[55,73] All

of the $LiCoPO_4$ polymorphs experienced relatively rapid capacity fade, which is largely attributed to the high operating voltage and the use of a sub-optimal EC:DMC electrolyte, but it could also be due to poor conductivity.

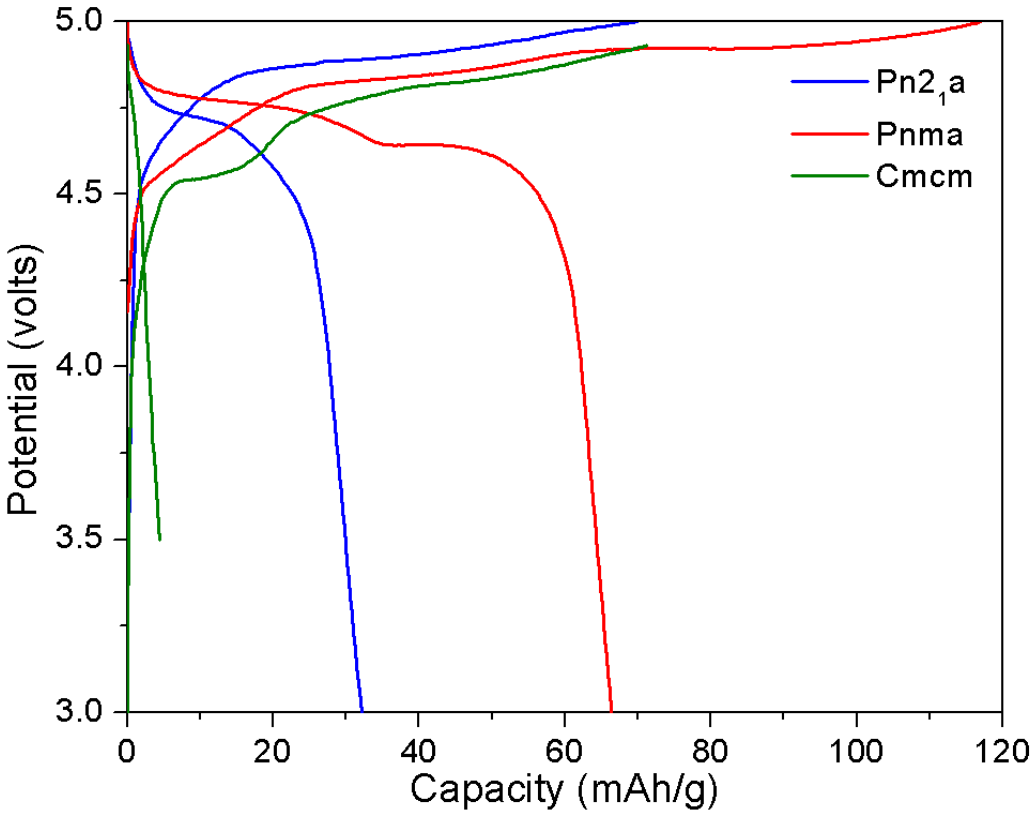

Figure 3.14. Galvanostatic first charge/discharge profiles of LiCoPO4 phases at C/10 rate. The *Pnma* and *Cmcm* phases were tested at 3.0-5.0 V and the *Cmcm* phase at 3.5-4.7 V.

3.5. Conclusion

Three different polymorphs of $LiCoPO_4$ were successfully synthesized via a facile microwave-assisted solvothermal method. The production of each of the polymorph was highly sensitive to the presence of small amounts of water in the solvent, TEG. The sensitivity of the phases generated may translate to the MW-ST synthesis of other $LiMPO_4$ materials. The synthesis of $LiCoPO_4$ *Cmcm* was demonstrated at low temperature. The lithium extraction/insertion reaction with the $LiCoPO_4$ (*Cmcm*)

polymorph was presented for the first time, but it was not reversible. FTIR spectroscopy gave empirical evidence to the change in the covalence of the P-O bond in the different polymorphs of $LiCoPO_4$. The $LiCoPO_4$ ($Pn2_1a$) polymorphs could be a promising candidate for future research due to the high theoretical specific energy capacity and demonstrated electrochemical activity. The problem of the residual ammonia needs to be addressed, and the cycleability improved for the $Pn2_1a$ polymorph to be used as a practical cathode material.

Chapter 4: Aliovalent Substitution of V^{3+} for Co^{2+} in $LiCoPO_4$ by a Low-temperature Microwave-assisted Solvothermal Process[2]

4.1. Abstract

Electrical and ionic conductivity has proven to be a major limiting factor in the adoption of high-voltage polyanion cathode materials, specifically $LiMPO_4$ (M = Mn, Co, Ni). While the aliovalent substitution of V^{3+} for Fe^{2+} in $LiFePO_4$ has been shown recently, no conclusive evidence is available for aliovalent substitutions in the analogous $LiCoPO_4$. This study presents a low-temperature microwave-assisted solvothermal synthesis and characterization of aliovalently substituted $LiCo_{1-3x/2}V_x\square_{x/2}PO_4$ for $x \leq 0.07$. The as synthesized $LiCo_{1-3x/2}V_x\square_{x/2}PO_4$ samples belonging to the $Pn2_1a$ space group are transformed to the *Pnma* polymorph via calcination in an inert atmosphere at 525℃. The $LiCo_{1-3x/2}V_x\square_{x/2}PO_4$ samples are characterized with scanning electron microscopy, X-ray diffraction, Rietveld refinement, inductively coupled plasma optical emissions spectroscopy, Raman & infrared spectroscopy, galvanostatic charge/discharge, electrochemical impedance spectroscopy, and cyclic voltammetry. Unlike the prior reports of aliovalent substitution via high-temperature methods, the $LiCo_{1-3x/2}V_x\square_{x/2}PO_4$ samples presented here experienced a systematic decrease in the unit cell volume with increasing vanadium substitution. The electrochemical performance and cyclability of $LiCo_{1-3x/2}V_x\square_{x/2}PO_4$ is greatly improved compared to the unsubstituted $LiCoPO_4$.

4.2. Introduction

Lithium-ion batteries have assisted the proliferation of mobile electronics and enabled the nascent adoption of electric and hybrid electric vehicles. Wide spread adoption of electric transportation requires the advent of cost-effective, higher energy density batteries. Polyanion cathodes are promising candidates as next-generation

[2] The majority of the work discussed in this chapter was carried out by Karl Kreder. Gaurav Assat provided assistance in conducting experiments. This chapter is based on previously published work: K. Kreder, G. Assat, A. Manthiram, "Aliovalent Substitution of V^{3+} for Co^{2+} in $LiCoPO_4$ by a Low-Temperature Microwave-Assisted Solvothermal Process," *Chemistry of Materials*, 28, 1847-1853 (2016).

intercalation compounds because they offer higher voltages and multi-ion reactions which have higher theoretical energy density compared to incumbent technologies.

Manthiram and Goodenough initially investigated the polyanion compounds $Fe_2(XO_4)_3$ (X = Mo, W, S) in the late 1980's.[49,50] Subsequently, Goodenough's group developed $LiFePO_4$, which initially suffered from low power density due to poor electrical conductivity.[13] Over the next several years it was demonstrated that nanosizing $LiFePO_4$ led to improved rate capability and exceptional cyclability.[16,74] In 2004, Nazar et al, demonstrated that early reports of increase in electronic conductivity due to low percentage doping of olivine phosphates was likely due to interspersed conductive metal phosphide phases at particle boundaries.[75] Subsequently, both our group and Whittingham's group have demonstrated the substitution of 10 to 20 % V^{3+} in $LiFePO_4$.[76,77,26,78] Following the demonstration of the aliovalent substitution of V^{3+} in $LiFePO_4$, our group demonstrated aliovalent substitution of vanadium in LiMnPO4 and the resulting improved conductivity and electrochemistry.[79] Additionally, our group has also demonstrated that the formation of the various polymorphs (*Pnma*, *Pn21a*, and *Cmcm*) of $LiCoPO_4$ are critically dependent on the presence of both water and ammonia during microwave-assisted solvothermal (MW-ST) synthesis.[80]

This investigation reports the low-temperature, low-pressure, MW-ST synthesis of vanadium substituted $LiCo_{1-3x/2}V_x\square_{x/2}PO_4$ at 240℃. $LiCo_{1-3x/2}V_x\square_{x/2}PO_4$ is synthesized for values of $x \leq 0.07$. Furthermore, it is demonstrated that the low-temperature synthesis is critical to achieving higher levels of vanadium substitution. The substituted $LiCo_{1-3x/2}V_x\square_{x/2}PO4$ show improved electrical and ionic conductivity, leading to improved electrochemical properties.

4.3. Experimental

4.3.1. Microwave-assisted Solvothermal Synthesis

All the $LiCo_{1-3x/2}V_x\square_{x/2}PO_4$ were synthesized via MW-ST synthesis with a tetraethylene glycol (TEG) (Sigma-Aldrich 99%) solvent. $LiCoPO_4$ was synthesized with stoichiometric ratios (1 : 1 : 1) of cobalt acetate tetrahydrate (593 mg) (Acros Organics 98+%), lithium hydroxide monohydrate (100 mg) (Alfa Aesar, 98%), phosphoric acid

(163 μL) (Fisher Scientific, 85%) were dissolved in 10 mL of TEG. The vanadium substituted samples were produced by adding an appropriate amount of vanadium tri-isopropoxide (Alfa Aesar, 96%) while simultaneously decreasing the amount of cobalt acetate tetrahydrate. The specific amounts of precursors used to synthesize the various $LiCo_{1-3x/2}V_x\square_{x/2}PO_4$ are summarized in Table 4.1.

Table 4.1. Precursor amounts used to generate $LiCo_{1-3x/2}V_x\square_{x/2}PO_4$ samples

Sample	Precursor (mmol)[a]			
	LiOH	Co-Ac	H_3PO_4	V-Iso
$LiCoPO_4$	2.38	2.38	2.38	0.0
$LiCo_{0.97}V_{0.02}\square_{0.01}PO_4$	2.38	2.31	2.38	0.048
$LiCo_{0.94}V_{0.04}\square_{0.02}PO_4$	2.38	2.24	2.38	0.095
$LiCo_{0.91}V_{0.06}\square_{0.003}PO_4$	2.38	2.17	2.38	0.143
$LiCo_{0.88}V_{0.08}\square_{0.04}PO_4$	2.38	2.10	2.38	0.191

[a] Co-Ac and V-Iso refer, respectively, to cobalt acetate tetrahydrate and vanadium triisopropoxide.

Varying amounts of ammonium hydroxide (Fisher Scientific 14.8 N) were added to the samples with lower amounts of vanadium substitution, specifically, 60, 40, and 20 μL, respectively, for the x = 0.00, 0.02, and 0.04 samples. The addition of ammonia encouraged the formation of the *$Pn2_1a$* phase rather than the *Cmcm* phase, which was critical to ensure complete conversion of the MW-ST samples to *Pnma* at 525 ^oC.[81] The TEG was dried with 4A molecular sieves (Fisher Scientific) for more than 8 hours prior to use. The precursor solution was subjected to microwave-assisted solvothermal process with an Anton-Paar Monowave 300 in a 20 mL borosilicate vessel. The solutions were heated to 50℃ and stirred at 600 rpm for 5 min to ensure homogeneous mixing of the precursors. Subsequently, the solutions were heated as fast as possible with 850 W of power to 240℃, as measured by an infrared sensor, and held for 30 min. The average pressure inside the vessels remained below ~ 5 bar. Upon cooling, the samples were washed with acetone, sonicated for 5 min, and the product was than separated via centrifugation. This washing of the samples to remove the TEG was repeated 3 times. The samples were then dried at 100℃ in an air oven. The as produced samples were dark

blue in color and belonged to the *Pn2$_1$a* space group, as determined by x-ray diffraction. Samples, which had higher amounts of vanadium substitution, were darker blue than the unsubstituted $LiCoPO_4$. All the samples were then post fired at 525℃ in a ultra-high purity (UHP) 10% H_2 : 90% Ar atmosphere for 12 h. Upon calcination, all samples converted to the *Pnma* polymorph of $LiCo_{1-3x/2}V_x\square_{x/2}PO_4$.

4.3.2. Materials Characterization

Powder X-ray diffraction (XRD) diffraction patterns were taken in continuous mode over a 2θ range of 10 - 120° at two degrees per minute. The stoichiometry of the as-prepared $LiCo_{1-3x/2}V_x\square_{x/2}PO_4$ samples were determined by inductively coupled plasma optical emission spectroscopy (ICP-OES) with a Varian 715-ES instrument. The Varian 715-ES instrument was calibrated with lithium, vanadium, cobalt, and phosphorous standard solutions (Ricca Chemical Company).

4.3.3. Electrochemical Characterization

The electrodes were dried in a vacuum oven at 150 ^oC for > 24 h prior to making cells. Purolyte A6 electrolyte (Novolyte Technologies) comprising of a 1 : 1 ratio of dimethyl carbonate (DMC) and ethylene carbonate (EC) with 1 M lithium-tetrafluorophosphate ($LiPF_6$) was used. The cells were kept for at least 24 h prior to testing. Galvanostatic charge/discharge and cyclic voltammetry (CV) measurements were carried out on an Arbin Instruments test system. Electrochemical impedance spectroscopy (EIS) was performed on the cells with a Solartron 1260A impedance analyzer with a frequency sweep range of 1 MHz to 100 mHz.

4.4. Results and Discussion

4.4.1. Structure and Morphology

Single-phase $LiCo_{1-3x/2}V_x\square_{x/2}PO_4$ samples were obtained for nominal values of x = 0.0, 0.02, 0.04, 0.06, and 0.08. SEM micrographs (Figure 4.1) of the samples show nanoparticle morphology with average particles ranging in size from 100 to 500 nm. The performance of the low-conductivity LiMPO4 (M = Fe, Mn, Co) cathodes has been shown to depend upon morphology. The consistent morphology of the as-synthesized

$LiCo_{1-3x/2}V_x\square_{x/2}PO_4$ ensures that the subsequent electrochemical results should not be greatly influenced by the differences in sample morphologies. The precise stoichiometries of the samples were determined by ICP-OES data and are presented in Table 4.2. The ICP-OES results match closely to the nominal stoichiometries, with the exception of the nominal x = 0.08 sample actually having x = 0.07.

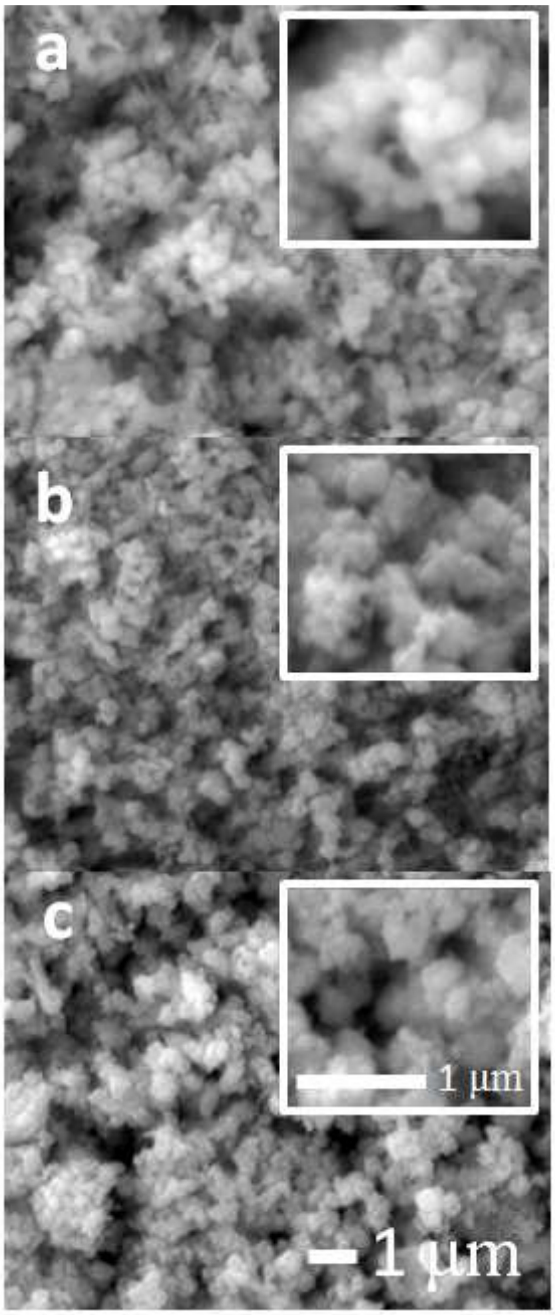

Figure 4.1. SEM micrographs of (a) LiCoPO4, (b) $LiCo_{0.94}V_{0.04}\square_{0.02}PO_4$, and (c) $LiCo_{0.88}V_{0.08}\square_{0.04}PO_4$

Attempts at synthesis of samples with vanadium contents higher than x = 0.08, yielded actual stoichiometry's of x <= 0.07. The samples with x > 0.08 were not single phase as evidenced by the impurity peaks in the powder XRD patterns and/or the lattice parameter of the samples no longer changed. It is not currently understood if the x = 0.08 is an intrinsic upper limit of vanadium substitution for cobalt or if this is a limitation of the synthesis conditions/method. All subsequent references to the $LiCo_{1-3x/2}V_x\square_{x/2}PO_4$ samples will use the nominal stoichiometry's for simplicity.

The as synthesized, MW-ST at 240℃, $LiCo_{1-3x/2}V_x\square_{x/2}PO_4$ samples' XRD peaks were indexed to the orthorhombic *Pn2₁a* space group. The post fired $LiCo_{1-3x/2}V_x\square_{x/2}PO_4$ samples' were indexed to the olivine structure, *Pnma* space group, with no un-indexed peaks. The conversion from *Pn2₁a* to *Pnma* space group started below 450℃ and was not complete until 525℃. Direct synthesis of the $LiCo_{1-3x/2}V_x\square_{x/2}PO_4$ *Pnma* polymorph in the microwave was not possible.

Table 4.2. ICP-OES results showing the chemical composition of V^{3+}-substituted $LiCo_{1-3x/2}V_x\square_{x/2}PO_4$

Sample	ICP stoichiometry		
	Li/P	Co/P	V/P
$LiCoPO_4$	0.98	0.97	--
$LiCo_{0.97}V_{0.02}\square_{0.01}PO_4$	0.99	0.95	0.02
$LiCo_{0.94}V_{0.04}\square_{0.02}PO_4$	1.04	0.94	0.03
$LiCo_{0.91}V_{0.06}\square_{0.003}PO_4$	0.98	0.91	0.06
$LiCo_{0.88}V_{0.08}\square_{0.04}PO_4$	1.01	0.87	0.07
All samples have estimated errors of < 4%			

Attempts to directly form the *Pnma* polymorph were not successful because the *Pn2₁a* phase was the preferred polymorph in the presence of vanadium isoproproxide. Heating of the $LiCo_{1-3x/2}V_x\square_{x/2}PO_4$ samples to 725 ^oC caused the formation of an

$Li_3V_2(PO_4)_3$ impurity (Figure 4.7), which is consistent with the results of previously reported low-temperature synthesis of vanadium substituted $LiFePO_4$ and $LiMnPO_4$ systems.[77,79] Furthermore, the $Li_3V_2(PO_4)_3$ is the expected impurity when attempting to substitute vanadium in the $LiMPO_4$ system (M = Fe, Mn) at high temperatures.[76,79,82,83] The lattice parameters and unit cell volumes were obtained by Reitveld refinement and the results are presented in Table 4.3.

Table 4.3. Crystallographic parameters of $LiCo_{1-3x/2}V_x\square_{x/2}PO_4$ as determined by Rietveld refinement

Sample	a (Å)	b (Å)	c (Å)	V (Å^3)	χ^2	R_{wp}
$LiCoPO_4$	10.20116	5.92342	4.70007	284.01	-	-
$LiCoPO_4$	10.1968(5)	5.9205(8)	4.7011(4)	283.814	1.64	21.2
$LiCo_{0.97}V_{0.02}\square_{0.01}PO_4$	10.1941(7)	5.9185(8)	4.7002(1)	283.587	1.58	21.5
$LiCo_{0.94}V_{0.04}\square_{0.02}PO_4$	10.1925(2)	5.9174(1)	4.6989(1)	283.406	1.45	23.7
$LiCo_{0.91}V_{0.06}\square_{0.03}PO_4$	10.1912(0)	5.9168(5)	4.6979(9)	283.287	1.75	21.8
$LiCo_{0.88}V_{0.08}\square_{0.04}PO_4$	10.1896(4)	5.9159(7)	4.6975(6)	283.176	1.60	17.9

The Reitveld refinement fitting to the X-ray powder diffraction patterns for the $LiCoPO_4$, $LiCo_{0.97}V_{0.02}\square_{0.01}PO_4$, $LiCo_{0.94}V_{0.04}\square_{0.02}PO4$, $LiCo_{0.91}V_{0.06}\square_{0.003}PO_4$ and $LiCo_{0.88}V_{0.08}\square_{0.04}PO_4$ samples are presented in, respectively, Figure 4.2, Figure 4.3, Figure 4.4, Figure 4.5, and Figure 4.6. The atomic positions and occupancies derived from each of the Rietveld simulations are presented in Table 4.4, Table 4.5, **Table 4.6**, Table 4.7, and Table 4.8, respectively.

Table 4.4. Atomic positions of $LiCoPO_4$ (*Pnma*)

Atom	Wyck.	x/a	y/b	z/c	Occ.
Li	4*a*	0.5000	0.5000	0.5000	1.000
Co	4*c*	0.2777	0.2500	0.9785	0.996
P	4*c*	0.0929	0.2500	0.4197	0.977
O1	4*c*	0.0992	0.2500	0.7431	0.997
O2	4*c*	0.4538	0.2500	0.2136	0.982
O3	8*d*	0.1630	0.0497	0.2810	0.994

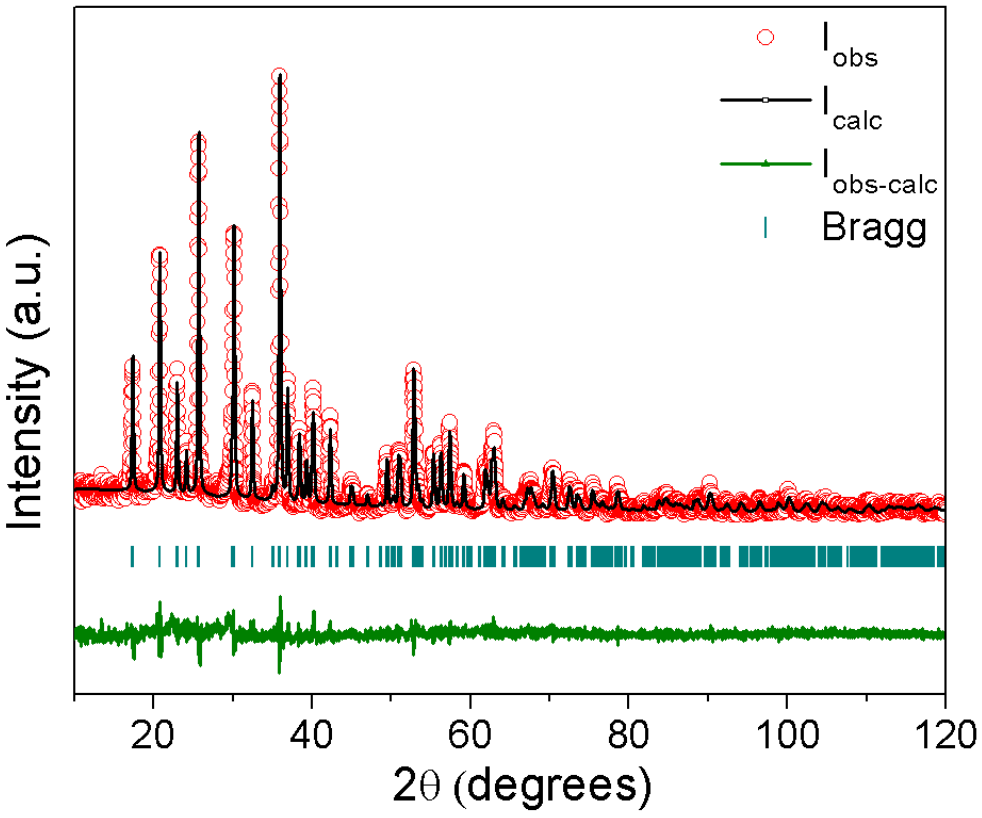

Figure 4.2. Rietveld refinement results of $LiCoPO_4$.

Table 4.5. Atomic positions of $LiCo_{0.97}V_{0.02}\square_{0.01}PO_4$ (*Pnma*)

Atom	Wyck.	x/a	y/b	z/c	Occ.
Li	4*a*	0.5000	0.5000	0.5000	1.000
Co	4*c*	0.2785	0.2500	0.9793	0.970
P	4*c*	0.0943	0.2500	0.4181	1.000
O1	4*c*	0.0996	0.2500	0.7399	1.000
O2	4*c*	0.4538	0.2500	0.2192	1.000
O3	8*d*	0.1615	0.0460	0.2820	1.000
V	4c	0.2785	0.2500	0.9793	0.016

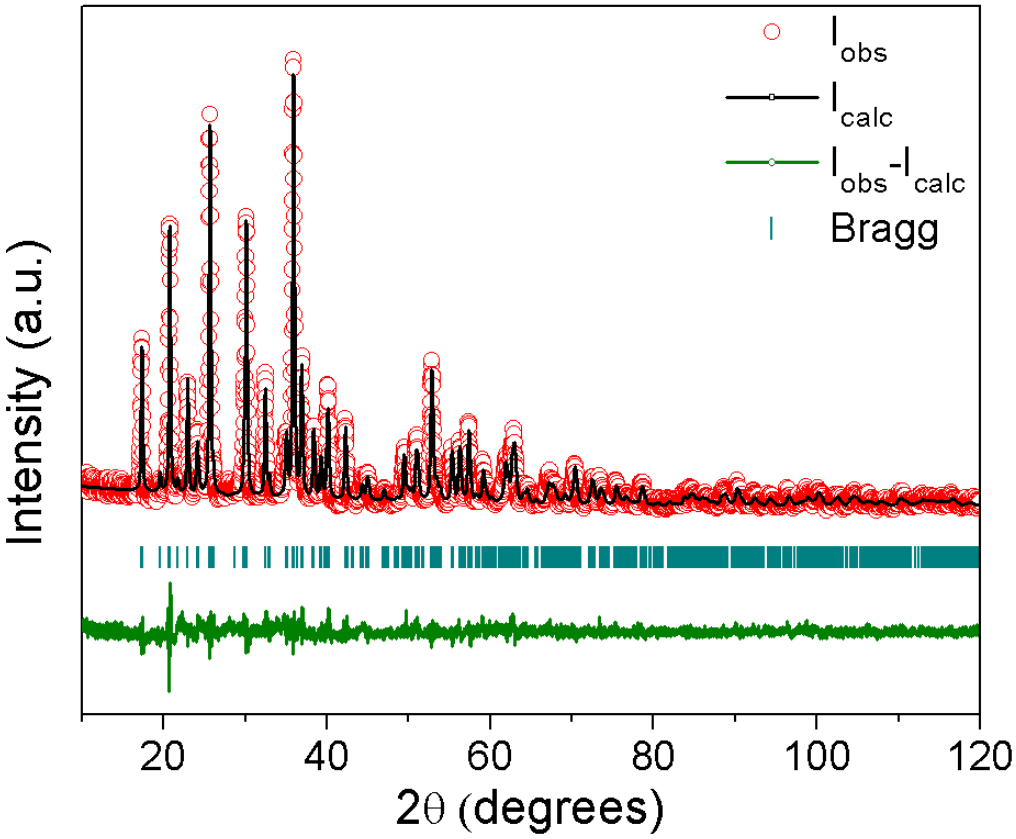

Figure 4.3. Rietveld refinement results of $LiCo_{0.97}V_{0.02}\square_{0.01}PO_4$.

Table 4.6. Atomic positions of $LiCo_{0.94}V_{0.04}\square_{0.02}PO_4$ (*Pnma*)

Atom	Wyck.	x/a	y/b	z/c	Occ.
Li	4*a*	0.5000	0.5000	0.5000	1.000
Co	4*c*	0.2788	0.2500	0.9801	0.934
P	4*c*	0.0941	0.2500	0.4181	1.000
O1	4*c*	0.0968	0.2500	0.7513	1.000
O2	4*c*	0.4554	0.2500	0.2134	1.000
O3	8*d*	0.1663	0.0461	0.2793	1.000
V	4c	0.2788	0.2500	0.9801	0.041

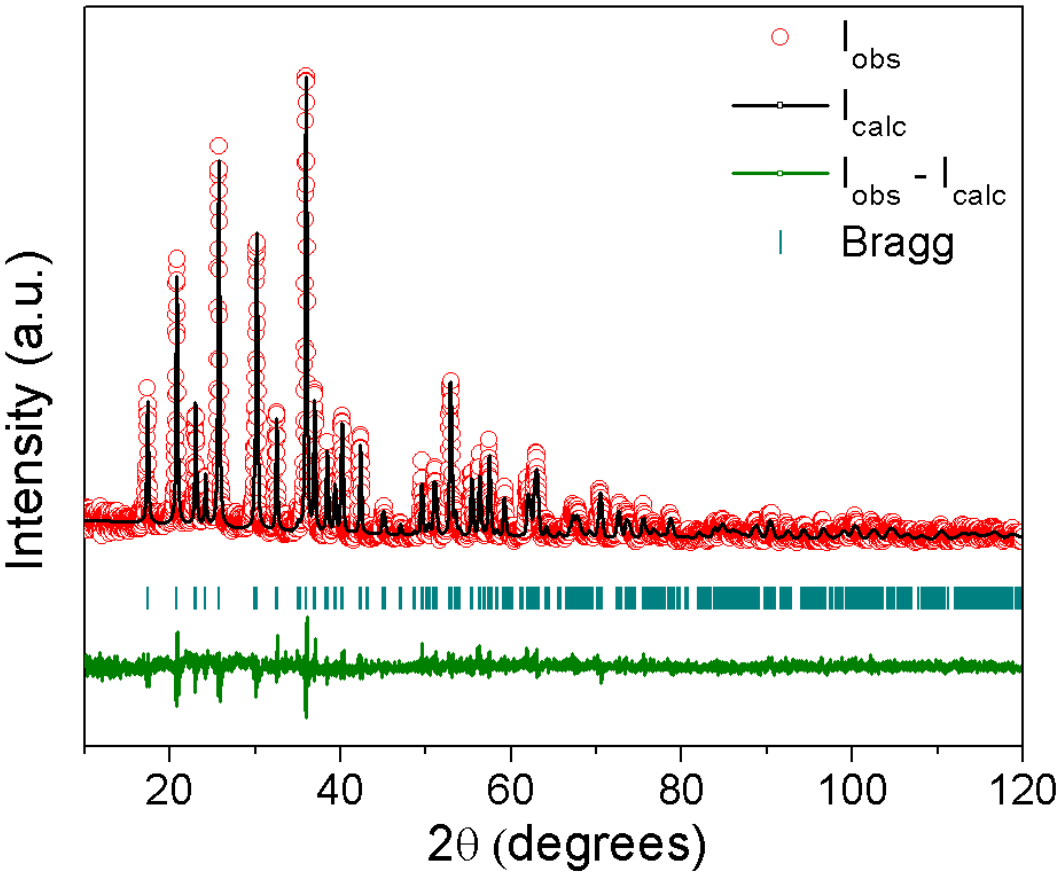

Figure 4.4. Rietveld refinement results of $LiCo_{0.94}V_{0.04}\square_{0.02}PO_4$.

Table 4.7. Atomic positions of $LiCo_{0.91}V_{0.06}\square_{0.03}PO_4$ (*Pnma*)

Atom	Wyck.	x/a	y/b	z/c	Occ.
Li	4*a*	0.5000	0.5000	0.5000	1.000
Co	4*c*	0.2788	0.2500	0.9823	0.880
P	4*c*	0.0926	0.2500	0.4131	1.000
O1	4*c*	0.1058	0.2500	0.7532	1.000
O2	4*c*	0.4561	0.2500	0.2155	1.000
O3	8*d*	0.1712	0.0375	0.2767	1.000
V	4c	0.2788	0.2500	0.9823	0.066

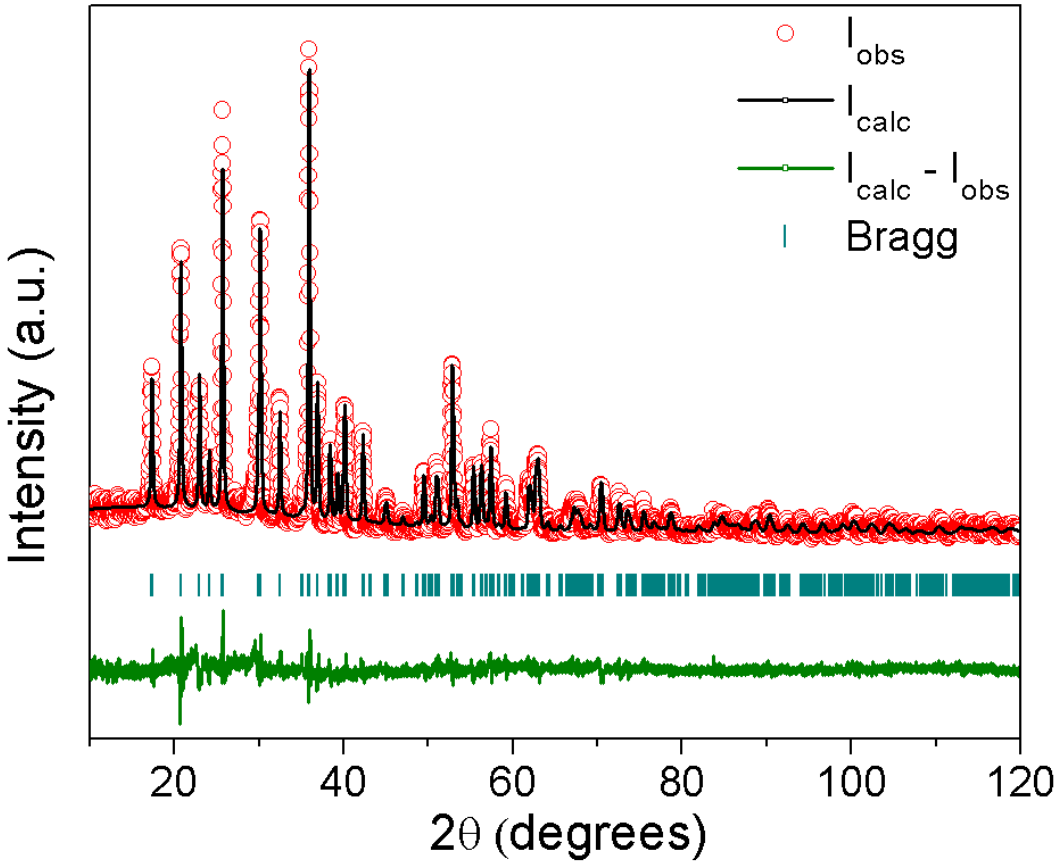

Figure 4.5. Rietveld refinement results of $LiCo_{0.91}V_{0.06}\square_{0.03}PO_4$.

Table 4.8. Atomic positions of $LiCo_{0.88}V_{0.08}\square_{0.04}PO_4$ (*Pnma*)

Atom	Wyck.	x/a	y/b	z/c	Occ.
Li	4*a*	0.5000	0.5000	0.5000	1.000
Co	4*c*	0.2720	0.2500	0.9783	0.904
P	4*c*	0.0943	0.2500	0.4179	1.000
O1	4*c*	0.0971	0.2500	0.7452	1.000
O2	4*c*	0.4583	0.2500	0.2152	1.000
O3	8*d*	0.1692	0.0429	0.2827	1.000
V	4c	0.2887	0.2500	0.9783	0.062

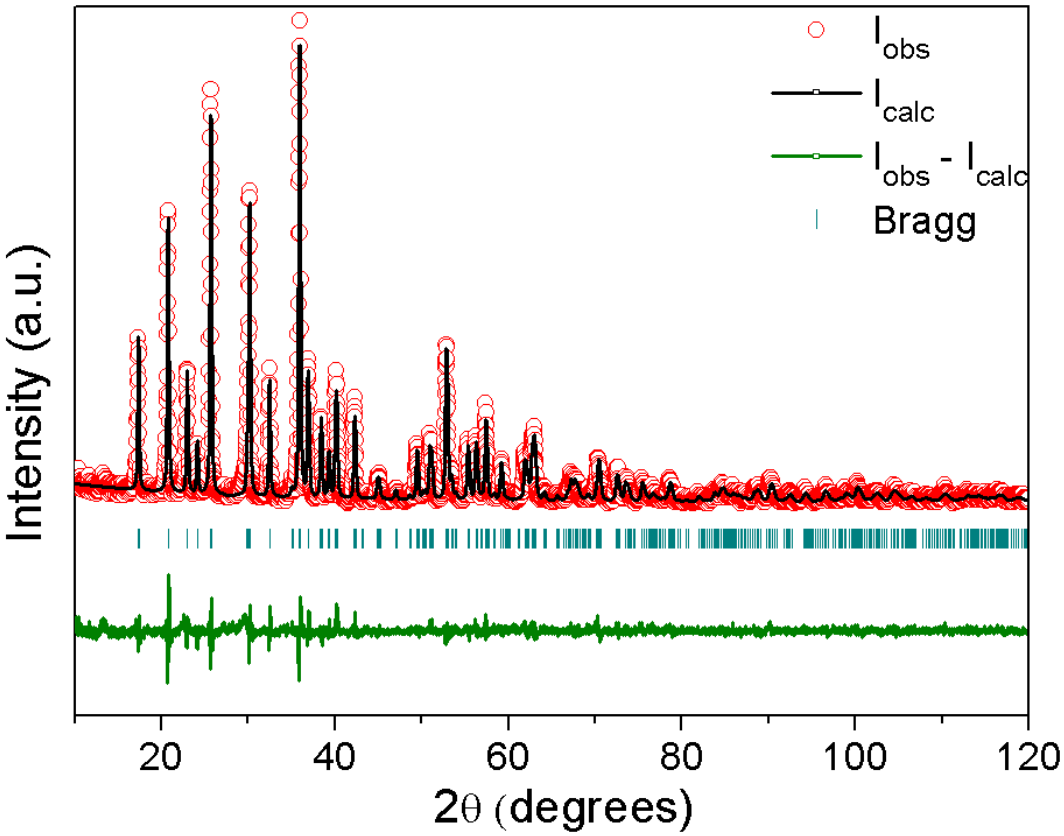

Figure 4.6. Rietveld refinement results of $LiCo_{0.88}V_{0.08}\square_{0.04}PO_4$.

The dependence of $LiCo_{1-3x/2}V_x\square_{x/2}PO_4$ lattice parameters on vanadium content is shown in Figure 4.8. The estimated standard deviation (ESD) in the lattice parameters was determined through Rietveld refinement and the error bars are shown in Figure 4.8. A systematic decrease in all three lattice parameters, (*a*, *b*, and *c*) and the unit cell volume is observed with increasing vanadium substitution. The lattice parameter *a* decreases more in absolute terms than both *b* and *c*, but the lattice parameters change by roughly the same percentage. The lattice parameters and the cell volume of $LiCoPO_4$ agree closely with the standardized parameters reported in Pearson's crystolgraphic database entry number 1629172. Furthermore, the interpolated percentage change in the unit cell volume of $LiCo_{0.925}V_{0.05}\square_{0.025}PO_4$ (283.32 $Å^3$) represents a decrease of 0.17% compared to those with $LiMn_{0.925}V_{0.05}\square_{0.025}PO_4$[79] and $LiFe_{0.925}V_{0.05}\square_{0.025}PO_4$,[76] which decreased by 0.36% and 0.18%, respectively. Therefore, the observed decrease in the unit cell volume of $LiCo_{0.925}V_{0.05}\square_{0.025}PO_4$ is very similar to that of $LiFe_{0.925}V_{0.05}\square_{0.025}PO_4$.

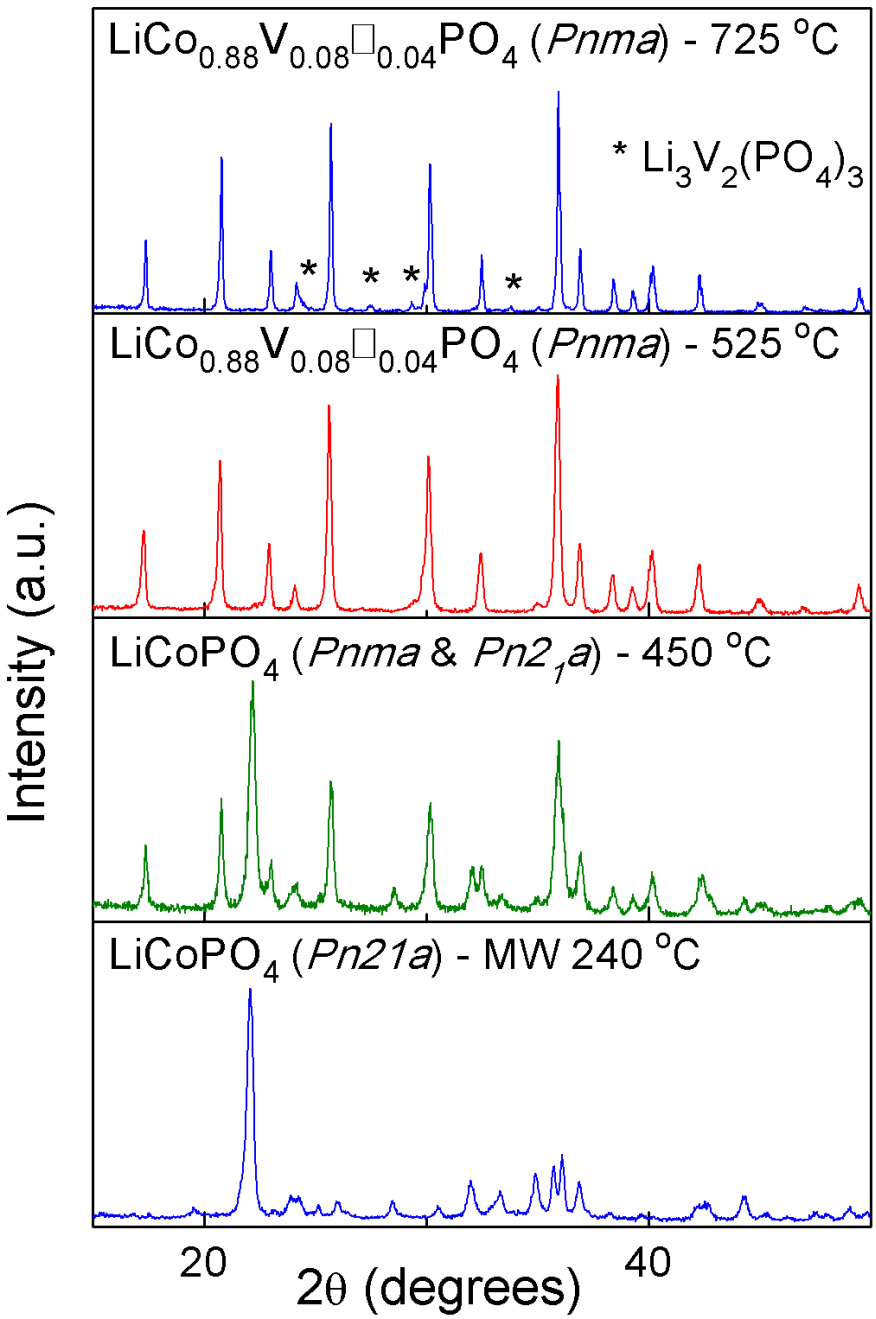

Figure 4.7. XRD patterns of the as-synthesized $LiCo_{1-3x/2}V_x\square_{x/2}PO_4$, and the samples obtained by subsequent conversion to Pnma space group upon heat treatment.

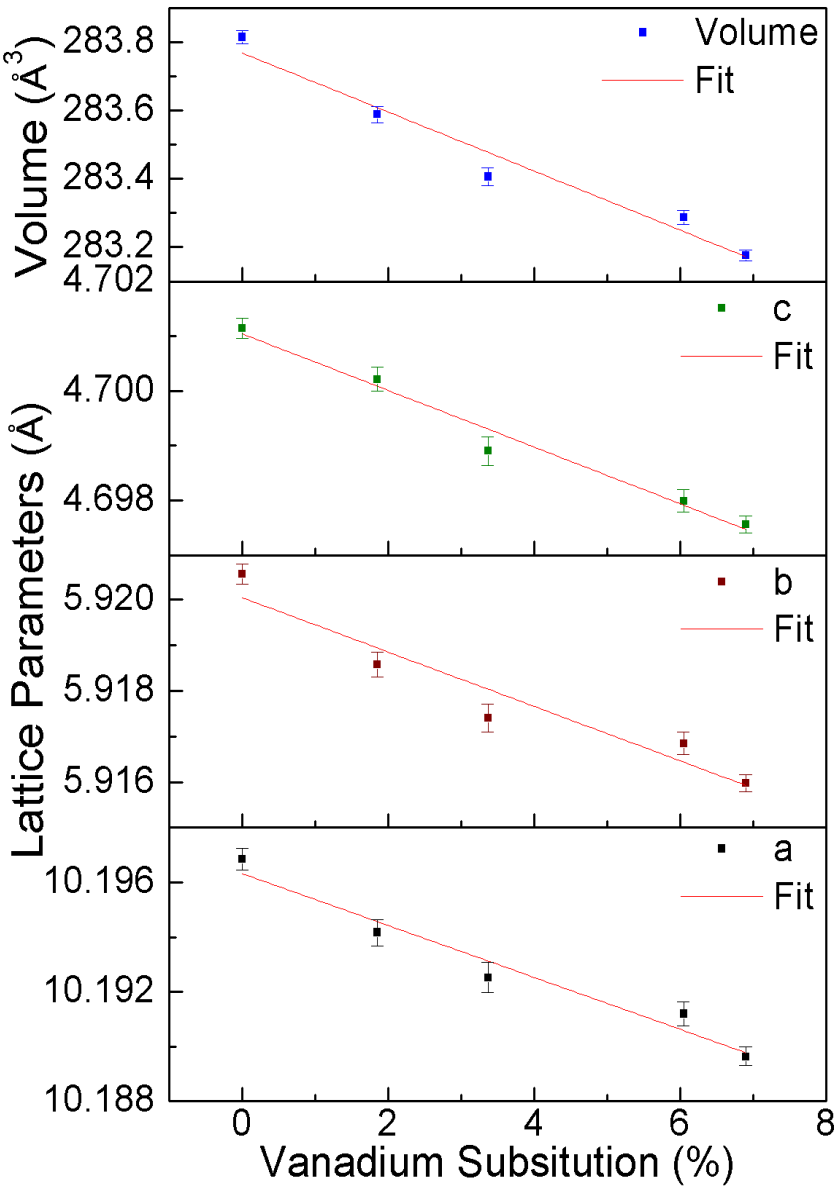

Figure 4.8. Variations of the lattice parameters and unit cell volume with vanadium content.

4.4.2. Materials Characterization

Energy dispersive spectroscopy was performed on the as-synthesized $LiCo_{1-3x/2}V_x\square_{x/2}PO_4$ samples to ensure that there were no vanadium rich or poor regions within the sample. The lack of vanadium rich regions indicates a single-phase solid solution rather than a segregation of the vanadium and the cobalt. The result of the EDS and the corresponding SEM image are shown in Figure 4.9. The FTIR spectra of the $LiCo_{1-3x/2}V_x\square_{x/2}PO_4$ samples are presented in Figure 4.10. The absorption peaks located at 900 - 1200 cm^{-1} are due to the bond stretching of the PO_4^{-3} anions, while the peaks located within the 400 – 700 cm^{-1} range are caused by the bending modes[64]. Specifically, the 988 cm^{-1} band corresponds to the symmetric stretching mode υ_1. The three absorbance bands located within the 1020 - 1170 cm^{-1} range correspond to the antisymmetric stretching υ_3 mode and are caused by the site symmetry of the PO_4^{3-} anion.[65] The FTIR patterns of the vanadium substituted samples have minor differences compared to the unsubstituted $LiCoPO_4$. Specifically, the absorbance peak located at 988 cm^{-1} corresponding to the υ_1 mode shifts to lower wave numbers with increasing vanadium substitution. Additionally, the FTIR patterns do not show any absorbance peaks associated with an $Li_3V_2(PO_4)_3$ impurity, which agrees with the XRD results and indicates phase-pure samples.

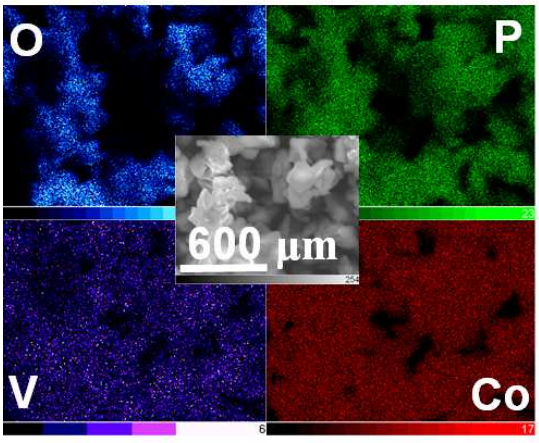

Figure 4.9. Elemental map of $LiCo_{0.91}V_{0.06}\square_{0.03}PO_4$ and the corresponding SEM image.

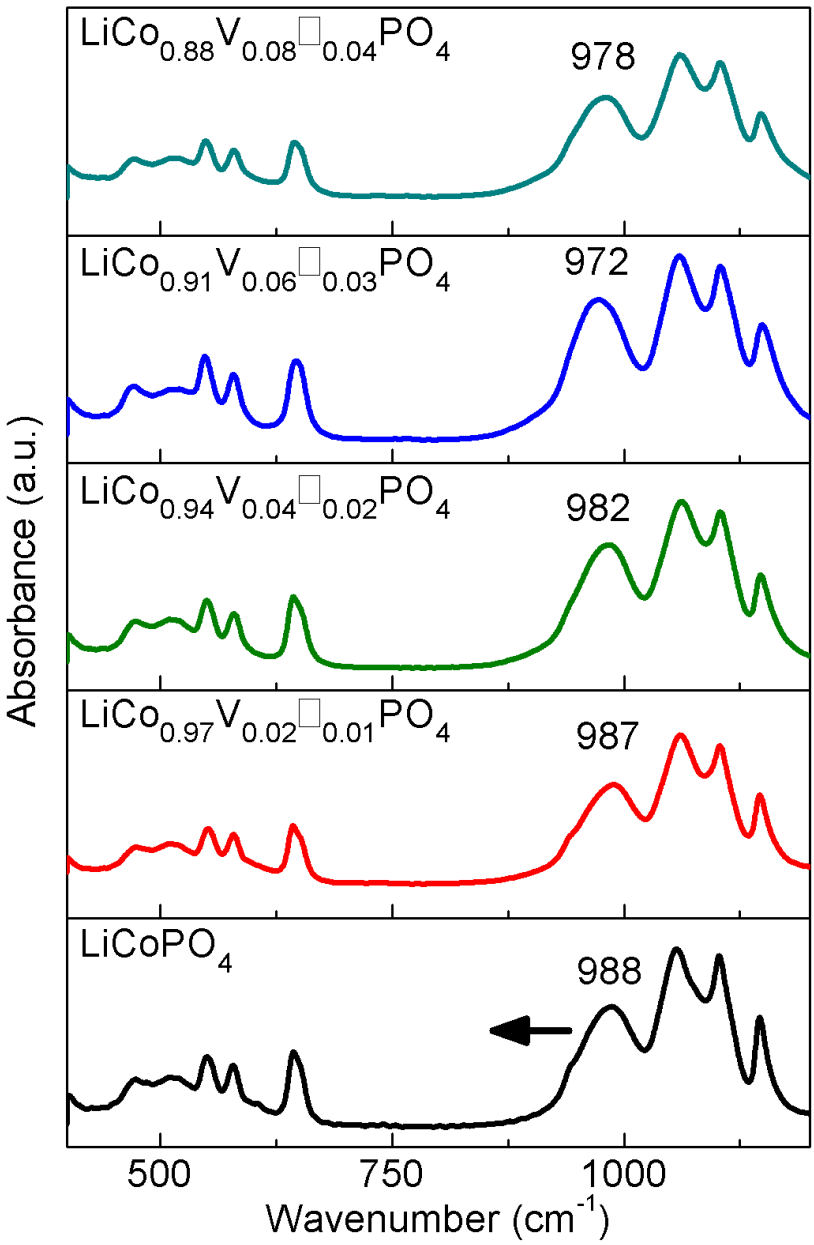

Figure 4.10. FTIR spectra of the $LiCo_{1-3x/2}V_x\square_{x/2}PO_4$ samples.

4.4.3. Electrochemical Characterization

The $LiCo_{1-3x/2}V_x\square_{x/2}PO_4$ materials were characterized by both cyclic voltammetry as well as galvanostatic charge/discharge. The cyclic voltammograms were generated at a scan rate of 0.05 mV-s^{-1}. The CV test results are presented in Figure 4.11.

$LiCoPO_4$ has redox peaks at 4.87 & 4.97 V with a considerable polarization of 0.257 V between the higher potential charge and the discharge peaks. The polarization decreases with increasing vanadium substitution, and reaches a minimum of 0.193 V for $LiCo_{0.91}V_{0.06}\square_{0.03}PO_4$, corresponding to an upper redox peak potential of 4.92 V. Although the $LiCo_{0.88}V_{0.08}\square_{0.04}PO_4$ sample breaks the trend of decreasing polarization, it is still lower than that of $LiCoPO_4$. The decrease in polarization is an evidence of increased electronic and/or ionic conductivity with vanadium substitution. The increase in electrical conductivity could be due to increased Co-O bond hybridization in the vanadium substituted samples. Additionally, the lower potential redox peak at ~ 4.85 V during charge appears to diminish with increasing vanadium substitution. The change in the redox peaks may be an indication of change in the two-phase behavior of $LiCoPO_4$.[22]

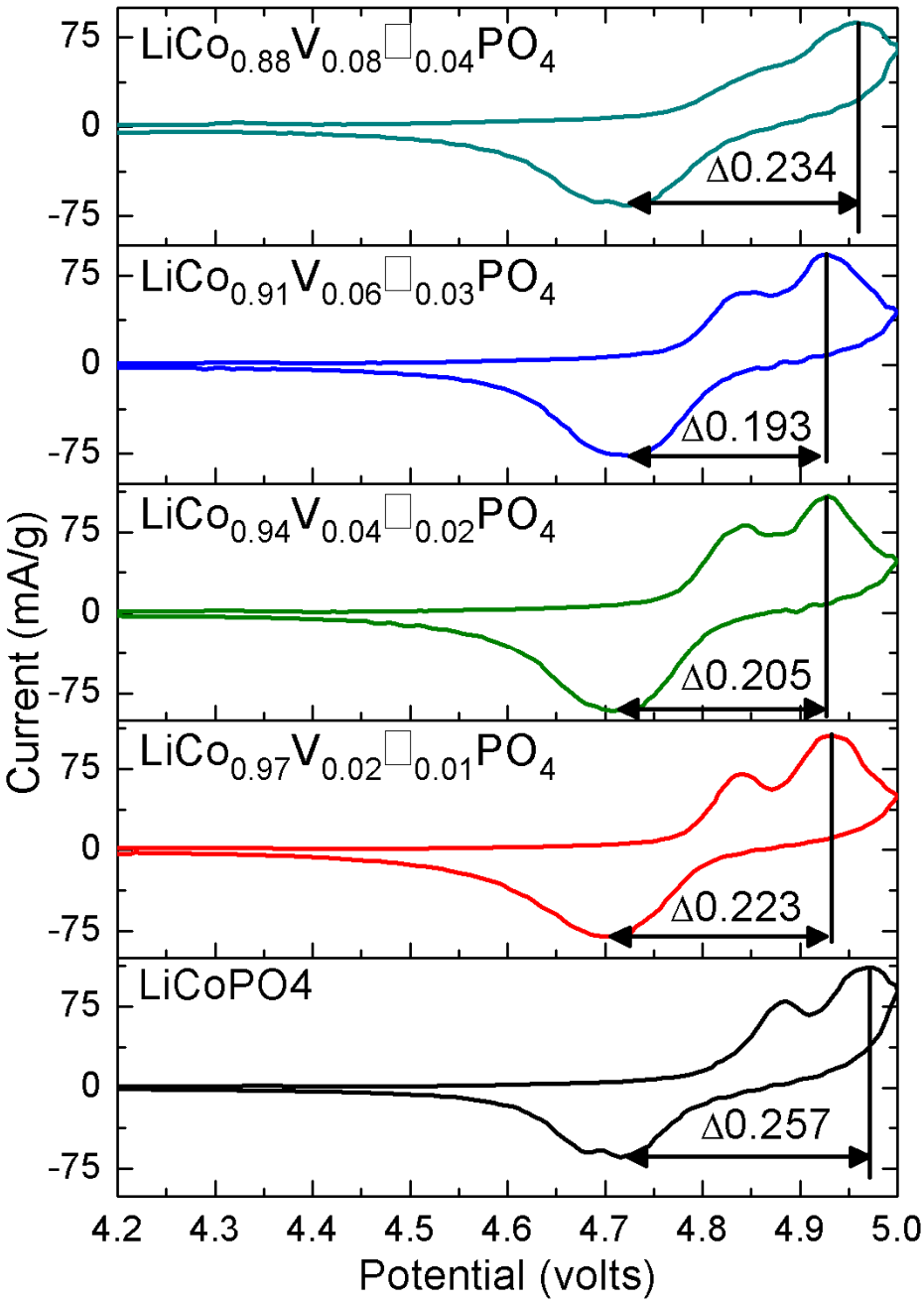

Figure 4.11. Cyclic Voltammagrams of $LiCo_{1-3x/2}V_x\square_{x/2}PO_4$ samples cycled at 3 – 5 V at a rate of 0.05 mV s^{-1}.

Galvanostatic charge/discharge tests were performed on the $LiCo_{1-3x/2}V_x\square_{x/2}PO_4$ samples to elucidate the effect of the substitution on cyclability. No additional attempts were

made to optimize the electrode construction. Although various extrinsic methods, such as ball milling and coating with a conductive polymers or carbon, have been shown to increase the performance of $LiCoPO_4$, these methods were not employed to avoid convolution of the results.[70–72] These materials were tested with 20% conductive carbon to prevent post synthesis treatments from complicating the comparisons of the $LiCo_{1-3x/2}V_x\square_{x/2}PO_4$ samples. The $LiCo_{1-3x/2}V_x\square_{x/2}PO_4$ samples had a first cycle discharge capacity of 69, 115, 99, 94, and 97 mAh/g for x = 0, 0.02, 0.04, 0.06, and 0.08, respectively. Thus, all the vanadium substituted samples showed higher first cycle capacity compared to the $LiCoPO_4$ sample. The $LiCo_{0.97}V_{0.02}\square_{0.1}PO_4$ sample achieved the highest first cycle capacity but faded much more quickly than the samples with higher amount of vanadium substitution.

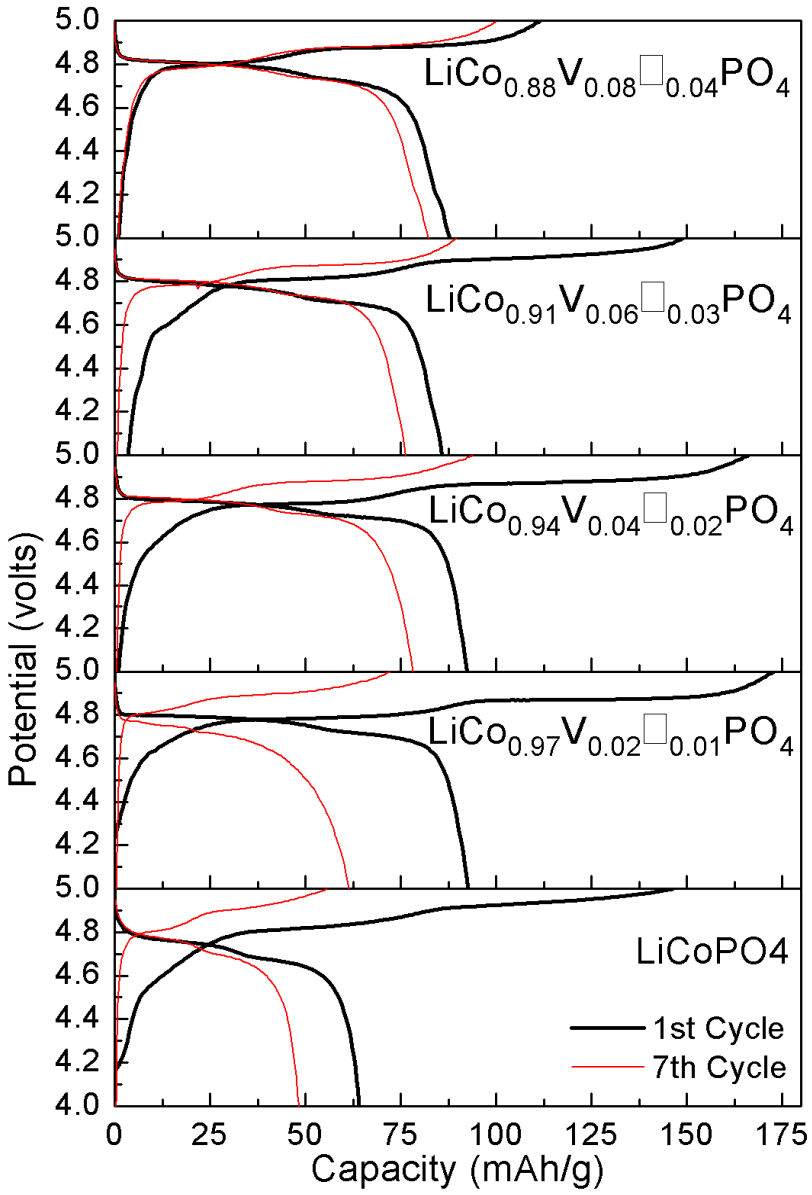

Figure 4.12. Galvanostatic first charge/discharge of the $LiCo_{1-3x/2}V_x\square_{x/2}PO_4$ samples at 3.0-5.0 V at a rate of C/10.

The cyclability of the $LiCo_{1-3x/2}V_x\square_{x/2}PO_4$ samples are shown in Figure 4.12. After 20 cycles, the x = 0.08 samples had the highest retained discharge capacity of ~ 82 mA h g^{-1}. Not only did vanadium substitution increase the first cycle capacity of $LiCoPO_4$, but it also enhances the cycle life.

Electrochemical impedance spectroscopy was performed on the $LiCo_{1-3x/2}V_x\square_{x/2}PO_4$ samples to determine the effect of vanadium substitution on conductivity. EIS was

performed on the as-prepared, fully discharged, coin cells after being rested for at least 24 h. The results of EIS are shown in Figure 4.14. The semicircle is a combination of the electrode resistance and the charge-transfer impedance of the electrode-electrolyte interface. Since the charge-transfer impedance should be similar for each of the samples, due to similar morphology, the decrease in the semicircle size can be largely attributed to a decrease in the electrode resistance.

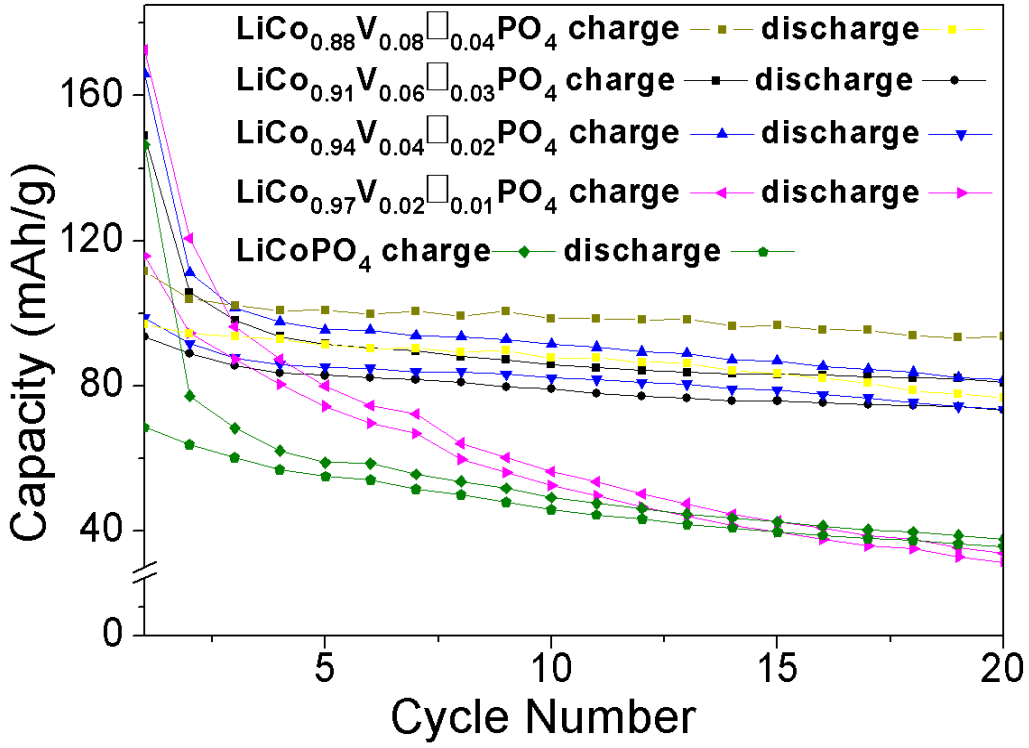

Figure 4.13. Cyclability of the $LiCo_{1-3x/2}V_x\square_{x/2}PO_4$ samples between 3 and 5 V at C/10 rate.

The Warburg impedance, which is associated with the Li-ion diffusion in the electrode material, is shown in Figure 4.15. The $LiCo_{1-3x/2}V_x\square_{x/2}PO_4$ samples show lower Warburg impedance corresponding to higher lithium-ion diffusion with increasing vanadium content. The lithium-ion diffusion coefficient can be calculated by the following equation:

$$D_{Li^+} = \frac{R^2T^2}{2A^2n^4F^4C^2\sigma^2}$$

where *R* is the gas constant (8.314 J-mol^{-1}-K^{-1}), *T* is temperature, *A* is electrode area, *n* is number of electrons per molecule, C is lithium ion concentration, F is Faraday's constant (96,486 C-mol^{-1}), and sigma is the slope of the Warburg impedance. The value for the lithium ion diffusion coefficient were calculated based on the Warburg impedance measurement and are presented in Table 4.9.

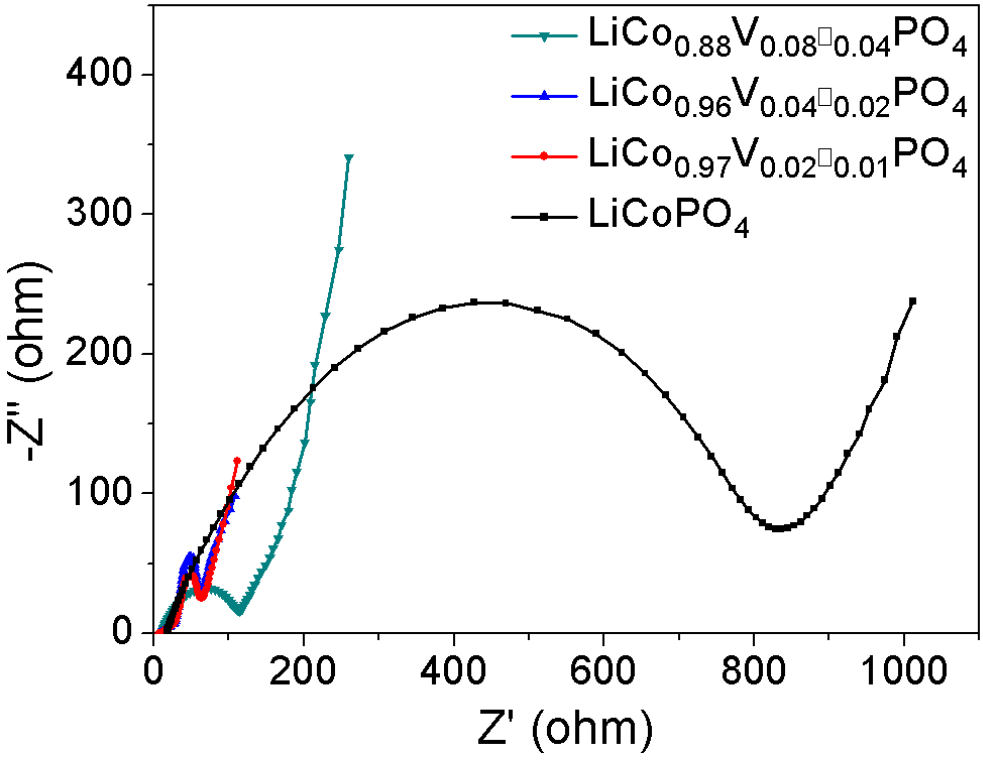

Figure 4.14. Electrochemical impdedance spectroscopy of the $LiCo_{1-3x/2}V_x\square_{x/2}PO_4$ samples, with the real impedance on abscissa and the imaginary impedance on ordinate.

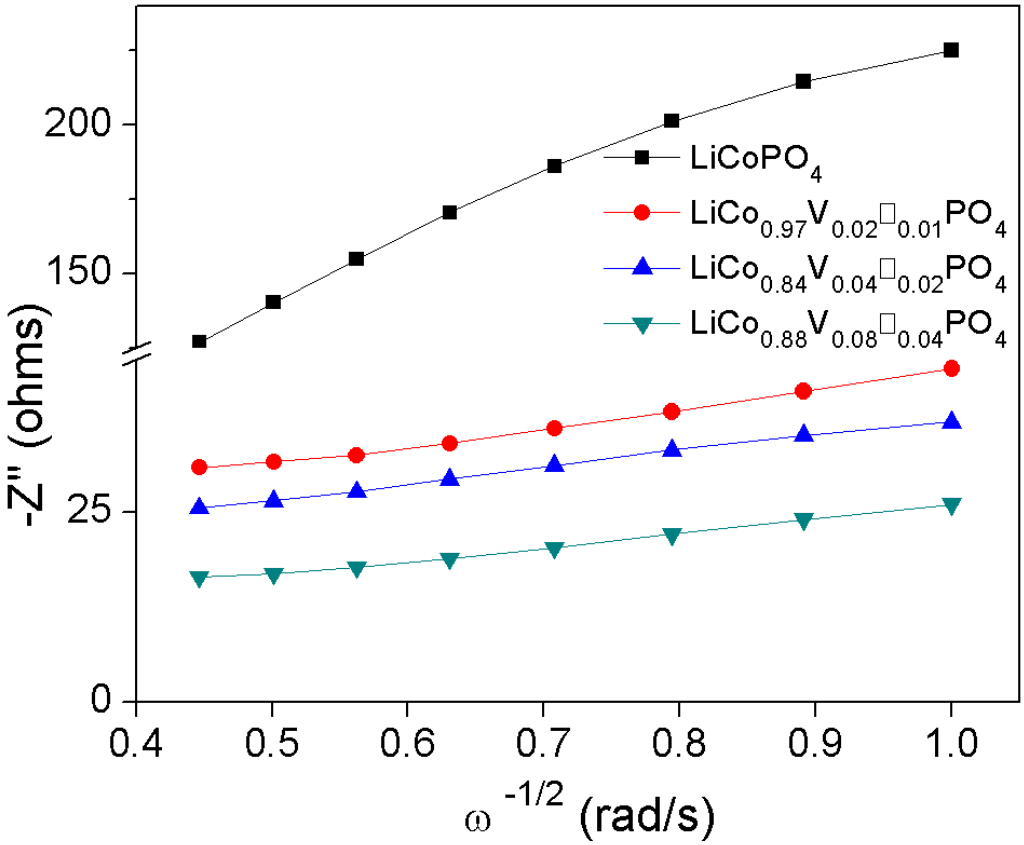

Figure 4.15. Warburg impedance of the $LiCo_{1-3x/2}V_x\square_{x/2}PO_4$. Samples, with the real impedance on abscissa and reciprocal square-root of frequency on the ordinate.

Table 4.9. Computed lithium diffusion coefficients of $LiCo_{1-3x/2}V_x\square_{x/2}PO_4$ samples from Warburg impedance

Sample	σ	D_{Li}^+ (cm^2-s^{-1})
$LiCoPO_4$	181.13	6.54e-15
$LiCo_{0.97}V_{0.02}\square_{0.01}PO_4$	23.99	3.73e-13
$LiCo_{0.94}V_{0.04}\square_{0.02}PO_4$	21.26	4.75e-13
$LiCo_{0.88}V_{0.08}\square_{0.04}PO_4$	17.84	6.74e-13

Interestingly, the electrode resistance actually increases for the x = 0.08 sample compared to the x = 0.02 and 0.04 samples, while the Warburg impedance decreases systematically with increasing vanadium content. This may be explained by the vanadium substitution causing two intrinsic but competing changes to $LiCoPO_4$ with

vanadium substitution, specifically electronic and ion conductivity. The electronic conductivity is initially enhanced with vanadium substitution due to the introduction of new charge carriers, but ultimately begins to decrease due to the increasing number of Co-site vacancies. Simultaneously, the increase in Li-ion diffusion may be due to the Co site vacancies providing additional path-ways for lithium-ion diffusion by allowing 2-D diffusion rather than 1-D diffusion known to take place in unsubstituted $LiCoPO_4$.

4.5. Conclusion

Vanadium-substituted $LiCo_{1-3x/2}V_x\square_{x/2}PO_4$ (*Pn2₁a* space group) samples have been synthesized by a low-temperature microwave-assisted solvothermal method, followed by subsequent conversion to the *Pnma* space group by calcination in an inert atmosphere. The substitution of vanadium was verified by the change in the unit cell volume with vanadium substitution as well as energy dispersive x-ray spectroscopy for values of $x \leq 0.07$. Vanadium substitution initially increases the electrical conductivity of the samples as indicated by the reduced polarization in the CVs and the reduced electrode resistance in the EIS data. Larger amounts of vanadium substitution continue to increase the ionic conductivity while subsequently decreasing the electronic conductivity. The cyclability of the $LiCo_{1-3x/2}V_x\square_{x/2}PO_4$ samples increase with increasing substitution with over double the retained capacity of $LiCoPO_4$ after 20 cycles. Overall, vanadium substitution enhances the electrochemical performance of $LiCoPO_4$ and further investigation with more optimized high-voltage electrolytes could offer additional improvements in performance.

Chapter 5: Vanadium-substituted $LiCoPO_4$ core with a monolithic $LiFePO_4$ shell for high-voltage lithium-ion batteries[3]

5.1. Abstract

High-voltage lithium-ion cathodes are a promising solution to achieving higher energy density batteries. However, the use of high-voltage cathodes is presently limited by the irreversible chemical reactions occurring between the cathode and the electrolyte at the high operating voltages. Metal-oxide coatings on micrometer sized high-voltage cathode materials have been employed to improve the electrochemical performance, but it is often difficult to achieve a robust, durable, monolithic coating, especially on nanoparticles. This study presents a novel low-temperature microwave-assisted solvothermal process for realizing a robust, monolithic coating of $LiFePO_4$ on the high-voltage (~ 4.8 V) $LiCo_{1-3x/2}V_x\square_{x/2}PO_4$ (x = 0, 0.02, and 0.04) nanoparticles, offering a stable cathode-electrolyte interface. The core-shell cathode obtained exhibit enhanced electrochemical performance compared to the uncoated sample with an initial discharge capacity of 145 mAh/g. A lower operating voltage of $LiFePO_4$ (~ 3.4 V) raises the Fermi energy of the cathode surface above the energy of the highest occupied molecular orbital (HOMO) of the electrolyte, offering a chemically stable cathode-electrolyte interface analogous to the stable solid-electrolyte interphase layer formed on carbon anodes.

5.2. Introduction

Lithium-ion batteries (LIBs) are facilitating the initial adoption of full electric vehicles. Further proliferation of electric vehicles requires a new generation of batteries having higher energy density compared with the batteries used today. Polyanion cathode materials are a promising group of materials that could offer higher energy densities through higher operating voltages with enhanced safety.

[3] This chapter is based on previously published work: K. Kreder, A. Manthiram, "Vanadium-Substituted $LiCoPO_4$ Core with a Monolithic $LiFePO_4$ Shell for High-Voltage Lithium-Ion Batteries," *ACS Energy Letters*, 2, 64-69 (2017).

In the 1980's, Manthiram and Goodenough investigated $Fe_2(XO_4)_3$ (X = Mo, W, S) polyanion cathode materials for LIBs.[49,50] Polyanion materials are interesting because of their higher operating voltages compared to the corresponding metal-oxide redox couple due to the inductive effect. Subsequently, Goodenough's group developed $LiFePO_4$, which, unfortunately, suffered from low electrical conductivity.[13,84] The groups of Nazar and Hinokuma showed that the intrinsically low electrical conductivity of $LiFePO_4$ could be overcome by employing nano-sized particles.[16,74] Presently, the higher voltage phosphates $LiMPO_4$ with M = Co and Ni are of much interest due to their higher operating voltages and energy density compared to $LiFePO_4$. Similar to $LiFePO_4$, the higher-voltage analogues also suffer from low electrical conductivity.[20,85] Improvements have been made in the electrochemical performance of $LiMPO_4$ (M = Mn and Co) through both nano-sizing as well as doping.[53,79,18,19,86–89]

Unfortunately, most high-voltage cathode materials operate outside the electrochemical stability limit of liquid electrolytes. The incompatibility of the electrochemical potential of the cathode with the electrolyte causes irreversible side reactions during cycling, which consumes the electrolyte and causes capacity fade.[3,90,91] There have been numerous attempts to introduce new electrolytes and additives that are stable at higher voltages.[83,2,92–97] Unfortunately, all of these novel electrolytes either suffer from low-ionic conductivity at low temperatures, and/or a very high cost. This has prevented the high-voltage cathodes from being put into wide use. Interestingly, the most commonly used anode material in lithium-ion batteries, graphitic carbon, is also outside the electrochemical stability window of most commonly used electrolytes. However, in the case of carbon, a self-limiting solid electrolyte interphase (SEI) layer forms, which prevents the further degradation of the anode, as illustrated in Figure 5.1.

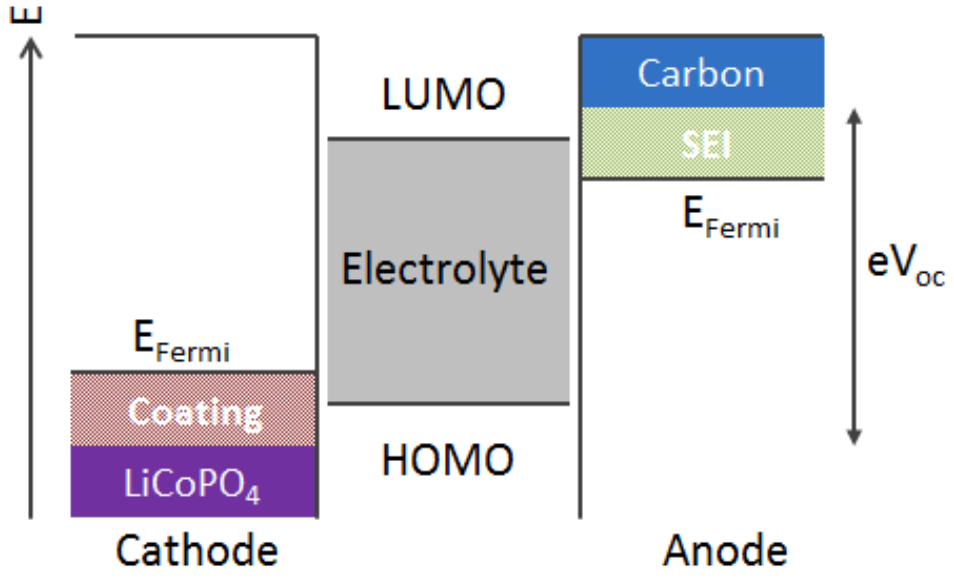

Figure 5.1. Fermi energies of the anode and cathode relative to the highest occupied molecular orbital (HOMO) and the lowest unoccupied molecular orbital (LUMO) of the electrolyte. The illustration also shows the lowering of the Fermi energy of a carbon anode by the SEI layer, and the analogous raising of the Fermi energy with the coating of the $LiCoPO_4$ cathode with $LiFePO_4$.

The in situ formation of the anodic SEI layer was a serendipitous consequence of using organic carbonate electrolytes.[98,37] The formation of the SEI layer lowers the Fermi energy of the anode surface below that of the lowest unoccupied molecular orbital (LUMO), creating a chemically stable interface. Unfortunately, the interactions of current high-voltage cathode materials, which are outside the electrochemical stability window of the electrolyte, do not form a stable SEI *in situ*. Therefore, a promising area of research is to form a stable monolithic SEI layer on the cathode particles *ex situ*, prior to making a battery electrode. The coating of the high-voltage (~ 4.8 V) $LiCoPO_4$ cathode with the lower-voltage (~3.5 V) $LiFePO_4$ can raise the Fermi energy of the cathode surface above the energy of the highest occupied molecular orbital, creating a chemically stable interface analogous to the *in-situ* SEI layer formed on carbon anodes.

Previously, our group has demonstrated enhanced electrochemical cyclability with $LiCoPO_4$ through an aliovalent substitution of V^{3+} for Co^{2+}, which enhances the electronic and ionic conductivity.[89] Unfortunately, all of the $LiCoPO_4$ materials which

we have previously investigated suffer from low coulombic efficiency, attributable to both the bulk instability of $LiCoPO_4$ as well as the interactions with the electrolyte at high potentials. We present here a novel low-temperature, low-pressure microwave-assisted solvothermal (MW-ST) method of coating $LiCo_{1-3x/2}V_x\square_{x/2}PO_4$ (LCVP) (x = 0, 0.02, 0.04) with 5 wt. % $LiFePO_4$ (LFP). The as-prepared LFP-coated LCVP (hereafter denoted as LFP-LCVP) materials are then characterized with x-ray diffraction (XRD), transmission electron microscopy (TEM), energy dispersive spectroscopy (EDS), x-ray photoelectron spectroscopy (XPS) and electrochemical properties measurements in lithium-ion cells.

5.3. Experimental Methods

5.3.1. Microwave-assisted Solvothermal Synthesis

Several vanadium substituted nanoparticle LCVP powders were synthesized as described elsewhere. In brief, stoichiometric 1 : 1-3x/2 : x : 1 ratio of lithium hydroxide monohydrate (100mg) (Alfa Aesar, 98%), cobalt acetate tetrahydrate (Acros Organics 98+%), vanadium tri-isopropoxide (Alfa Aesar, 96%), and phosphoric acid (Fisher Scientific, 85%) were mixed with 12 mL of dry tetraethylene glycol (TEG) (Sigma-Aldrich 99%). This mixture was than heated to 240 ^oC in an Anton-Paar microwave reactor for 30 min. The samples were washed with acetone thrice. The LCVP powders obtained were then post heated in an argon atmosphere at 525 ^oC for 4 h. Subsequently, 200 mg of the synthesized LCVP powders were placed in a 20 mL borosilicate reaction vessel with 12 mL of TEG and appropriate amounts of lithium hydroxide monohydrate, iron acetate (Alfa Aesar, 98%), and phosphoric acid to form LFP. The solution was stirred and sonicated for 10 min to ensure the dispersion of the LCVP particles as well as the dissolution of the LFP precursors. The solution was then heated as fast as possible with 850 W of power to 260 ^oC and held for 15 min. The synthesized LFP-coated LCVP materials were then washed with acetone three times and dried in an air oven. They were then post calcined in an argon atmosphere at 525 ^oC for 4 h.

5.4. Materials Characterization

The nature and morphology of the MW-ST LFP-LCVP materials were investigated with a JEM-2100F high-resolution TEM with an accelerating voltage of 200 kV. Energy dispersive spectroscopy (EDS) was performed on the JEM-2100F with an Oxford Instruments detector while operating in the scanning transmission electron microscopy (STEM) mode. Powder x-ray diffraction (XRD) patterns were taken over a range of 10-80^{o} 2θ in continuous mode at a rate of 3 degrees per minute. Inductively coupled plasma - optical omission spectroscopy (ICP-OES) performed on a Varian 715-ES and was used to determine the chemical composition of the samples. The ICP-OES was calibrated with solutions made with lithium, cobalt, vanadium, iron, and phosphorous standards (Ricca Chemical Company). X-ray photoelectron spectroscopy was performed was performed on both the uncoated LCVP and coated LFP-LCP samples. Two separate peaks were used to fit both the Co $2p_{3/2}$ and Co $2p_{1/2}$ peaks due to the existence of satellite peaks common to $LiCoPO_4$ materials. The Co $2p_{3/2}$ peaks were constrained to have the same full width half max (FWHM) as their corresponding Co $2p_{1/2}$ peaks as well as having 2 times the area. The atomic percentage of the Co, Fe, P, and O in the iron containing sample were determined by the area under, respectively, the Co $2p_{1/2}$, Fe 2p, P 2p, and O 1s peaks with the proper relative sensitivity factors.

5.4.1. Electrochemical Characterization

The electrochemical properties of the LFP-LCVP samples were assessed by making CR 2032 coin cells from the synthesized powders. Composite electrodes were made as described in chapter 2. Electrolyte was prepared by mixing a 3 : 7 ratio of ethylene-carbonate (EC) ethylmethylcarbonate (EMC) and adding 1 M of lithium-tetraflourophosphate ($LiPF_6$). The cells were allowed to rest for 24 h prior to cycling. An Arbin instruments test system was used to conduct cyclic voltammetry (CV) and galvanostatic charge/discharge tests of the cells.

5.5. Synthesis method

The novel method of creating nano-scale core-shell particles with a microwave-assisted solvothermal method, and the mechanism of why it works needs elaboration.

Briefly, microwave synthesis heats a sample via dielectric heating. For dielectric heating, the generated power per unit volume is given as:

$$Q = \omega \varepsilon_{\tau}'' \varepsilon_o E^2$$

where ω is the angular frequency of the excitation radiation, ε_{τ}'' is the imaginary part of the relative complex permittivity of the sample, ε_o is the permittivity of free space, and E is the electric field strength. Samples that are a mixture may have constituents, which will undergo greater dielectric heating compared to the other constituents causing non-homogeneous heat generation. The microwave interaction of an individual constituent of a mixture depends on the ε_{τ}'' of that constituent. Most solvents that are used in microwave synthesis are chosen because of their high ε_{τ}'', such as polyethylene glycol (200 molecular weight) with an ε_{τ}'' of ~6.5 (@2500 Mhz).[99] In comparison, $LiCoPO_4$ has an ε_{τ}'' of ~ 67 (@10 MHz).[100] Although we were unable to find the precise ε_{τ}'' for TEG and $LiCoPO_4$ at the microwave operating frequency of 2455 MHz, these values are illustrative of the order of magnitude higher value of ε_{τ}'' expected for many metal-oxides and metal phosphates when compared to polyglycol solvents. In this particular case, the microwave will locally heat the $LiCoPO_4$ nanoparticles to a higher temperature than the TEG or the bulk solution temperature, as shown in Figure 2a. The highest solution temperature will occur locally at the surface of the nanoparticles, causing the LFP precursors to preferentially nucleate on the surface of the existing LCVP nano-particles rather than in the bulk. This method of creating hierarchical nanoparticles by causing surface nucleation can be extended to any combination of solvents and particles as long as the $\varepsilon_{\tau,solvent}'' << \varepsilon_{\tau,particle}''$. This present study demonstrates the synthesis of ceramic-ceramic core-shell nano-particles, but this method could also be extended to synthesize ceramic-metal, metal-ceramic, and metal-metal, core-shell materials.

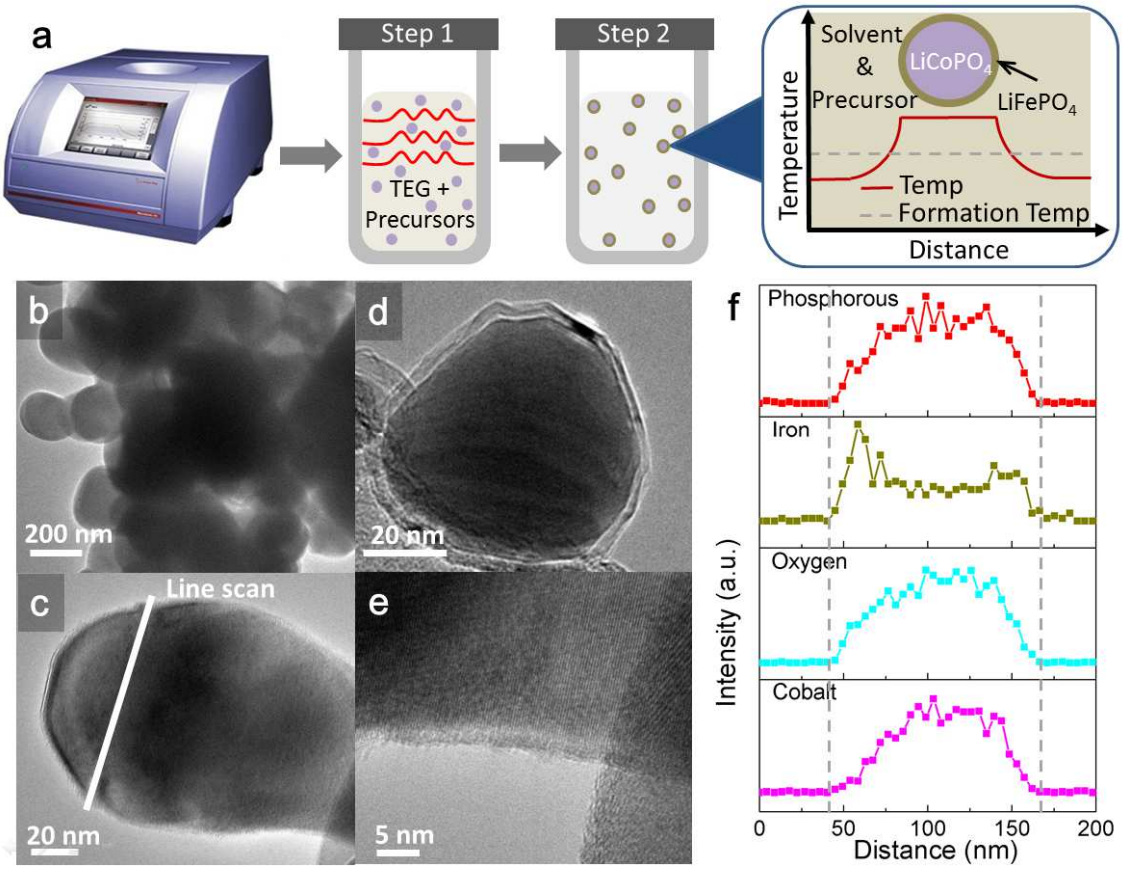

Figure 5.2. (a) Illustration of the MW-ST coating method as well as a graphic showing the expected local temperature distribution around a core LCVP nano-particle. TEM micrographs of (b) $LiCo_{1-3x/2}V_x\square_{x/2}PO_4$ (x = 0.04) showing the general particle morphology. TEM micrographs of LFP-coated $LiCo_{1-3x/2}V_x\square_{x/2}PO_4$ (x = 0) particles showing (c) where the EDS line-scan was performed, (d) the core-shell structure of a particle oriented parallel to the beam axis, and (e) the core-shell of a particle oriented perpendicular to the beam axis. f) Quantitative EDS data for the line-scan shown in Figure 2c.

5.6. Morphology

TEM micrographs (Figure 5.2b-f) show the morphology of the LFP-LCVP nanoparticles after the MW-ST coating. The nanoparticles have spherical or oblong spheroid morphologies with widths ranging from 50 to 250 nm (Figure 5.2b). The core-shell structure of the nanoparticles was most apparent for particles which have the long axis parallel to the beam axis, as shown in Figure 5.2d. The shell was also seen on perpendicularly oriented particles, such as in Figure 5.2e, although the contrast between

the core and shell is lower. The core-shell structure is composed of the core LCVP nano-particle with an LFP coating approximately 3 - 5 nm thick. The shell is monolithic rather than an agglomeration of smaller particles on the larger core particle. The monolithic nature of the coating is believed to be important in preventing electrolyte from penetrating the coating and decomposing on the LCVP particle surface during cycling. In addition to TEM, EDS line scans were performed on the LFP-LCVP particles to provide further verification of the core-shell structure. The particle shown in Figure 5.2c had a line-scan performed over the marked region. The quantitative results of the EDS line-scan are shown in Figure 5.2f. Careful examination of the line-scan results reveals two features, which support the formation of an LFP shell on an LCVP core. First, the width of the iron, phosphorous, and oxygen signals are wider than the cobalt signal. This indicates that iron, phosphorous, and cobalt span the full width of the particle, while cobalt is not present at the edges. Second, the shape of the iron signal is different than the phosphorous, oxygen, and cobalt signals. Phosphorous, cobalt, and oxygen have a concave down distribution, while the iron distribution is concave up. The iron distribution shows that iron is concentrated equally across the surface of the particle. The higher counts near the edge are due to the interaction of the beam with a larger LFP-rich volume as it passes through greater amounts of the coating at the particle edge. Unfortunately, EDS line-scans were not possible on the vanadium containing compounds because the LFP-coated $LiCo_{1-3x/2}V_x\square_{x/2}PO_4$ (x = 0.02, and 0.04) were not stable under the TEM electron beam. The LCVP instability is consistent with our previous work, which found that LCVP materials decompose at temperatures above 525 ^oC.[89]

In addition to TEM and EDS, XPS was performed to further validate the core-shell structure with the results presented in Figure 5.3a-d. There was some difficulty in performing quantitative analysis of the Fe : Co ratio owing to the overlap of the Fe LMM Auger peak with the photoelectron Co 2p peak, as well as overlap of the Co LMM Auger electron peak with the strongest iron photoelectron Fe 2p peak, shown in Figure 5.3b and Figure 5.3d respectively. Due to these spectral overlaps, a sample with 10% $LiFePO_4$ coating was used to provide a stronger iron signal relative to the Co LMM Auger peak. The overall intensity of the Co 2p peaks was significantly lower in the LCP-10% $LiFePO_4$ sample (Figure 5.3b) compared to the uncoated LCP material (Figure 5.3a),

while the intensity of the O1s and P 2p peaks of both samples were nearly identical, indicating shielding of the Co signal by Fe.

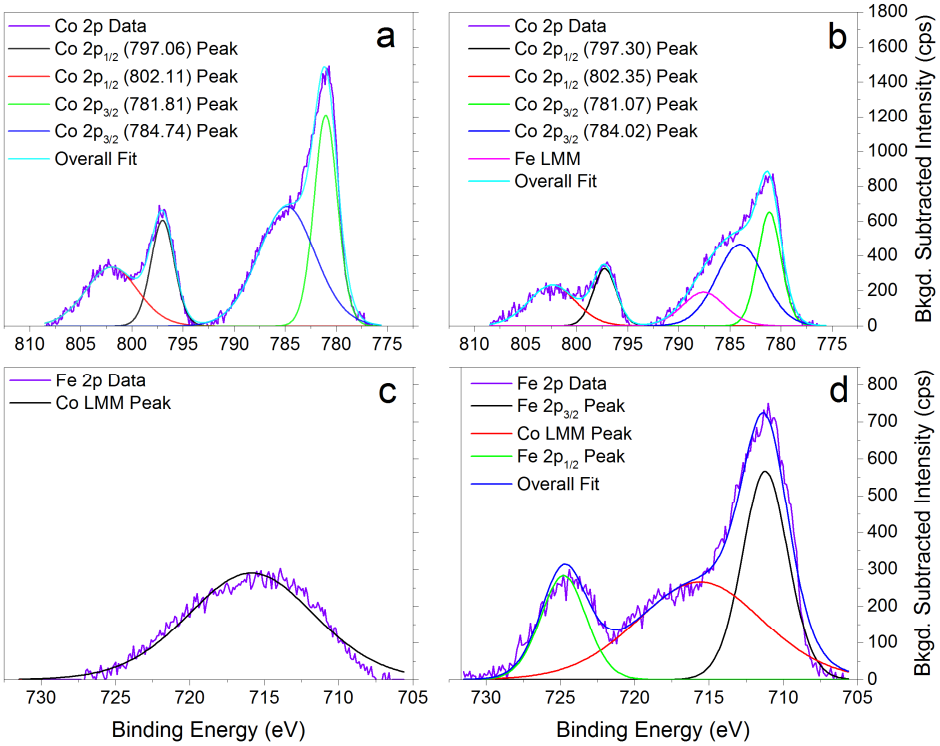

Figure 5.3. XPS spectra: (a) Co 2p peaks of uncoated $LiCoPO_4$, (b) Co 2p and Fe LMM peaks of $LiCoPO_4$-coated with 10% $LiFePO_4$, (c) Co LMM peak of uncoated $LiCoPO_4$, and (d) Fe 2p and Co LMM peaks of $LiCoPO_4$ coated with 10% $LiFePO_4$.

The ratio of the Co $2p_{3/2}$ peak to the Co $2p_{1/2}$ peak was greater than 2 for the $LiFePO_4$ coated material with the difference in area attributed to the Fe LMM Auger peak, Figure 5.3b. Quantitative analysis of Co, Fe, P, and O was performed using the integrated area of the Co $2p_{1/2}$, Fe 2p, P 2p, and O 1s peaks, with the results presented in Table 5.1.

Table 5.1. Atomic percent of elements in uncoated and 10% LFP coated $LiCoPO_4$ measured by XPS excluding lithium

Sample	XPS atomic percent			
	Co	Fe	P	O
$LiCoPO_4$	17.51	--	16.27	66.21
$LiCoPO_4$ + 10% $LiFePO_4$	7.35	8.55	15.71	68.40

It can be seen that although the nominal ratio of Fe : Co in the sample is 1 : 9 XPS determined the ratio to be 1.16 : 1. The overrepresentation of iron via XPS compared to the samples nominal stoichiometry is consistent with the iron being located at the surface of the particles. The diminished intensity of the Co 2p peaks, rather than complete suppression, is consistent with a monolithic (5-7 nm) $LiFePO_4$ shell when considering the 10 nm penetration depth of Al Kα radiation. Using a strictly volumetric argument, a 5-7 nm shell with a 10 nm penetration depth would be expected to produce measured Fe to Co ratios ranging from 1 : 1 to 1.4 : 1 which is in agreement with the quantitative result. Furthermore, it should be noted that the integrated area of the Fe 2p peaks is likely under represented due to the inability to fit the satellite peaks that are known to exist for $LiFePO_4$ on both the Fe $2p_{1/2}$ and Fe $2p_{3/2}$ peaks due to the presence of the Co LMM Auger peak. If the fitting of the satellite peaks was possible, the ratio of iron to cobalt would be even greater than the currently measured 1.16 : 1. The TEM, EDS, and XPS results provide a consistent and compelling evidence of the formation of a monolithic LFP coating on the LCVP particles via the MW-ST method.

5.7. Structure, composition, and electrochemical characterization

Powder x-ray diffraction patterns of all the LCVP samples were taken before and after coating with LFP and are presented in Figure 5.4a. The XRD patterns show that all of the samples are single-phase materials, with no impurity peaks. No new identifiable peaks were observed corresponding to the LFP phase after coating. The lack of new peaks is not surprising because the LFP has the same space group (*Pnma*) and similar lattice parameters as LCVP.

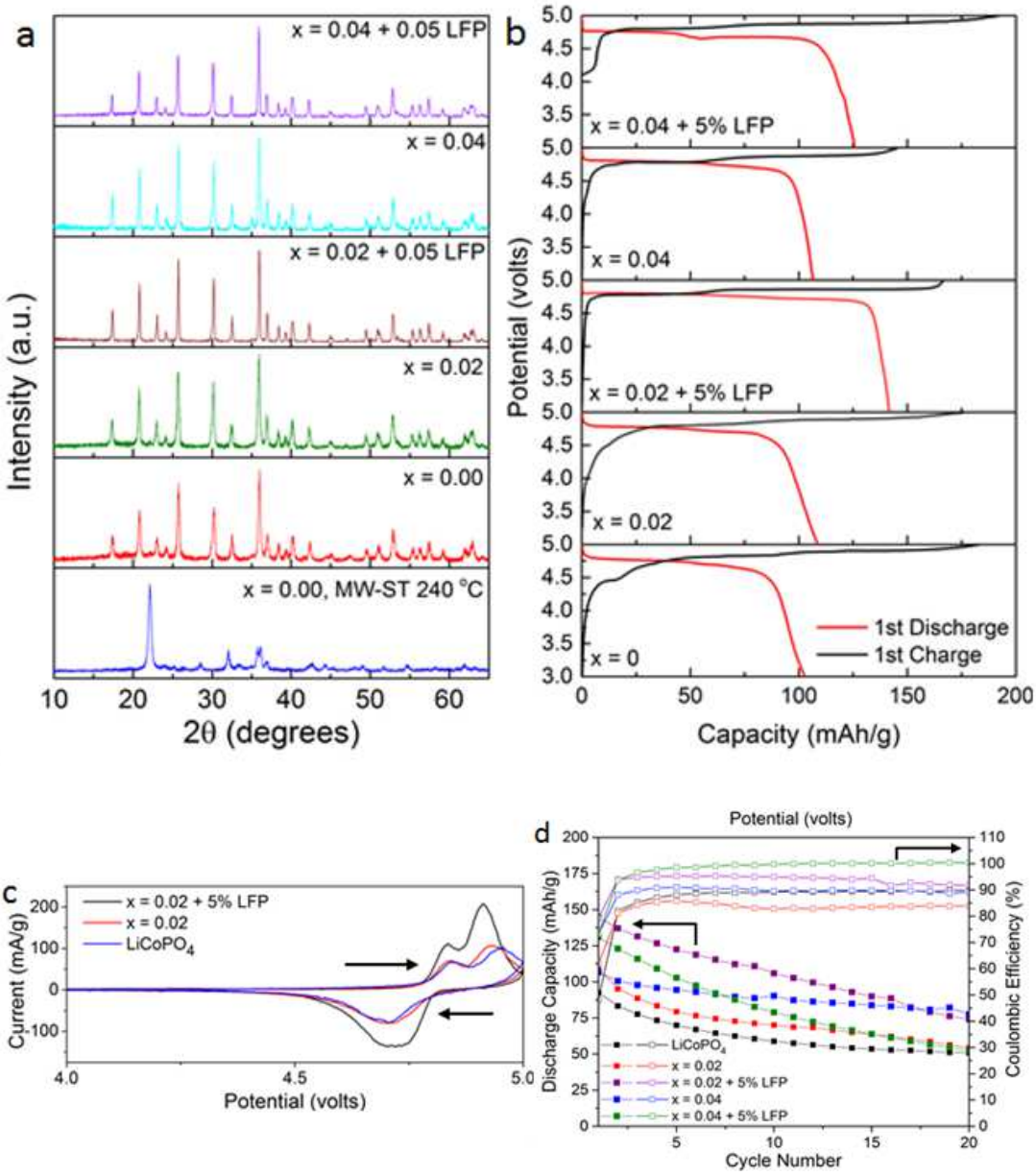

Figure 5.4. (a) Powder x-ray diffraction patterns of both the uncoated and LFP-coated $LiCo_{1-3x/2}V_x\square_{x/2}PO_4$ (*Pnma*) after post-heating at 525 ^oC and $LiCoPO_4$ (*Pn2₁a*) prior to post heating. (b) First cycle charge/discharge voltage profiles of both the uncoated and LFP-coated $LiCo_{1-3x/2}V_x\square_{x/2}PO_4$. (c) Cyclic voltammograms of $LiCoPO_4$, LCVP, and LFP-LCVP. (d) Discharge capacity and the coulombic efficiencies of both the uncoated and LFP-coated and $LiCo_{1-3x/2}V_x\square_{x/2}PO_4$ cycled from 3 to 5 V at a rate of 0.1C.

The precise stoichiometries of the LCVP samples were assessed with ICP-OES both before and after coating with LFP and are presented in Table 5.2. The nominal stoichiometries closely match the measured values. Furthermore, the measured stoichiometries show that a coating of approximately ~ 4.3 at. % was achieved via the MW-ST method for the LCVP samples with x = 0.02 and 0.04.

Table 5.2. Chemical compositions of the uncoated and LFP coated $LiCo_{1-3x/2}V_x\square_{x/2}PO_4$ measured by ICP-OES

Sample	ICP stoichiometry			
	Li/P	Co/P	V/P	Fe/P
$LiCoPO_4$	0.98	0.97	--	--
$LiCo_{0.97}V_{0.02}\square_{0.01}PO_4$	0.98	0.99	0.02	--
$LiCo_{0.97}V_{0.02}\square_{0.01}PO_4$ + 5% $LiFePO_4$	0.95	0.93	0.02	0.04
$LiCo_{0.94}V_{0.04}\square_{0.02}PO_4$	0.95	0.94	0.04	--
$LiCo_{0.94}V_{0.04}\square_{0.02}PO_4$ + 5% $LiFePO_4$	0.91	0.89	0.04	0.04
All samples have an estimated error of < 2%				

Galvanostatic charge/discharge tests were performed on the cells made with both the LCVP and the LFP-LCVP samples. The cells were cycled over a 3 to 5 volt potential range at a rate of C/10. The first charge/discharge cycles are shown in Figure 4b. The baseline $LiCoPO_4$ material had a first discharge capacity of 103 mAh/g, while the capacity improved slightly for the LCVP materials with x = 0.02 and 0.04 to, respectively, 109 mAh/g and 107 mAh/g. The LFP-coated LCVP samples experienced the greatest improvement in the first-cycle discharge capacity with 145 and 127 mAh/g for, respectively, the x = 0.02 and 0.04 samples. The discharge capacity of the LFP-coated LCVP sample with x = 0.02 had one of the highest first-cycle discharge capacities for $LiCoPO_4$ reported to date in the literature and represents 87% of the theoretical capacity of 167 mAh/g. A flattening of the charge/discharge curves was observed for the LFP coated samples. The flattening may be due to the reduction of side reaction with the electrolyte during first cycle, preventing the formation of lower conductivity SEI layers.

The formation of significant SEI layers would create a sloping in what should otherwise be a nearly constant electrochemical potential of the two 2-phase regions.

In addition to galvanostatic testing, cyclic voltammetry was performed on the LCVP samples (Figure 5.4c). The cyclic voltammograms show a change in the activity and polarization of the LCVP materials due to both vanadium substitution as well as coating with LFP. The rightmost redox peak is shifted to lower potentials from 4.952 V for the $LiCoPO_4$, to 4.930 and 4.912 V, respectively, for the $LiCo_{0.97}V_{0.02}\square_{0.01}PO_4$, and $LiCo_{0.97}V_{0.02}\square_{0.01}PO_4$ + 5% $LiFePO_4$ samples. This is a 40 mV shift down in the potential at the redox peak. The lower potential redox peak allows the upper potential limit for the charge cycle to be lowered for the LFP-LCVP samples to 4.93 V with no appreciable (< 1 %) decrease in the discharge capacities.

The discharge capacities as well as the coulombic efficiencies during galvanostatic testing are shown in Figure 5.4d. The LFP-LCVP sample with x = 0.02, which had the highest initial capacity, show a 51% retention of the initial discharge capacity. The LFP-LCVP sample with x = 0.04 also exhibit a capacity retention of 51%. The rather rapid decrease in the capacity of the $LiCoPO_4$ samples is characteristic of most reports. Most recently, there have been reports that the substitution of iron, chromium, and silicon led to better long-term cyclability, but the coulombic efficiency remained under 99.5%.[88] This indicates that substitution in the $LiCoPO_4$ increased the stability of the bulk material during cycling, but did not fully mitigate electrolyte side reactions. The bulk instability during delithiation of $LiCoPO_4$ causes the irreversible formation of CoP_2O_7.[101] The LFP coated samples have a lower polarization and higher initial capacity, which means more lithium was removed during charging which would lead to the formation of more CoP_2O_7 compared to the uncoated samples, explaining the more rapid rate of capacity fade in the coated samples. Interestingly, we found a repeatable and systematic increase in the coulombic efficiency of the samples with LFP coating. Specifically, the coulombic efficiency of the LCVP sample with x = 0.02 increased from ~ 85% to ~ 95% with the addition of the LFP coating. A similar increase of ~ 10% in coulombic efficiency was also observed for the LFP-LCVP sample with x = 0.04, which brought the coulombic efficiency to 100.00%.

5.8. Conclusion

In summary, a novel method of microwave-assisted solvothermal synthesis of core-shell nanoparticles has been demonstrated by coating $LiFePO_4$ on $LiCo_{1-3x/2}V_x\square_{x/2}PO_4$ (x = 0.02 and 0.04). The MW-ST coated materials were characterized with TEM, EDS and XPS, which showed compelling evidence of the formation of a monolithic LFP layer on the LCVP samples. The electrochemical properties of the LFP-LCVP samples were assessed and compared to that of uncoated LCVP materials as well as $LiCoPO_4$. The LFP-LCVP samples showed reduced polarization and lower required charging potentials. The LFP-LCVP sample with x = 0.02 had one of the highest reported first cycle discharge capacities of 145 mAh/g. The coulombic efficiency of the LFP-LCVP samples increased by approximately 10% compared to the corresponding uncoated LCVP samples. The LFP-LCVP sample with x = 0.04 had a coulombic efficiency of 100.00%, which indicated that the LFP coating mitigated the electrolyte side reactions. Further work could be carried out to investigate the effect of MW-ST synthesis of core-shell particles with other cathode materials, which have better bulk stability than $LiCoPO_4$, yet still suffer from capacity fade due to irreversible electrolyte side reactions.

Chapter 6: Metal Nanofoams via a Facile Microwave-assisted Solvothermal Process[4]

6.1. Abstract

A novel, facile, non-hazardous, low temperature/pressure microwave solvothermal method of producing pure copper, silver, and nickel metal nanofoams is presented. The nanofoams have been produced using inexpensive metal acetates and polyglycol solvent. The nanofoam formation proceeds in two steps within a single-pot synthesis: formation of metal nanoparticles, followed by the sintering of nanoparticles into nanofoams. The nanofoams have many potential uses in clean energy applications, particularly lithium-ion batteries.

6.2. Introduction

Free-standing cotton like metal nanofoams, specifically copper, silver, and nickel, have been synthesized via a facile, one-step microwave-assisted solvothermal (MW-ST) method. The metal nanofoams hold great potential for use as substrates for battery and supercapacitor electrodes as well as catalysts.[102–111] More specifically, there have been a number of efforts to create high power, fast charging batteries by employing 3D electrode architectures, particularly with lithium-ion batteries.[102,103,106,107,112] These efforts have shown the promise of high surface area metal substrates, but unfortunately have had to use very tedious, multi-step, synthesis methods. Additionally, there have been several efforts which have sought to make all-solid state lithium-ion batteries (LIBs) by employing electrodeposition of active materials on to conducting substrates, such as traditional micrometer sized metal foams and metal nano-wires.[105,113–115] All of these efforts have demonstrated the need for a facile synthesis method of making high surface

[4] This chapter is based on previously published work: K. Kreder, A. Manthiram, "Metal nanofoams via a facile microwave-assisted solvothermal process," *Chemical Communications*, 53, 865-868 (2017).

area metal substrates. Due to these promising applications, a large amount of research has been focused on several different synthesis approaches.[116–120] The currently known methods of producing high surface area metal foams include templating, dealloying, nanosmelting, and combustion synthesis methods. All the current methods have a limitation that would hinder scale-up for most applications.

Specifically, the templating methods all require the preparation of a nanoscale template, usually a pearlite structure, which takes a non-trivial amount of time to prepare. There are usually at least three subsequent steps, depending on the specific method, to produce the nanofoam.[120,121] Dealloying methods are limited to producing more expensive noble metal frameworks, such as silver and gold.[122,123] The nanosmelting method is very simple, but does not create macroporous materials, nor are these materials phase-pure metals.[124] The combustion synthesis method appears to be the most scalable, but requires a multi-step synthetic route using hazardous azide chemistry to produce the precursor. Furthermore, most of the precursors that are used in this process were originally investigated for use as contact explosives.[125–127] Finally, the precursors must be combusted in an inert atmosphere at high pressures (300 – 1000 psi), generating highly toxic gas by-products.[118] There have also been prior reports on self-assembled Ni/Au/Pt/Pd nanochains via room-temperature chemical methods, but the size scale (< 20 nm) is much smaller, making them structurally inadequate in most applications.[128–130] We present here a novel, single-step, microwave-assisted solvothermal (MW-ST) method that uses inexpensive, non-hazardous, widely available polyglycol solvent and the corresponding metal salts, while still producing robust high surface area metal nanofoams. Additionally, the MW-ST method is the simplest known process, which could potentially be developed at scale to produce uniform metallic foams with controlled dimensions.

6.3. Results and Discussion

Accordingly, metal nanofoams of copper, silver, and nickel were synthesized via a low-temperature, low-pressure, MW-ST method, using the corresponding metal acetate as the precursor and tetraethylene glycol as the solvent. The precursors were rapidly heated in an Anton-Parr Monowave microwave reactor to 300 ^{o}C. The total time to

produce all of the nanofoams from the start of the reaction to completion was less than 3 minutes.

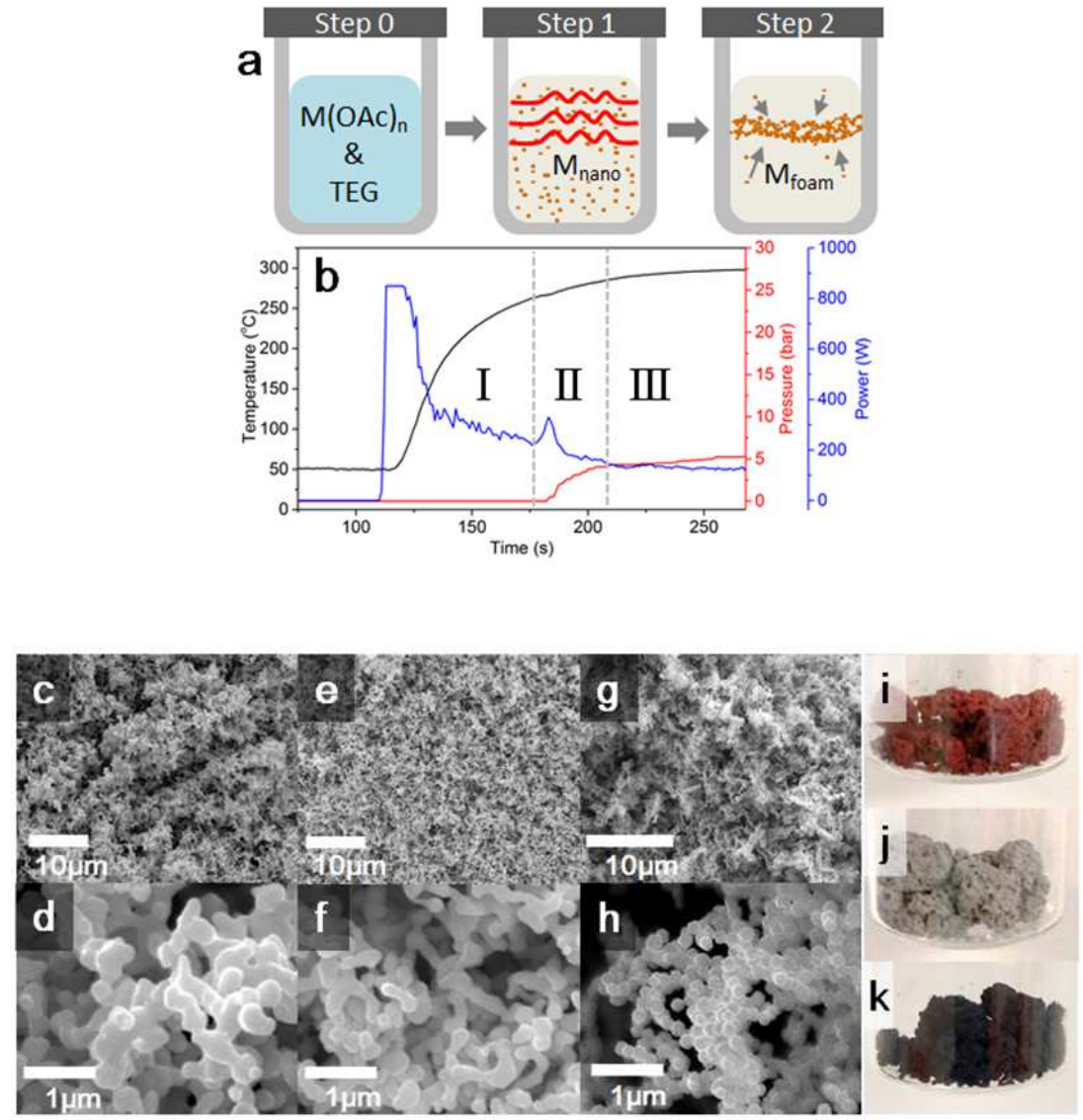

Figure 6.1. (a) Illustrative process of the synthesis procedure of the metal nanofoams, showing the separate steps of nanoparticle nucleation and subsequent sintering to form the nanofoam. (b) Pressure, temperature, and power versus time of the Anton-Paar microwave reactor during the synthesis of nickel metal nanofoam. Low and high magnification SEM micrographs of the MW-ST produced (c,d) copper, (e,f) silver, and (g,h) nickel nanofoams. Color photographs of (i) copper, (j) silver, and (k) nickel nanofoam

The nanofoam formation appeared to occur with two distinct steps within the single-pot synthesis process, as shown in Figure 6.1a. The first step is the well-known reduction of the metal acetate to metal by the TEG, which produces metal nanoparticles.[131] The nanoparticles subsequently undergo growth as the acetate precursors are expended. As the temperature is increased further, a rapid second step takes place, where the metal nanoparticles agglomerate and fuse into a metal nanofoam. The transition between the first step of forming nanoparticles and the second step of creating nanofoam can be observed in the pressure and power of the microwave reactor, as shown in Figure 6.1b. Specifically, for the nickel nanofoam, the microwave reactor was at 0 bar relative pressure until approximately 175 s into the reaction, at which point there was an ~ 150 W spike in the power, required to maintain the heating, as well as an ~ 4 bar increase in pressure. The pressure and power of the microwave reactor for the silver and copper nanofoams are shown in Figure 6.2 and Figure 6.3, respectively.

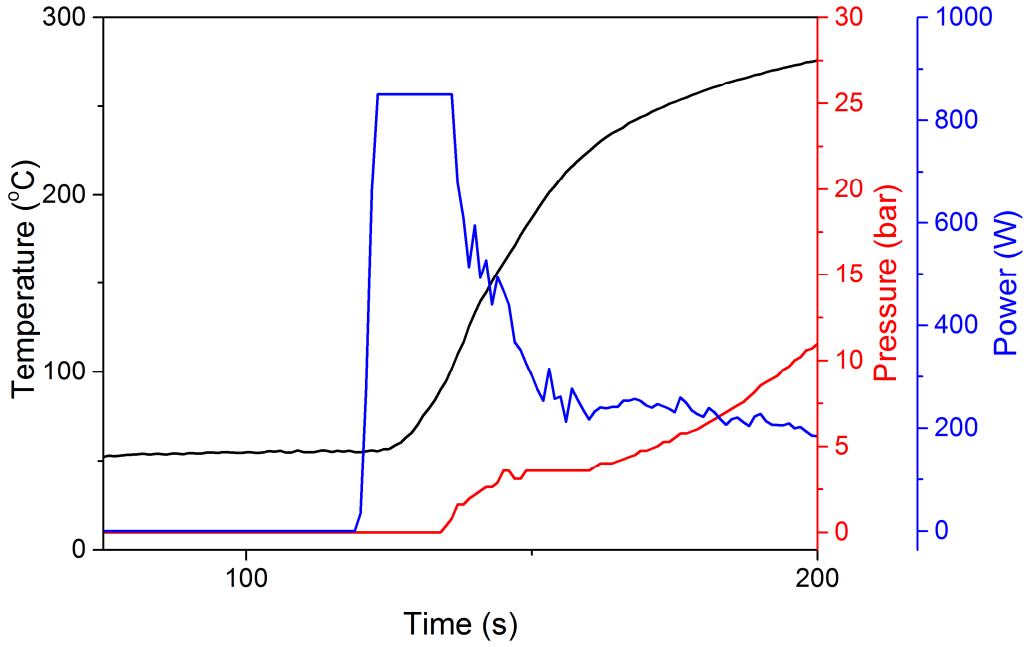

Figure 6.2. Pressure, temperature, and power versus time of the Anton-Paar microwave reactor during the synthesis of silver metal nanofoam.

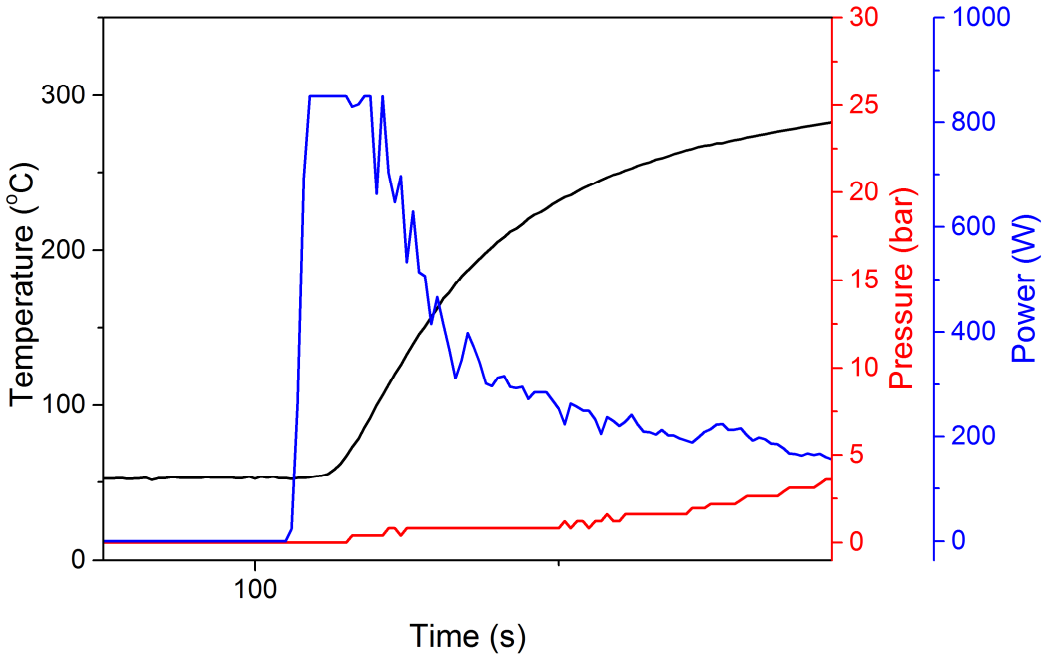

Figure 6.3. Pressure, temperature, and power versus time of the Anton-Paar microwave reactor during the synthesis of copper metal nanofoam.

Due to the speed at which the formation of the nanofoam occurs, there appears to be a force that drives the agglomeration of the nanoparticles. It is hypothesized that as the nanoparticles increase in size, they begin to interact with the microwave field which causes the circulation of current within the particles. The circulating currents induce a magnetic field, which causes the rapid agglomeration. As the particles collide, the induced currents pass across adjacent particles fusing them together. Only nanoparticles were observed to have formed when the reaction was stopped prior to the power/pressure spike, whereas nanofoams were produced when the reaction was stopped subsequent to the spike. The dependence of the formation of nanoparticles or nanofoams on when the reaction was stopped, relative to the spike, supports the hypothesis of a two-step nanofoam formation.

Scanning electron microscopy (SEM) images as well as photographs of the synthesized nanofoams are presented in Figure 6.1c-h. The SEM images reveal that the nickel nanofoam had the finest structure with the structural members composed of spheres having a diameter of less than 100 nm. The silver nanofoam

had the next finest structure with the structural members having 150-300 nm widths. The copper nanofoam had the coarsest structure with the structural members having 200-400 nm widths. Unlike the nickel, the copper and silver base particles did not have a well-defined shape. Consequently, the mechanical robustness of the foams appears to be inversely correlated to the size of the structure, with the copper foam being the most robust and the nickel foam being the most fragile. Additionally, all of the foams appeared to be made from the joining/welding of smaller particles into a network. The copper and silver foams were robustly joined with joints ~ 80 % of the width of the structural members. The nickel foam appeared to be less well joined, with joints ~ 50 % the width of the structural members. The difference in the degree to which the metal nano-particles were joined could be due to the relative melting points of the metals, *viz.*, 1085, 962, and 1455 ^{o}C, respectively, for copper, silver, and nickel. The melting points indicate copper and silver could be more easily joined than nickel at low temperatures, agreeing with the experimental observations. The colours of the foams, shown in Figure 6.1i-k, were reddish-brown, grayish-white, and black, respectively, for copper, silver, and nickel. The colourings indicate metallic materials coated by a thin layer of the naturally occurring metal oxide. The effect of precursor concentration on the size and structure of the copper nanofoam was explored, and the SEM micrographs are presented in Figure 6.4.

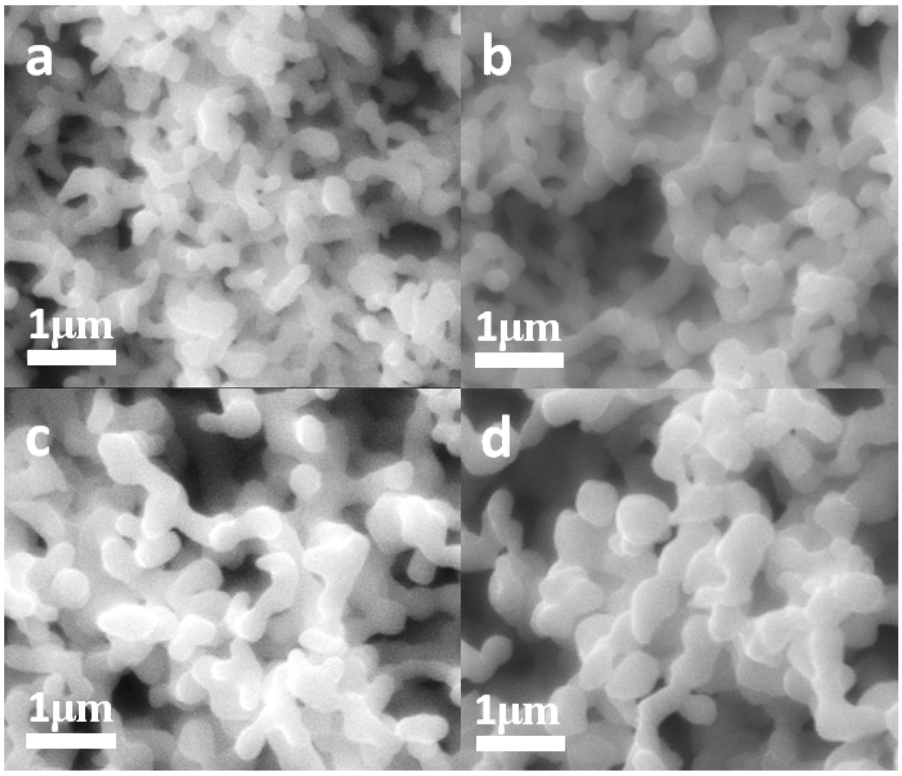

Figure 6.4. SEM micrographs of the copper foams formed from different concentrations of copper acetate: (a) 0.01 M, (b) 0.02 M, (c) 0.04 M, and (d) 0.06 M.

The structure of the copper nanofoam became finer as the concentration of Cu-acetate decreased. The formation of the nanofoam over a concentration range of 0.01 – 0.08 M indicates that the reaction is not very sensitive to precursor concentration.

The composition, crystal structure, and crystallite size of the metal nanofoams were assessed with x-ray diffraction along with subsequent Rietveld refinement. The XRD patterns shown in Figure 6.5 indicate that all of the metal nanofoams are pure metallic phases. The XRD pattern of nickel shows that the nickel nanofoam is composed of a major FCC nickel phase and minor HCP nickel phase belonging to the *Fm-3m* and $P6_3/mmc$ space groups respectively. HCP nickel is typically a high pressure phase, but has also been known to form when nickel nanoparticles are made at low temperatures.[132]

both the silver and copper nanofoams are pure FCC metals with no impurities. The metal oxide which visually appeared to form on the surface is a small constituent because it did not appear in any of the XRD patterns. Further analysis of the nanofoams composition was carried out via high-resolution transmission electron microscopy (HRTEM), with the micrographs presented in Figure 6.6 and Figure 6.7 and Figure 6.8.

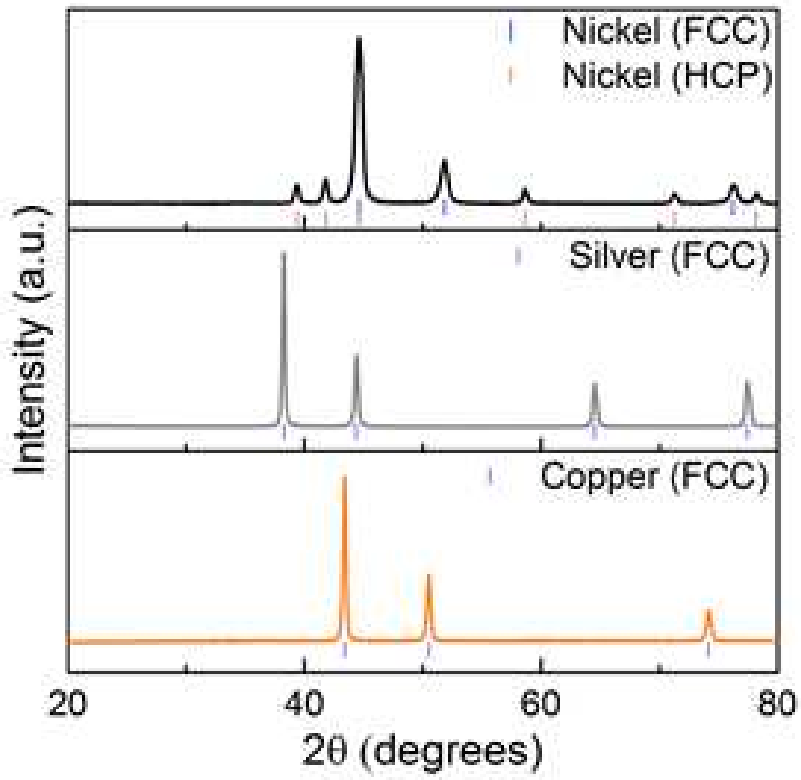

Figure 6.5. X-ray diffraction patterns of the MW-ST nickel, silver, and copper nanofoams.

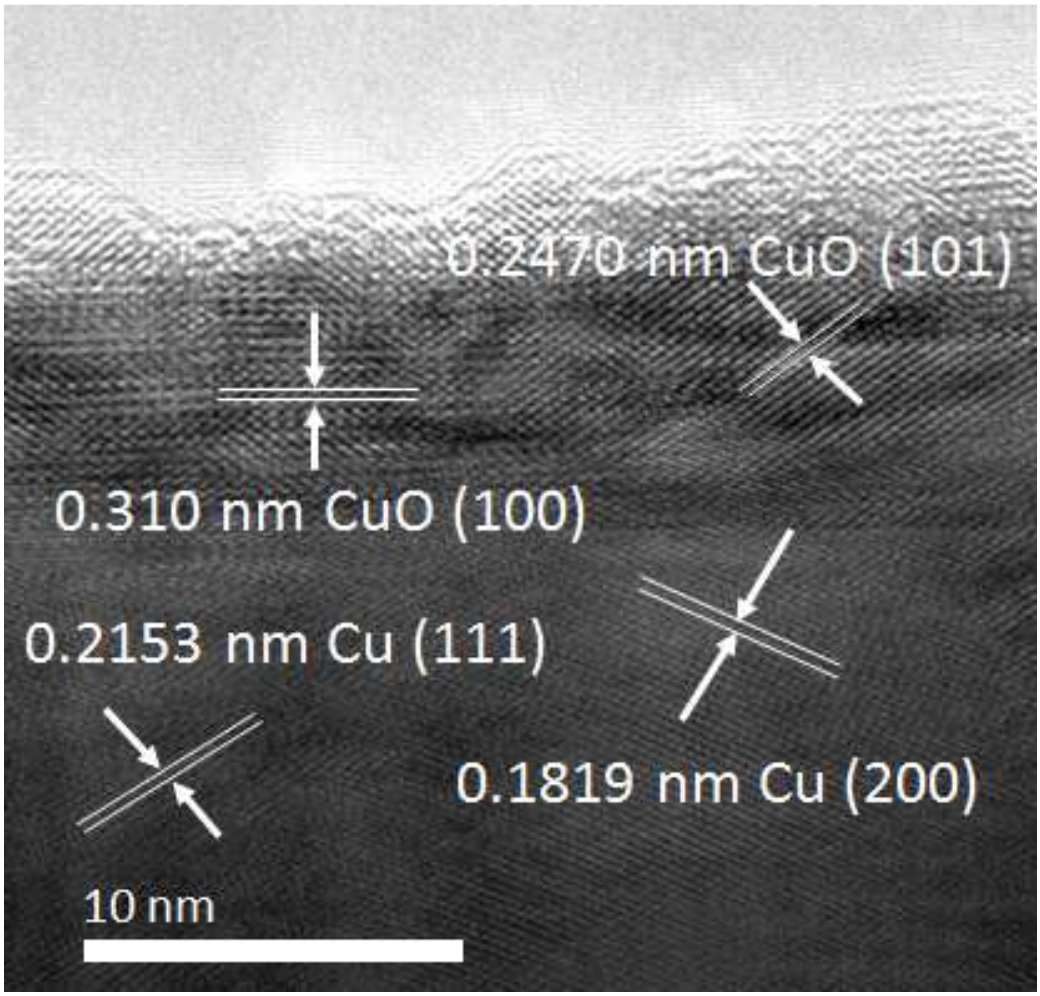

Figure 6.6. TEM micrograph of the copper foam with interplanar spacing in the bulk corresponding to the Cu (111) and (200) planes and at the surface corresponding to the CuO (100) and (100) planes.

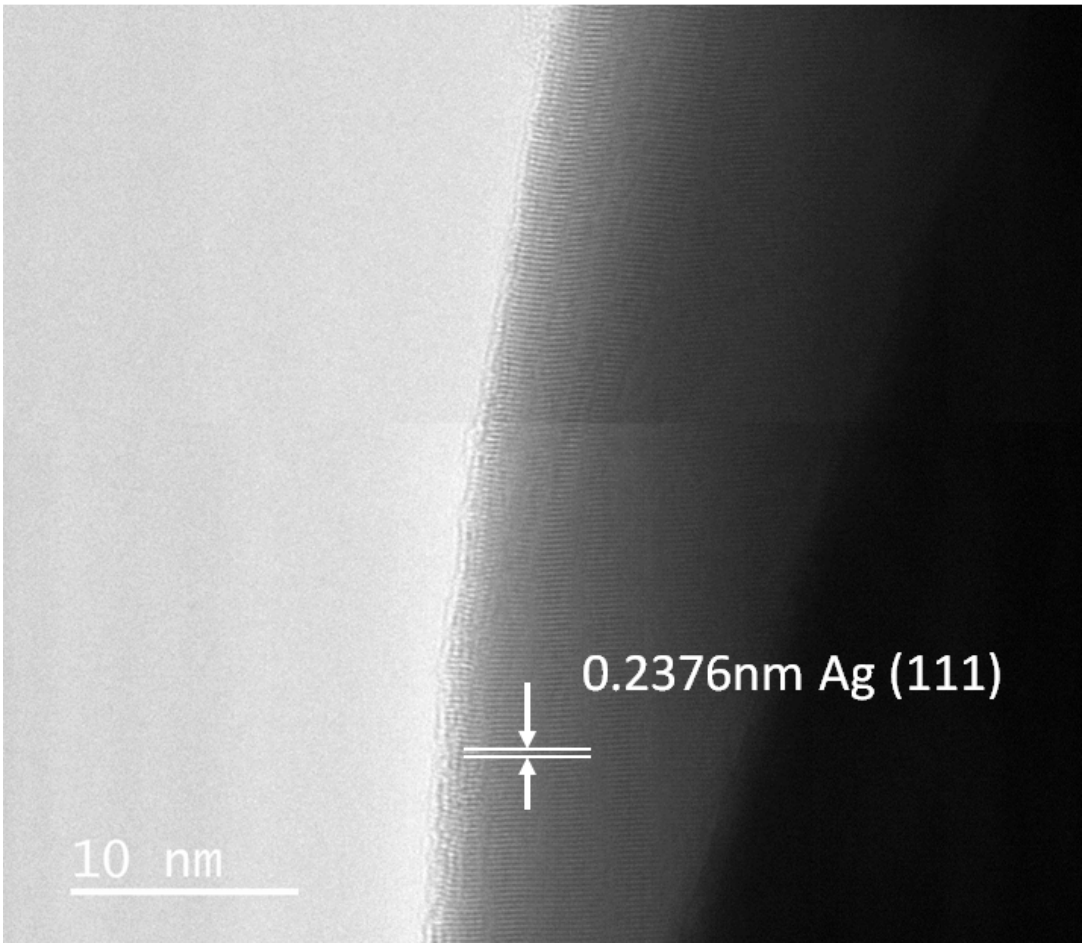

Figure 6.7. TEM micrograph of the silver foam with interplanar spacing corresponding to the (111) plane.

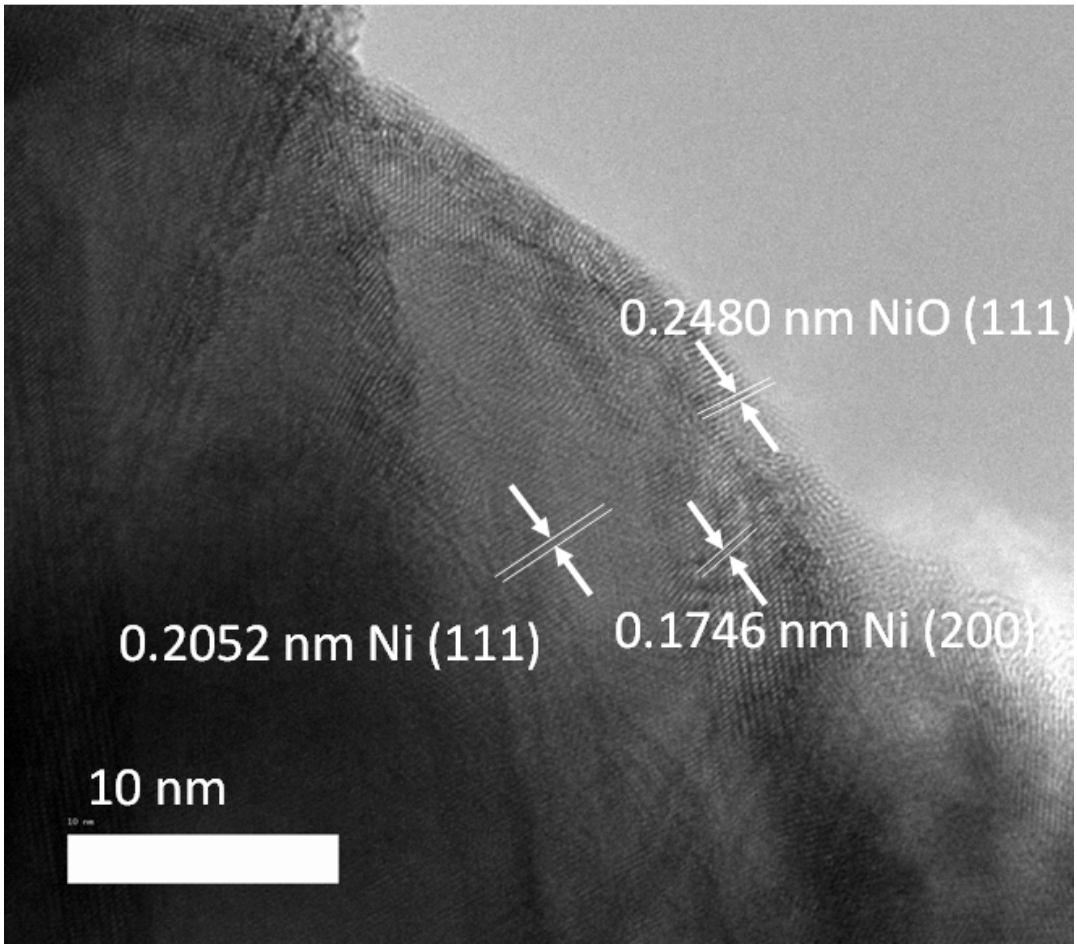

Figure 6.8. TEM micrograph of the of nickel foam with the interplanar spacings in the bulk corresponding to the Ni (111) and (200) planes and at the surface corresponding to the NiO (111) planes. The micrograph shows that the particle is mostly metallic Ni with a 1 – 3 nm thick layer of NiO on the surface.

The micrographs show that both the copper and nickel foams form metal oxide layers on their surfaces of 5 – 8 nm and 1 - 3 nm, respectively, while the silver did not have any appreciable metal oxide layer. The composition of the bulk particles was verified by measuring the interplanar spacing of the particles, while the composition of the surface layers was determined to be CuO and NiO, respectively, for copper and nickel.

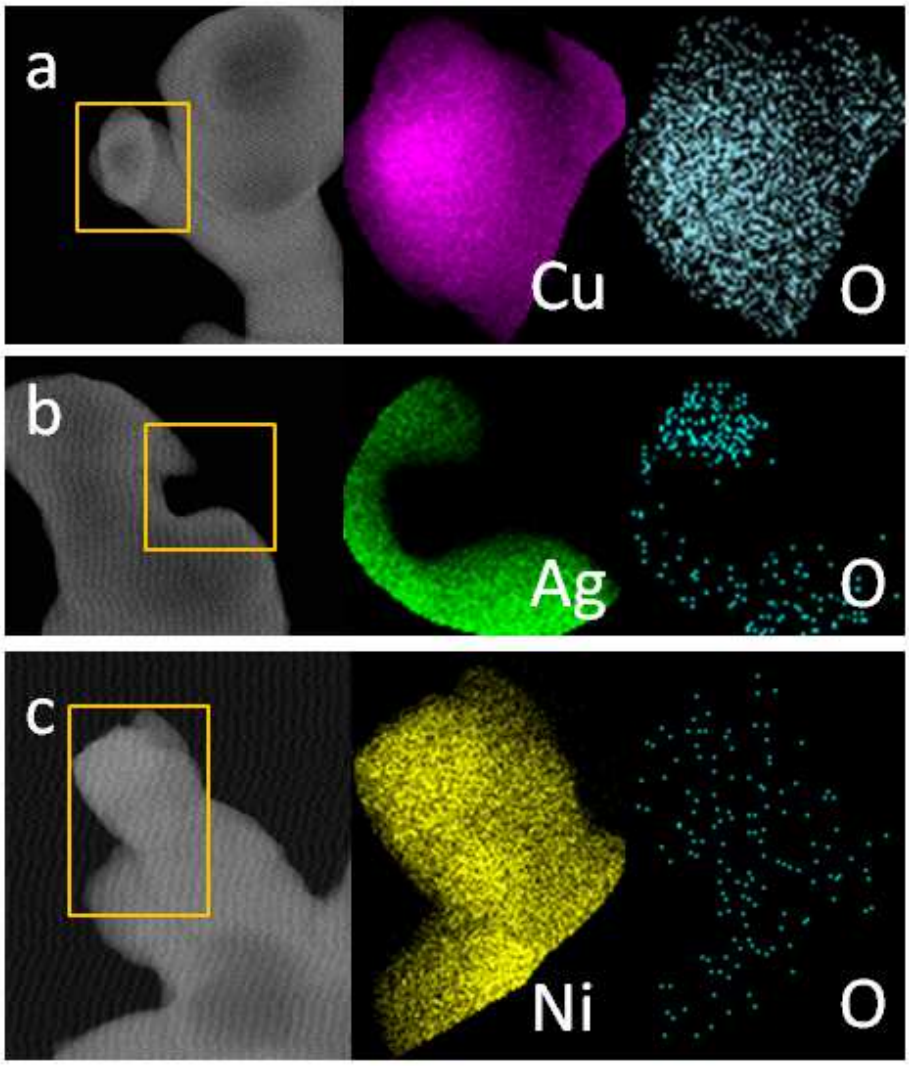

Figure 6.9. STEM micrographs and EDS maps of the (a) copper, (b) silver, and (c) nickel nanofoams.

The crystallite sizes of the metal nanofoams were determined with the Williamson-Hall method in conjunction with PDXL 2 software's Rietveld refinement feature. The nanofoams crystallite sizes were found to be 29 nm, 27 nm, and 13 nm, respectively, for the silver, copper, and nickel. It is interesting to note, that the crystallite sizes do not directly correlate with the foam structure sizes, but rather have an inverse correlation with melting temperature. Furthermore, based on the

crystallite analysis coupled with the TEM micrographs, it was deduced that the base nanoparticles from which the foam was composed had multiple crystallites.

The surface area of the foams, shown in Figure 6.10, were measured with the Brunauer, Emmett, and Teller (BET) analyser.

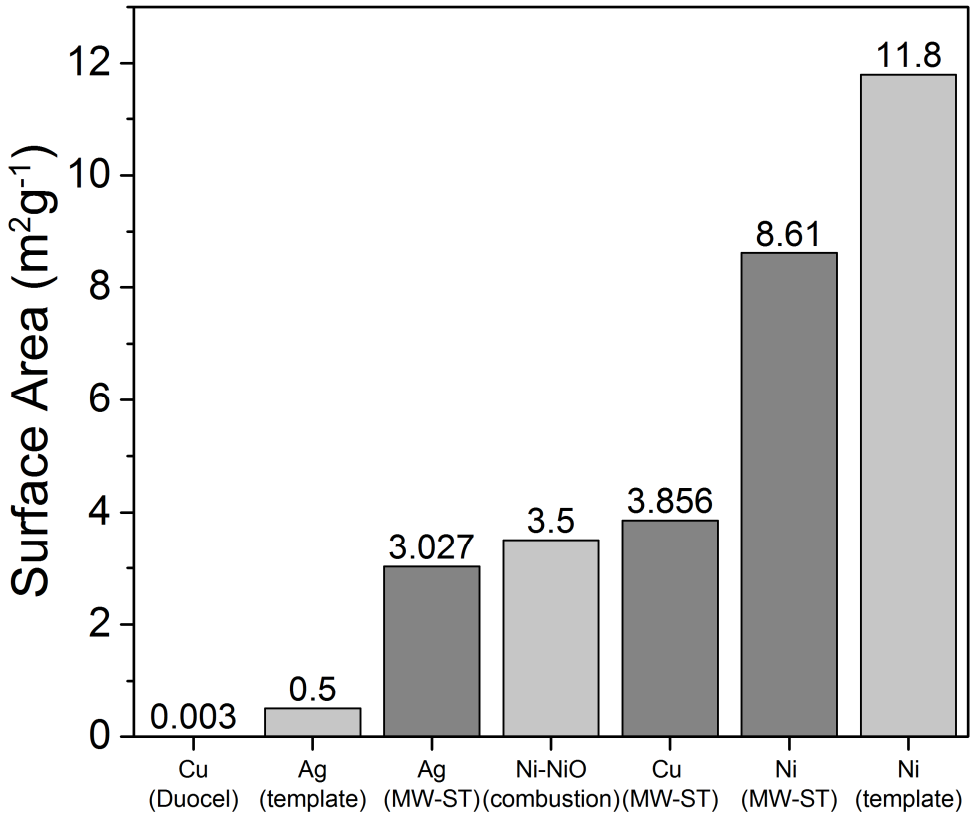

Figure 6.10. BET surface area of the MW-ST copper, silver, and nickel nanofoams compared to those of commercial copper foam[133], silver (templated) foam[119], nickel-nickel-oxide (combustion) foam[134], and nickel (templated) foam.[120]

The nickel foam had the highest surface area of the three nanofoams, followed by copper and silver, with surface areas of, respectively, 8.6, 3.9, and 3.0 m^2g^{-1}. The foams were found to have both mesoporosity and macroporosity, but were not found to be microporous. The surface areas of the metal nanofoams were compared with the previously reported non-microporous metal foams. The metal nanofoams presented here had a surface area that is three orders of magnitude

greater than that of the commercially available copper foam.[133] Additionally, they also had a higher surface area when compared to those produced with a nanosmelting technique (0.5 m^2g^{-1}) or a combustion technique (3.5 m^2g^{-1}).[119,134] The nickel nanofoam presented here had a slightly lower surface area when compared to a templated inverse pearlite structured nickel foam with a surface area of 11.8 m^2g^{-1}.[120] Overall, the nanofoams produced with the MW-ST method had surface areas comparable to or higher than those of the previously reported metallic foams, but were produced with a much simpler, faster, low-cost synthesis process.

The effects of further microwave heating and of post heating of the metal nanofoams were investigated. Specifically, after the formation of the metal nanofoams, the microwave reaction was continued for varying amounts of time. The SEM results of 5 min of post formation heating of the nickel nanofoam are presented in Figure 6.11.

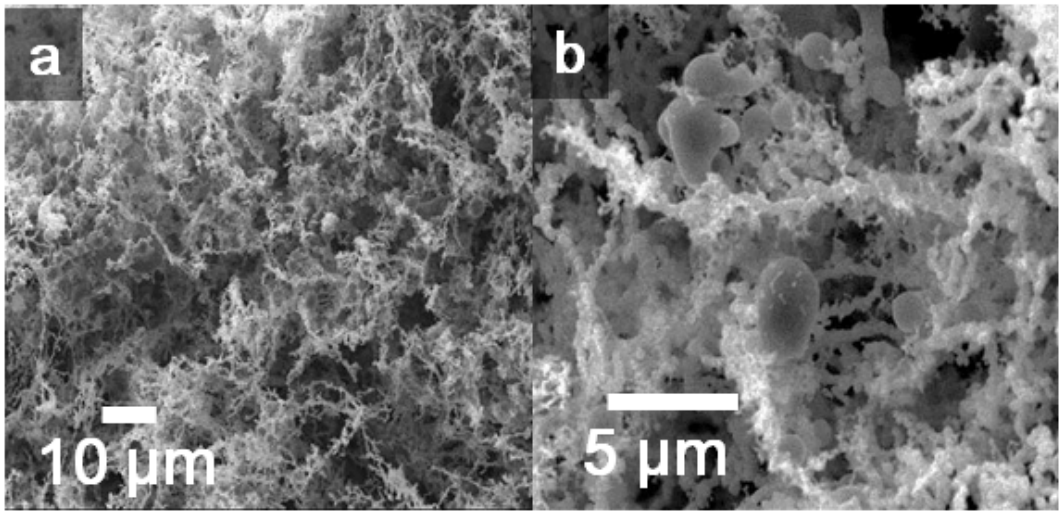

Figure 6.11. SEM micrographs of the nickel foam after 5 min of additional microwave heating shown at (a) low magnification and (b) high magnification.

Two phenomena were observed with a continued heating of the nickel. First, the nickel structure thickened, which is likely due to the flow of nickel metal. Second,

some of the flowing metal agglomerated into large sphere-shaped nickel deposits within the foam structure, shown in Figure 6.11b. Both of these phenomena were apparent in the SEM micrographs of the metal foams after continued microwave heating with a duration as low as 2 min. This experiment provides further evidence that the metal foams were not directly formed from the reduction of metal salts by the TEG, but are reaching a high enough temperature (>> 300 ^{o}C) in localized regions to flow and sinter together. Post heating of the metal nanofoam in an argon atmosphere was also investigated. The various samples were heated to 450, 500, 550, and 600 ^{o}C for 4 h. No noticeable changes in the structure of the nanofoams were observed prior to 550 ^{o}C. At 550 ^{o}C the copper nanofoam thickened slightly, but no noticeable change in overall volume was observed. The silver nanofoam thickened more than copper, and the volume decreased by an estimated ~20%. There were no noticeable changes in the appearance of the nickel nanofoam. When heated to 600 ^{o}C, all of the foams underwent a dramatic thickening of the structural members. The silver and copper nanofoams experienced a large reduction (> 50%) in their overall volume. The micrographs of the nanofoams after post heating are shown in Figure 6.12.

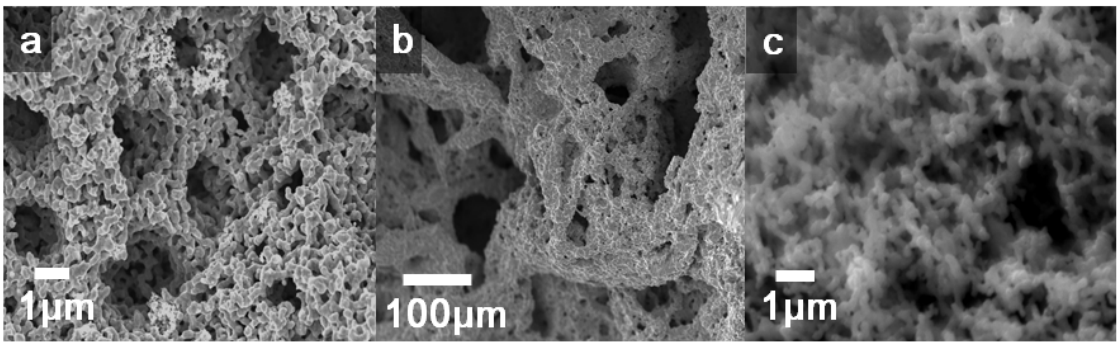

Figure 6.12. SEM micrographs of the (a) copper, (b) silver, and (c) nickel nanofoams after post heating in an argon atmosphere at 600 ^{o}C for 4 h.

Interestingly, unlike the continued microwave heating of the nanofoams, where large metal agglomerations were observed, the evolution of the nanofoams with post heating seemed to be self-similar. More specifically, the structural members

of the foams thickened while the pores of the foams remained. This behaviour could enable the production of self-similar sets of metallic foams on multiple size scales by controlling the time and temperature of the post heat treatment.

6.4. Conclusion

In summary, we have demonstrated a novel, simple, non-hazardous, fast, low temperature/pressure MW-ST method for producing copper, silver, and nickel metal nanofoams. The nanofoams were produced using inexpensive metal acetates and polyglycol solvent. The nanofoam formation took place in two steps within the single-pot synthesis process. Nanoparticles were formed first, which subsequently underwent sintering to form nanofoams. The local temperatures that were achieved in the microwave reactor appeared to exceed the bulk solution temperature. The post heating of the nanofoams caused self-similar foams to form in larger sizes. The surface areas of the nanofoams were higher than or comparable to those of the non-microporous metal foams produced using more complex methods. This simple, inexpensive method of producing metal nanofoams could be scalable and has potential uses in many clean energy applications. Future synthesis work on metal nanofoams could focus on further optimizing the heating rates, concentration of pre-cursors, as well as solvents to modulate the porosity and size of the nanofoams. Additionally, the synthesis of both composite and alloy nanofoams could be explored.

6.5. Experimental Section

6.5.1. Synthesis of Metal Nanofoams

The metal nanofoams of copper, silver ,and nickel were produced by dissolving 200 mg of copper(II) acetate monohydrate (Alfa-Aesar), silver-acetate (Fischer Scientific, laboratory grade), or nickel(II) acetate tetrahydrate (Arcos Organics, 99+%) in 12 mL of dry tetraethylene glycol (TEG) (Sigma-Aldrich 99%). The TEG was dried by storing on 4A molecular sieves (Fisher Scientific) prior to use. Dissolution of the salts was

expedited with approximately 10 min of ultra-sonication creating translucent blue, green, and clear solutions, respectively, for copper, nickel, and silver. The solutions were subsequently transferred to 20 mL borosilicate vessels and heated as fast as possible with a max power of 850 W to 300 ^{o}C in an Anton-Paar Monowave microwave reactor. The solutions were not stirred. Stirring of the solutions would cause the foams to become compacted into a ball of metal. The reactions were stopped approximately 1 min after the observation of the pressure spike. The samples were than washed three times with acetone and dried in an air oven at 100 ^{o}C.

6.5.2. Characterization of Metal Nanofoams

X-ray diffraction patterns were collected in continuous mode over a range of 10 – 80^{o} 2θ at a rate of 3^{o} per minute. Subsequently, the average crystallite size was determined with Rietveld refinement on Rigaku PDXL 2 software. The morphology of the samples was investigated with a JEOL JSM-5610 scanning electron microscope (SEM). The samples were prepared by affixing a small foam sample onto a carbon tape on a sample holder. The surface area of the samples was determined with a Quantachrome autosorb iQ2 Brunauer, Emmett, and Teller (BET) analyzer using approximately 100 mg samples. The transmission electron microscopy (TEM) was carried out with a JEM-2100F microscope with an accelerating voltage of 200 kV. The energy dispersive x-ray spectroscopy (EDS) was performed with the JEM-2100F microscope equipped with an Oxford Instruments EDS detector while operating in the scanning transmission electron microscopy mode.

Chapter 7: Interdigitated metal foil electrodes for rechargeable batteries[5]

7.1.Abstract

Metal alloy electrodes involving a conversion reaction offer high charge-storage capacities with working ions like lithium and sodium, but suffer from fast capacity fade due to huge volume changes occurring during cycling. We present here a novel interdigitated metal foil anode (IMFA) in which a nanosized active material like tin is integrated with an electrically conductive aluminum matrix to form a eutectic metal foil like Al-Sn. The IMFA does not require an additional inactive copper foil current collector, thereby allowing a dramatic increase in the effective capacity. The IMFA is manufactured with a simple inexpensive process traditionally used to make metal foils, allowing facile production at low cost and high volume. Although the approach is demonstrated here with tin and lithium, it can be used with a variety of alloying materials and working ions, opening up a new arena for rechargeable batteries.

7.2.Introduction

Although rechargeable non-aqueous lithium-ion batteries (LIBs) are ubiquitous ranging from consumer electronics to electric vehicles, the current technology needs to be improved to meet the increasing demands. With this perspective, recent studies have focused on improving the gravimetric energy density of LIBs by replacing the graphite anode with alloying materials, such as silicon, tin, germanium, and antimony. While bulk alloying materials undergo electrochemical pulverization due to large volume changes and internal stresses during lithiation, loading nanosized particles into a conductive matrix has been shown to allow reversible cycling [135–138]. However, their practical utility is plagued by large irreversible capacity loss in the first cycle and poor long-term cyclability. Efforts to increase energy density by adding alloying materials into graphite

[5]The majority of the work discussed in this chapter was carried out by Karl Kreder. Brian Heligman provided assistance in conducting experiments. K. Kreder, B. Heligman, A. Manthiram, "Interdigitated metal foil electrodes for rechargeable batteries," (*Submitted, Nature Energy, 2017)*.

without significantly compromising the performance have been limited to < 10 wt. % [139–145]. In an attempt to address the volume change, some studies have focused on thin films or composites of binary eutectic alloys, such as Al-Sn, Sn-Sb, and Ag-Sn [146–148]. The eutectic systems showed significant improvements in performance due to their even dispersion of the nanosized alloying material throughout the metal alloy. An alternate approach has been use of materials that can act both as an active material and as a current collector, reducing the amount of inactive material. Due to the high ductility required to produce foils, these investigations have been limited primarily to either aluminum or tin [149–151]. These studies have had limited impact due to poor cyclability, low coulombic efficiency, or low utilizable capacity of pure metallic foils. Most of the studies have concluded that the poor cyclability of such foils is due to the large volume changes (> 200%) with cycling and/or undesirable side reactions with the electrolyte.

7.3.Results

We present here a strategy in which an electrochemically active component Sn is interdigitated with an electrically conductive matrix Al. With this approach, hypoeutectic Al-Sn (AT) and Al-Zn-Sn (AZT) alloys are demonstrated as interdigitated metal foil anodes for lithium-ion batteries. The various compositions investigated and the weight percentages as measured by inductively coupled plasma – optical emission spectroscopy (ICP-OES) are given in Table 7.1. The effects of composition on morphology as well as electrochemical performance were evaluated over a range of 50 – 70 nominal wt. % tin. Additionally, the effect of zinc ranging from 1.5 to 2.5 wt. % was investigated.

Table 7.1. Nominal and measured compositions of the alloys

Nominal composition (wt. %)	Measured Al composition (wt. %)	Measured Sn composition (wt. %)	Measured Zn composition (wt. %)	Abbreviation
Al 50 – Sn 50	0.501	0.498	-	AT50
Al 40 – Sn 60	0.392	0.608	-	AT60
Al 30 – Sn 70	0.299	0.700	-	AT70
Al 47.5 – Zn 2.5 – Sn 50	0.475	0.501	0.023	AZT50
Al 38 – Zn 2 – Sn 60	0.378	0.598	0.019	AZT60
Al 28.5 – Zn 1.5 – Sn 70	0.284	0.701	0.016	AZT70

7.3.1. Morphology and Characterization

The morphology of both the AT and AZT alloys were characterized with scanning electron microscopy (SEM) as well as elemental maps generated with energy dispersive x-ray spectroscopy (EDX). Prior to the analysis, both the as-cast ingots as well as the foils were sectioned, mounted, and polished with traditional metallographic preparation techniques. The SEM micrographs reveal an archetypical binary eutectic alloy, shown in Figure 7.1b-g. Primary aluminum dendrites are surrounded by eutectic tin with no noticeable aluminum-tin eutectic structure. The observed microstructure are consistent with the Al-Sn phase diagram, given the hypoeutectic composition of the alloys as well as the location of the eutectic composition at 97.6 at % tin. The size scale of the aluminum and tin features seen in the micrographs of the as-cast ingots are on the order of tens of microns. The as-cast ingots were cold-rolled anisotropically, such that there was an ~ 100-times elongation along the x-axis, a corresponding ~ 100-times reduction along the z-axis, and little change along the y-axis, as seen in Figure 7.1b,n-s. The macroscopic deformation of the ingots into foils induced similar changes in the microstructure of the foils. Most importantly, the aluminum/tin feature sizes in the rolled foils were reduced to ~ 200 nm along the z-axis. The nanosizing of the tin features is believed to be critical in mitigating electrochemical milling and allowing reversible alloying with lithium [152]. The AZT alloys appear to have a slightly finer microstructure when compared to the corresponding AT alloys. The zinc does not appear as its own separate phase or in a eutectic microstructure, rather according to EDX, tin is spread evenly in both the aluminum and tin regions with a slight preference for the tin domains, Figure 7.2.

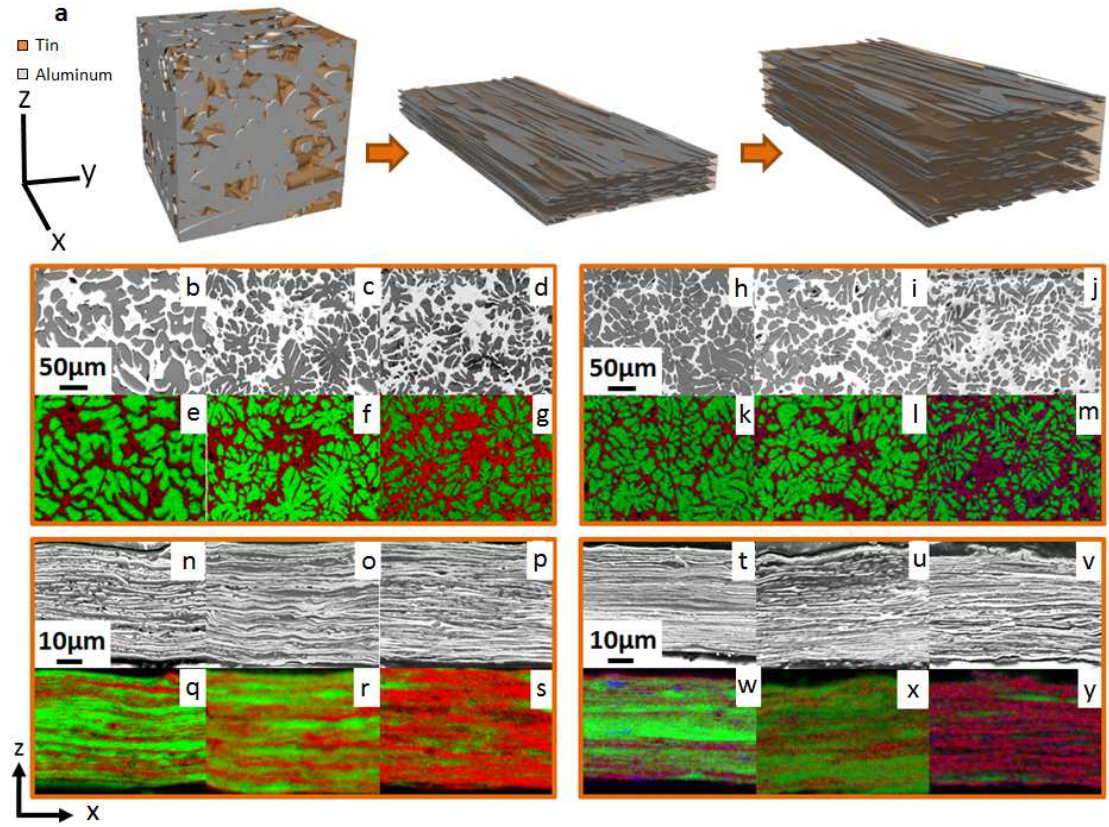

Figure 7.1. (a) Illustration of the cast ingot, rolled into a foil, and subsequent lithiation of the tin portion of the foil. SEM photos and EDX elemental maps of both AT and AZT alloys before and after rolling: (b,e) AT50, (c,f) AT60, (d,g) AT70, (h,k) AZT50, (i,l) AZT60, and (j,m) AZT70 as cast ingots. SEM photos and EDX elemental maps of alloy foils: (n,q) AT50, (o,r) AT60, (s,v) AT70, (t,w) AZT50, (u,x) AZT60, and (v,y) AZT70. Tin is shown as red, aluminum as green, and zinc as blue in the EDX elemental maps.

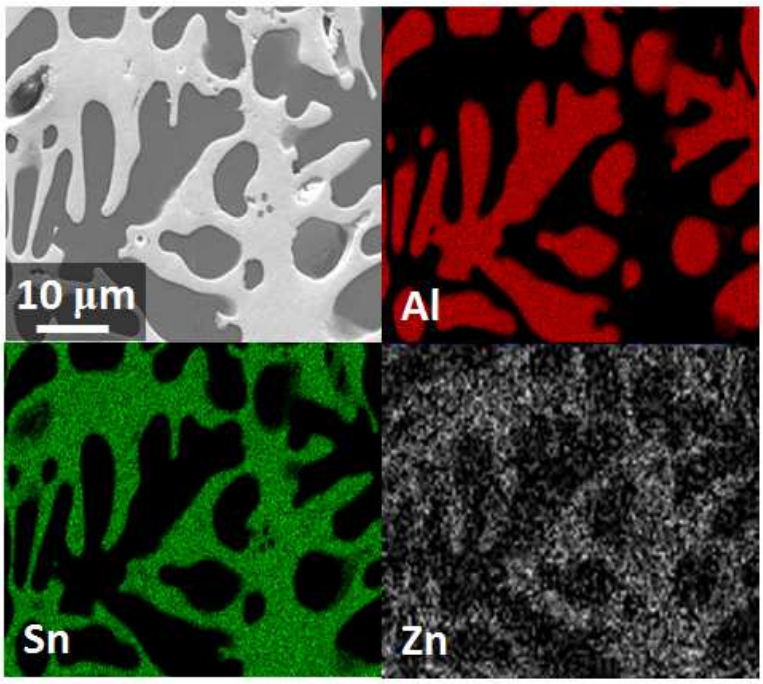

Figure 7.2. High magnification SEM of AZT70 and corresponding EDX elemental map.

The AT and AZT foils were also characterized with x-ray diffraction (XRD). The XRD patterns show that there are two pure phases, viz., Al and Sn, with no intermetallic compounds, Figure 7.3. The XRD patterns also show that the tin belongs to the *I4/mmm* space group and has a significant amount of texturing due to the excessive plastic deformation during rolling.

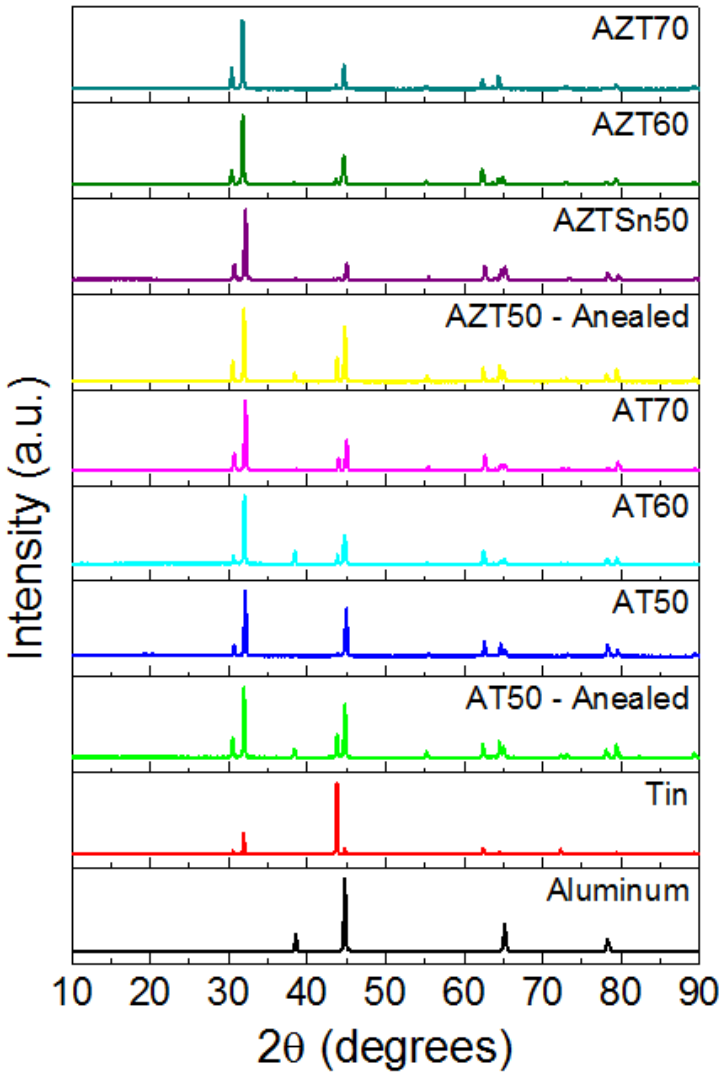

Figure 7.3. XRD patterns of AT and AZT alloys.

Texturing is indicated by a higher intensity of the (200) diffraction peak, which could be significantly reduced by annealing the foil. The aluminum has the cubic crystal structure with the *Fm3m* space group. The relative intensity of the aluminum peaks were found to increase with annealing due to the likely reduction in defects produced by cold work. Although there are no noticeable peaks corresponding to zinc in the AZT alloys, both the tin and aluminum peaks are shifted to lower 2θ values, indicating that zinc may have formed a solid solution with both aluminum and tin.

Due to the reduction in texturing with annealing, thermogravimetric analysis and differential scanning calorimetry (TGA/DSC) were performed on both the AT and AZT foils in air and argon atmospheres. The foils were heated above the aluminum-tin eutectic temperature (232 ^{o}C), at a rate of 5 ^{o}C/min, to understand the effects of atmosphere on the alloys during annealing. The TGA/DSC results of the AT foils are shown in Figure 7.4.

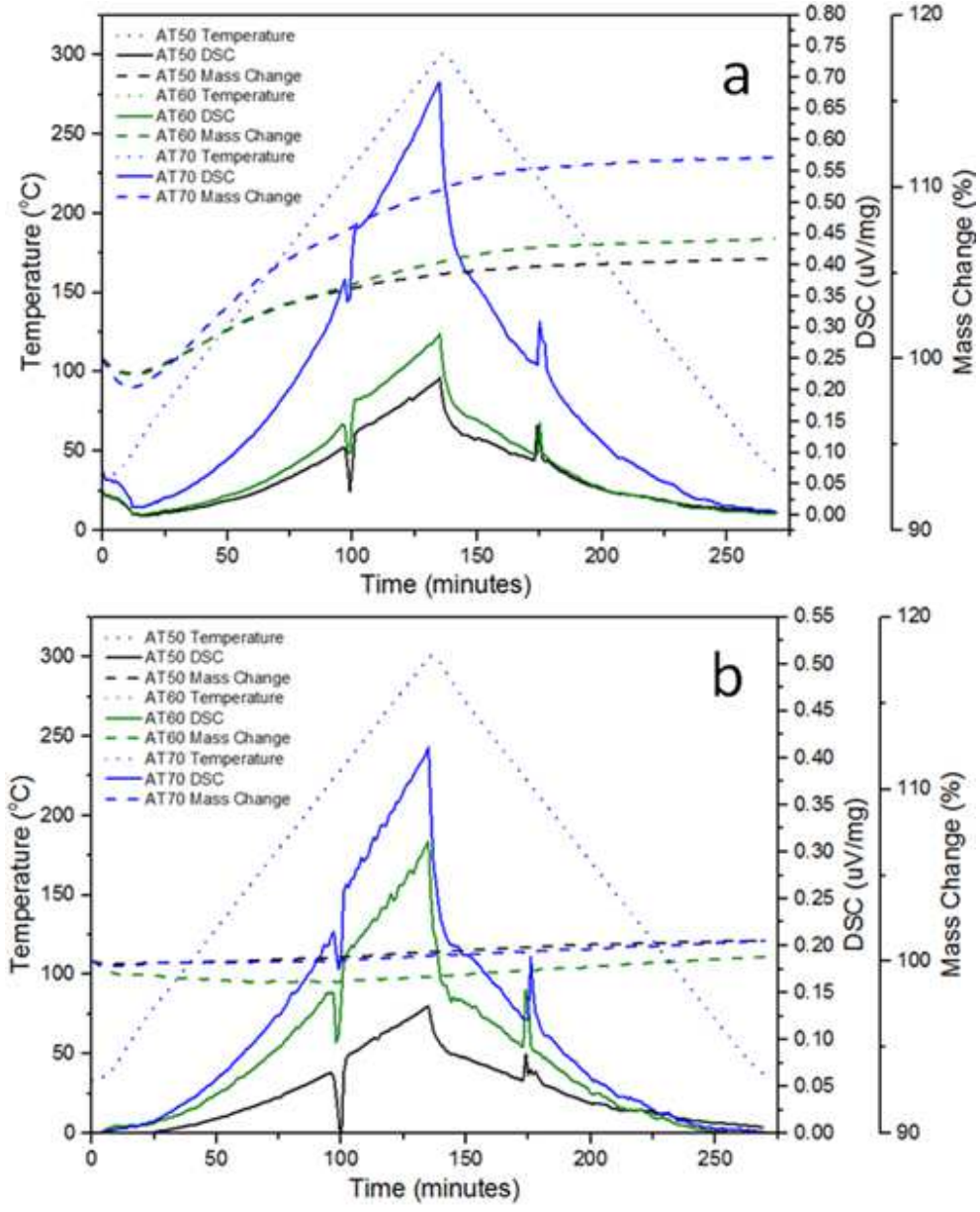

Figure 7.4. TGA/DSC results of heating the AT alloys in (a) air and (b) argon atmospheres.

Notably, the AT foils have an endothermic peak during heating at 232 ^{o}C, corresponding to the melting of the tin eutectic, and an exothermic peak during cooling, corresponding the recrystallization of the tin eutectic. Most interestingly, the change in weight while heating in air was significantly greater than the weight change when heating in argon. Furthermore, the percentage weight gain increased in alloys with increasing tin content, indicating that SnO_2 is likely forming. A significant amount of SnO_2 (~ 10 wt. %) was formed even at relatively low temperatures of > 50 ^{o}C. The TGA/DSC data directed the annealing of the AT and AZT foil anodes in argon rather than air to prevent oxidation.

7.4.Electrochemical Performance

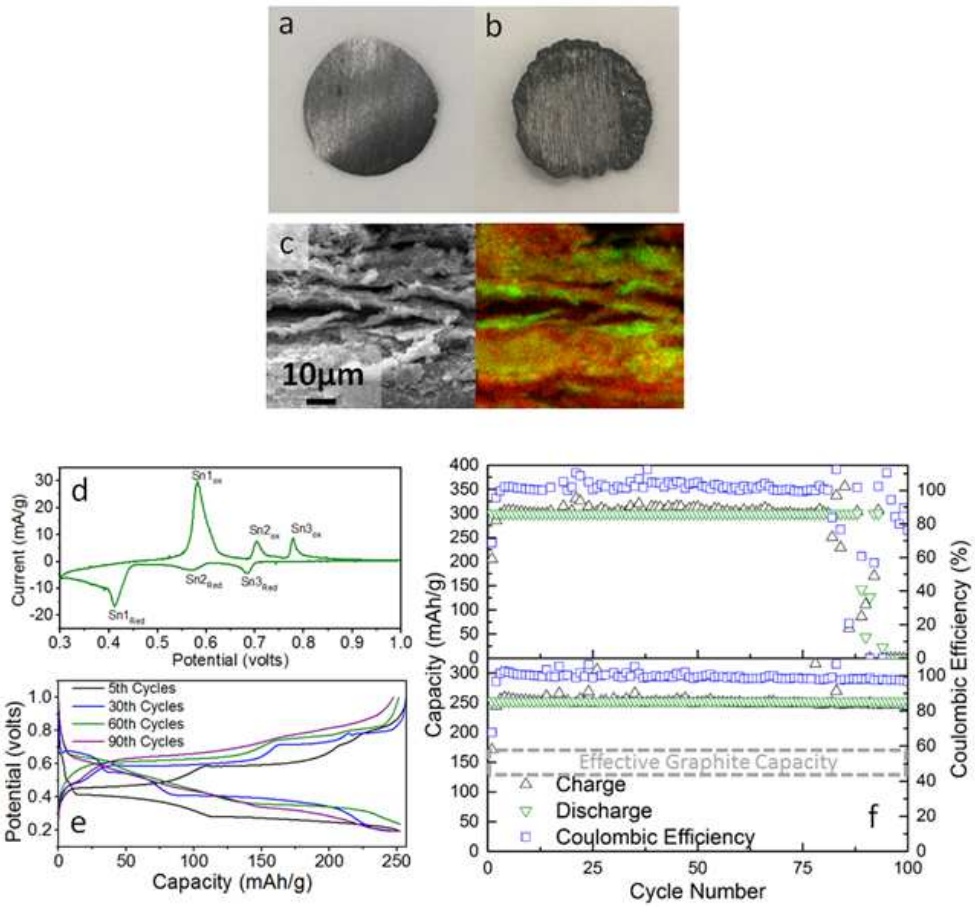

Fig. 7.5. Color images of AZT70 anode (a) before cycling (b) and after 40 cycles at C/10 rate at 250 mAh/g capacity. SEM image of (c) AZT70 anode after cycling with corresponding EDX elemental map.(d) Cyclic voltammogram of AZT70 at 0.3 – 1.0 V. (e) Charge/discharge profiles of AZT70 cycled at 250 mAh/g. (f) Cyclability of the AZT70 alloy cycled at C/5 rate, limited to both 250 and 300 mAh/g capacity ranges in lithium half-cells.

To fully understand the benefits of the IMFA strategy, the practically realized energy density of graphite/copper composite anodes must be understood. Traditional graphite anodes have a theoretical capacity of 370 mAh/g, but the realized capacity is only ~ 150 mAh/g when the weights of the copper foil, conductive carbon, and binder are included [32,153]. The IMFAs do not require any conductive carbon, binder, or an inactive copper current collector, so their capacities should be compared to the 150 mAh/g practical capacity of completed graphite anodes rather than the 370 mAh/g theoretical capacity of pure graphite.

The AT and AZT alloys were assembled into lithium half-cells and tested over several capacity limited discharge ranges with a 1.0 V cut-off limit on charge. Cyclability, heat treatments, and capacity limits tested of selected compositions are summarized in Table 7.2. The total foil weight was used when computing the gravimetric energy densities. The majority of the cycled capacity can be attributed to the first three redox peaks of Sn at 0.70, 0.57, 0.45 V, shown in Fig. 7.5d, rather than aluminum. These three voltage plateaus correspond to the two-phase regions of, respectively, Sn-Li_2Sn_3, Li_2Sn_3-LiSn, LiSn-Li_7Sn_3. Limiting the lower cut-off capacity prevented the lithiation/delithiation of a significant amount of aluminum. This can be seen in the cell with AZT70 by a lack of aluminum plateaus for cycles 30 to 90, Fig. 7.5e. Since the tin lithiation was limited to Li_7Sn_3, the theoretical capacity of the tin was reduced from 960 mAh/g to 509 mAh/g. The theoretical capacities of the various IMFAs were further reduced based on the wt. % of tin and are shown in Table 7.2.

Table 7.2. Electrochemical performances of cells assembled with Sn, AT, and AZT foils

Cell Type	Capacity Limit	Theo. Capacity	Rate	Cycles to 80%
Sn	300	960	C/10	11
AT50	300	254	C/10	40
AT60	300	305	C/10	30
AT70	300	356	C/10	33
AZT60	250	295	C/5	>98
AZT60	200	295	C/5	>152
AZT70	300	347	C/5	83
AZT70	250	347	C/5	>110
AZT60 -An	250	295	C/5	54
AZT60 -An	200	295	C/5	>102
AZT70 -An	300	347	C/5	61
AZT70 -An	250	347	C/5	81

Overall, the AZT alloys performed better than the annealed AZT and the AT alloys. Interestingly, although the argon-annealed AZT alloys were more quickly able to achieve capacity from tin only, Figure 7.6, they were not able to cycle as long as the corresponding un-annealed alloys. With a capacity limit of 250 mAh/g, the AZT70 alloy was able to achieve more than 110 cycles at an average coulombic efficiency of 99.3%, shown in Figure 2f.

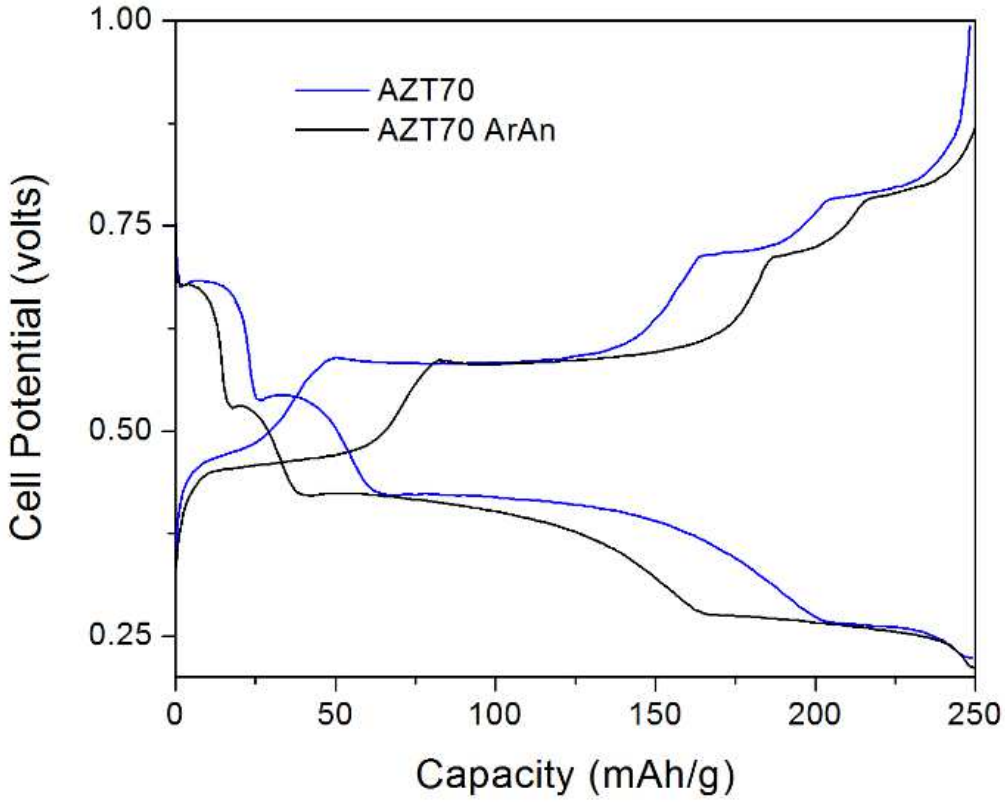

Figure 7.6. Comparison of the 10th charge-discharge cycle of the annealed and un-annealed IMFAs.

The AZT70 alloy which was cycled at a higher capacity of 300 mAh/g was able to cycle for 83 cycles before abruptly dying. This represents a utilization of > 87% of the theoretical capacity of tin in the AZT70 alloy. In contrast, the AT70 alloy was unable to achieve 300 mAh/g of capacity from tin, but rather had a maximum peak tin capacity of only 273 mAh/g, which implies a utilization of only 76%. The difference in performance between the AT and AZT anodes is attributed to increased accessibility of tin in the zinc doped system. The tin accessibility may be higher due to an intrinsic change in the ionic conductivity of the tin-zinc solid solution, or due to the introduction of new unobserved phase boundaries between eutectic tin-zinc.

The first several charge-discharge cycles of the IMFAs were carried out below 0.25 V, which caused some of the lithium to initially alloy with the aluminum as well as with tin. These cycles forced the delamination of the Al-Sn foil, which created an exfoliated

foil, see Figure 2a-c. Exfoliation of the foil dramatically increased the accessibility of the tin as seen by the increase in capacity above 0.25 V from 5 mAh/g on the first cycle to 190 mAh/g on the 10th cycle and 236 mAh/g by the 20th cycle. The first cycle coulombic efficiency of AZT70 that was limited to 300 mAh/g was 72.9%. However, much of the "loss" during the first cycle was recovered during the subsequent 15 cycles as lithium was extracted (coulombic efficiency > 100%) from the aluminum alloy, raising the effective first cycle efficiency to 87.2%.

7.5. Discussion

Although this work primarily focused on the Al-Sn system, Al-Sn is just one manifestation of a broader framework, which applies to a number of other eutectic alloy systems. The Al-Sn system is a prototypical example of fabricating a nano-sized lithium alloying material intimately interdigitated into a ductile conductive inert metal matrix by cold rolling a eutectic metal ingot. A primary benefit of such systems is the potential for inexpensive and simple production of high capacity anode materials, without requiring the expensive slurry processing steps needed with conventional electrodes. Furthermore, having an active alloying phase interdigitated with an inactive and ductile phase allows the accommodation of volume change upon cycling.

Only ductile metals, which contain little or no intermetallic compounds, are conducive to being cold rolled into metal foils. Therefore, any alloy system that can be considered should meet the following three criteria. First, the alloy must either form a binary eutectic or monotectic with little to no intermetallic compounds. Second, one of the two elements should be able to alloy with lithium reversibly. Third, the conductive matrix metal should ideally be inactive, but if it is not, the potential range over which it is alloyed with lithium should not overlap with or should not be cycled to a potential that begins to significantly alloy with lithium. In addition to the aforementioned technical criteria, there are additional considerations such as cost (< $10/lb) and annualized production quantities (>10,000 metric tons) to practically consider for battery anodes. Based on these criteria, there exist at least 10 other systems besides Al-Sn, which meet these criteria and deserve exploration. They include: Zn-Sn, Sn-Pb, Cd-Sn, Ni-Pb, Sn-Bi, Cu-Pb, Cu-Bi, Bi-Pb, Bi-Zn, and Bi-Cd. Furthermore, the strategy can be extended to

other rechargeable batteries, such as sodium-ion, magnesium-ion, zinc-ion, etc., with appropriate alloy systems.

7.6. Conclusion

The present work demonstrated an aluminum-tin and aluminum-zinc-tin eutectic foils as an integrated metal foil anode for a lithium-ion batteries. The AT/AZT alloys represent a novel topology for creating high capacity, low-cost anodes for lithium-ion batteries. The AZT70 alloy demonstrated an effective doubling of capacity compared to a graphite/copper composite anode. Additionally, the AZT70 anode had high effective first cycle coulombic efficiency of 87.2% and was able to demonstrate over 110 cycles at 250 mAh/g with > 99.3% coulombic efficiency. All metrics of this first iteration of the AT/AZT IMFA system, including capacity, cost, coulombic efficiency, average voltage, effective first cycle losses, and rate capability, are promising for practical viability. The IMFA approach offers a new framework to develop high capacity alloy anodes with an abundant number of compositional, elemental, and processing variations available for rechargeable batteries based on lithium, sodium, magnesium, zinc, calcium, etc.

7.7. Materials and Methods

7.7.1. Synthesis

The Al-Sn and Al-Zn-Sn metal foils were synthesized as follows. Approximately 50 g of the desired weight ratios of aluminum (McMaster-Carr, 1100 series >99.5%), zinc (RotoMetals, >99.7%), and tin (Metal Shipper Inc., >99.9%) were melted in air at 750 ^{o}C in a high temperature graphite crucible. The melt was then cast into a graphite mold and allowed to cool to form rectangular ingots of ~ 35 x 13 x 7 mm in size. The foils were made by rolling sections of the ingots of ~ 7 x 7 x 3.5 mm in size with a manual Durston rolling mill equipped with 60 mm diameter rollers. The rolling was performed such that the 3.5 mm dimension was reduced to 0.02-0.03 mm while elongation was focused on one of the 7 mm dimensions. Subsequent to rolling, some of the foils were annealed in either air or argon atmospheres at 185 ^{o}C for 1 h.

7.7.2. Materials characterization

X-ray diffraction patterns were collected in continuous mode over a 2θ range of 10 - 100^{o} 2θ at a rate of 3^{o} s^{-1}. Both the foils and ingots were mounted and polished with traditional metallographic sample preparation techniques prior to analysis in the SEM. Briefly, samples were first sectioned and mounted in a thermoset polymer (Beuhler, Inc., PhenoCure). The mounted samples were then polished first with 6 and 1 μm diamond suspensions followed by a final polish with an aqueous suspension of 0.1 μm alumina. The samples were then washed with water and ethanol and quickly dried. It should be noted that all the alloys had a high degree of reactivity with water and the washing step etched the surface. There were no subsequent etching steps. Scanning electron microscopy (SEM) data were taken on a JEOL JSM-5610 SEM operating at a 20 keV accelerating voltage. Energy dispersive X-ray spectroscopy (EDX) elemental maps were generated with an Oxford Instruments INCAx-act detector. Inductively coupled plasma optical emission spectroscopy (ICP-OES) was performed on a Varian 715-ES instrument to determine the compositions of the various alloys. The Varian 715-ES instrument was calibrated with 10,000 ppm standard solutions of aluminum, zinc, and tin (Ricca Chemical). Thermogravimetric analysis (TGA) was conducted with ~ 15 mg samples on a Jupiter STA 449 F3 in both air and argon atmospheres at a heating rate of 5 ^{o}C/min.

7.7.3. Electrochemical Characterization

Coin cells (CR 2032) were constructed to test the electrochemical characteristics of the as made foils. The foil strips (~ 20 μm thick) were punched into 12 mm disks weighing ~ 10 mg. Metallic lithium chips (MTI corporation) were used as the counter electrode and glass fiber prefilters (Millipore APFA04700) were used as separators. The electrolyte used was a 3 : 7 ratio of monoflouro ethylene carbonate (FEC) to ethylene carbonate (EC) with 1 M bis(trifluoromethane)sulfonimide lithium (LiTSFI) and 3% vinylene carbonate (VC). The coin cells were constructed in an inert (O_2 < 5 ppm) dry (H_2O < 1 ppm) glovebox with an argon atmosphere. The galvanostatic charge-discharge and cyclic voltammetry were performed with a BT-2000 Arbin instruments battery cycler. The first 2 cycles of the galvanostatic charge-discharge testing were conditioning cycles in which a rate of C/10 was used with capacity limited cutoffs for the nominal

capacities of 150, 200, 250, and 300 mAh/g cells. Subsequently, the cells were then cycled at their specified C-rates such that they were capacity limited on discharge and then charged at a constant current to 1.0 V on charge. Aberrant behavior was observed upon several charges early in the cycling, shown in Figure 7.7.

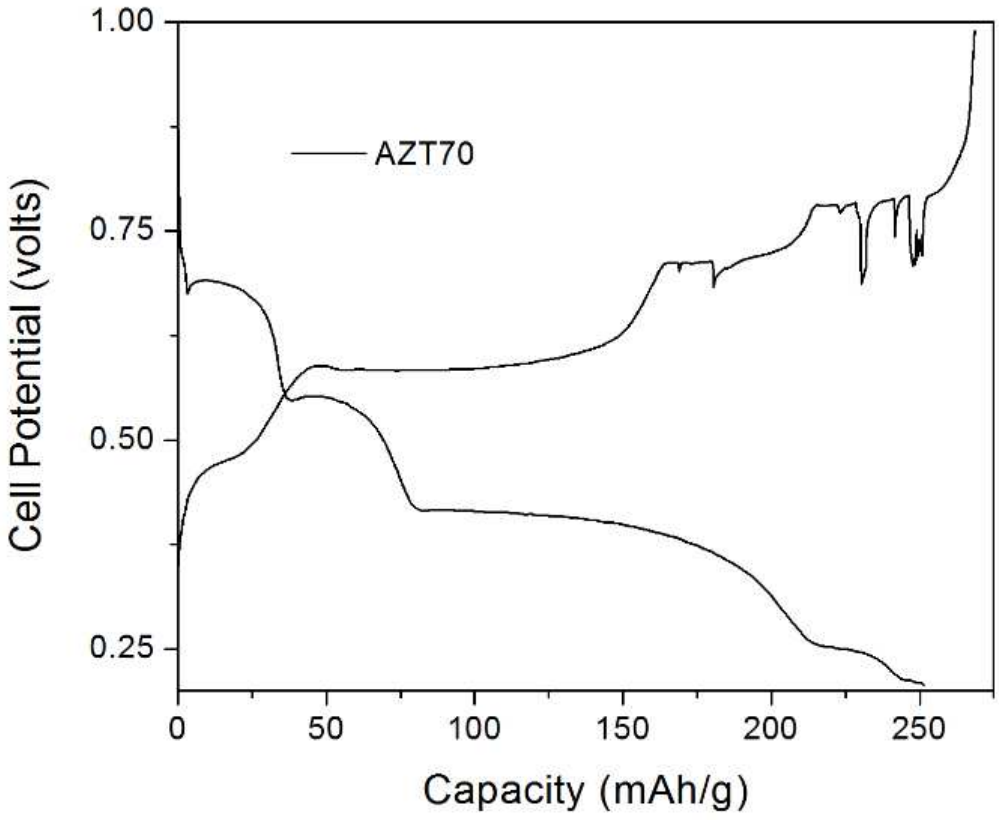

Figure 7.7. Aberrant behavior during the 24th charge-discharge of the AZT70 IMFA.

This behavior was attributed to the inability of the coin cell geometry to accommodate the alloying volume expansion. Given that these aberrant cycles presented with coulombic efficiencies over 100 percent, they were excluded from average columbic efficiency calculations. Cyclic voltammograms were then collected with a sweep rate of 0.0005 V s^{-1} over two voltage ranges between 0.3 V to 1.0 V.

Chapter 8: Summary

The aim of the presented work was to improve the electrochemical properties of novel high capacity electroactive materials for lithium ion batteries. This was demonstrated for both a high-voltage polyanion cathode, $LiCoPO_4$, as well as for a novel interdigitated metal foil anode. The properties of the $LiCoPO_4$ were successfully modified via several low temperature synthesis methods which, in combination, increased the initial discharge capacity from 69 to 145 mAh/g. Additionally, the capacity retention as well as coulombic efficiency of the cells was dramatically improved. The coulombic efficiency of the LFP-LCVP cells was shown to be higher than 99%. The IMFA demonstrated a new engineering framework for designing high capacity lithium alloying materials. Not only did the IMFA have an effective capacity of twice that of graphite over 80 cycles, it also did so at a high coulombic efficiency >98.5%, a commercially practical rate C/5, with first cycle irreversible losses of around 12%. On all metrics, the IMFA is presently a novel material which could be developed as a commercially viable anode.

Firstly, the low temperature MW-ST synthesis of three phase pure polymorphs of $LiCoPO_4$ was demonstrated. Two of the three polymorphs, *Cmcm* and $Pn2_1a$, had not previously been presented. Although, these materials were not good electroactive materials, understanding the dependence of the formation of these polymorphs on both the concentrations of water and ammonium hydroxide facilitated the further work. Additionally, the structural electrochemical and spectroscopic properties were reported for the first time.

Second, the aliovalent substitution of vanadium in lithium cobalt phosphate was demonstrated via a two-step synthesis method. Specifically, the vanadium substituted form of the $Pn2_1a$ polymorph was formed via a MW-ST method and was subsequently converted to a vanadium substituted *Pnma* polymorph via calcination at 525 ^{o}C. The vanadium substituted LiCoPO4 demonstrated both increased electrical and ionic conductivity. The improvement in the solid-state properties increased the first cycle gravimetric capacity from 69 to 115 mAh/g.

Third, electrolyte side reactions with $LiCoPO_4$ cathode were mitigated via a novel MW-ST approach to coating $LiCoPO_4$ nanoparticles with $LiFePO_4$. The monolithic coating of $LiFePO_4$ was conclusively verified through TEM, EDX, and XPS. The methodology of coating nanoparticles using an MW-ST process takes advantage of the surface localized heating and could be extended to many coat nanoparticles with many other materials. The LFP coating of LCVP improved in the initial capacity of the material from 115 to 145 mAh/g.

Fourth, a novel MW-ST synthesis process of high surface area metal nanofoams was demonstrated which successful produced copper, silver, and nickel nanofoams. This process is a cheap facile inexpensive method for producing metal foams which can be used in many clean energy applications ranging from catalytic to electrochemical. The foams could be employed as a high surface area current collector for lithium ion batteries.

Finally, the interdigitated metal foil anode was presented as a novel framework for the design of high capacity lithium alloying anodes. Simple metallurgical processes were employed to form a nanostructured foil anode allowing production at scale. Additionally, only one archetypical system was presented with the aluminum-tin eutectic system. At least 10 other similar systems exist and deserve further investigation. The current performance of the AZT IMFA was able to double the effective capacity of graphite for more than 80 cycles. There are a large number of experimental parameters that have not been explored that will likely vastly improve the performance of these systems.

Although the work on $LiCoPO_4$ was not successful in producing a material that can be used commercially in batteries it demonstrated new methods for synthesis that have helped to dramatically improve performance. This has contributed to the knowledge base of understanding of this material. The introduction of the IMFA framework has demonstrated a step-change in the performance of foil type anodes. The IMFA system already performs very well on all common metrics and can likely be developed further to the point of commercialization.

Appendix A: List of Publications Related to this Work

1. K. J. Kreder, G. Assat, A. Manthiram, Microwave-Assisted Solvothermal Synthesis of Three Polymorphs of $LiCoPO_4$ and Their Electrochemical Properties. Chem. Mater. 27, 5543–5549 (2015).

2. K. J. Kreder, G. Assat, A. Manthiram, Aliovalent Substitution of V^{3+} for Co^{2+} in $LiCoPO_4$ by a Low-Temperature Microwave-Assisted Solvothermal Process. Chem. Mater. 28, 1847–1853 (2016).

3. K. J. Kreder, A. Manthiram, Vanadium-Substituted $LiCoPO_4$ Core with a Monolithic $LiFePO_4$ Shell for High-Voltage Lithium-Ion Batteries. ACS Energy Lett., 64–69 (2016).

4. K. J. Kreder, A. Manthiram, Metal nanofoams via a facile microwave-assisted solvothermal process. Chem. Commun. 53, 865–868 (2017).

5. K. J. Kreder, B.T. Heligman, A. Manthiram, Interdigitated metal foil electrodes for rechargeable batteries. *Submitted Nature Energy*

References

(1) Liu, J.; Zhang, J. G.; Yang, Z.; Lemmon, J. P.; Imhoff, C.; Graff, G. L.; Li, L.; Hu, J.; Wang, C.; Xiao, J.; et al. Materials science and materials chemistry for large scale electrochemical energy storage: From transportation to electrical grid. *Adv. Funct. Mater.* **2013**, *23* (8), 929–946.

(2) Xu, W.; Xiao, J.; Wang, D.; Zhang, J. J.-G.; Zhang, J. J.-G. Crown Ethers in Nonaqueous Electrolytes for Lithium/Air Batteries. *Electrochem. Solid-State Lett.* **2010**, *13* (4), A48.

(3) Aurbach, D.; Markovsky, B.; Salitra, G.; Markevich, E.; Talyossef, Y.; Koltypin, M.; Nazar, L.; Ellis, B.; Kovacheva, D. Review on electrode-electrolyte solution interactions, related to cathode materials for Li-ion batteries. *J. Power Sources* **2007**, *165* (2), 491–499.

(4) Afanasyeva, S.; Breyer, C.; Engelhard, M. The Impact of Cost Dynamics of Lithium-Ion Batteries on the Economics of Hybrid PV-Battery-GT Plants and the Consequences for Competitiveness of Coal and Natural Gas-Fired Power Plants. *Proc. 10th Int. Renew. Energy Storage Conf.* **2016**, No. March, 1–24.

(5) Zhang, B.; Zhong, J.; Cheng, Z. Mechanism of formation of anodic excursion peaks on lead electrode in sulfuric acid. *J. Power Sources* **2011**, *196* (13), 5719–5724.

(6) Scrosati, B. Lithium Rocking Chair Batteries: An Old Concept? *J. Electrochem. Soc.* **1992**, *139* (10), 2776.

(7) Manthiram, A. Materials challenges and opportunities of lithium ion batteries. *J. Phys. Chem. Lett.* **2011**, *2* (3), 176–184.

(8) Whittingham, M. S. Electrical Energy Storage and Intercalation Chemistry. *Science*

(80-.). **1976**, *192* (4244), 1126–1127.

(9) Takehara, Z. Future prospects of the lithium metal anode. *J. Power Sources* **1997**, *68* (1), 82–86.

(10) Koch, V. R.; Young, J. H. The Stability of the Secondary Lithium Electrode in Tetrahydrofuran-Based Electrolytes. *J. Electrochem. Soc.* **1978**, *125* (9), 1371.

(11) Ota, H.; Shima, K.; Ue, M.; Yamaki, J. ichi. Effect of vinylene carbonate as additive to electrolyte for lithium metal anode. *Electrochim. Acta* **2004**, *49* (4), 565–572.

(12) Mizushima, K.; Jones, P. C.; Wiseman, P. J.; Goodenough, J. B. Li_xCoO_2 ($0 < x < 1$): A new cathode material for batteries of high energy density. *Mater. Res. Bull.* **1980**, *15* (6), 783–789.

(13) Padhi, A. K.; Nanjundaswamy, K. S.; Goodenough, J. B. Phospho-olivines as Positive-Electrode Materials for Rechargeable Lithium Batteries. *J. Electrochem. Soc.* **1997**, *144* (4), 1188–1194.

(14) Kim, J.; Manthiram, A. A manganese oxyiodide cathode for rechargeable lithium batteries. **1997**, *480* (1972), 478–480.

(15) Thackeray, M. M. Manganese oxides for lithium batteries. *Prog. Solid State Chem.* **1997**, *25* (1–2), 1–71.

(16) Huang, H.; Yin, S.-C.; Nazar, L. F. Approaching Theoretical Capacity of $LiFePO_4$ at Room Temperature at High Rates. *Electrochem. Solid-State Lett.* **2001**, *4* (10), A170–A172.

(17) Shiratsuchi, T.; Okada, S.; Yamaki, J.; Yamashita, S.; Nishida, T. Cathode performance of olivine-type $LiFePO_4$ synthesized by chemical lithiation. *J. Power Sources* **2007**, *173* (2), 979–984.

(18) Wang, L.; Zhang, L.; Li, J.; Gao, J. First-Principles Study of Doping in $LiMnPO_4$. *Int. J. Electrochem. Sci.* **2012**, *7*, 3362–3370.

(19) Ellis, B.; Kan, W. H.; Makahnouk, W. R. M.; Nazar, L. F. Synthesis of nanocrystals and morphology control of hydrothermally prepared $LiFePO_4$. *J. Mater. Chem.* **2007**, *17*, 3248.

(20) Delacourt, C.; Laffont, L.; Bouchet, R.; Wurm, C.; Leriche, J.-B.; Morcrette, M.; Tarascon, J.-M.; Masquelier, C. Toward Understanding of Electrical Limitations (Electronic, Ionic) in $LiMPO_4$ (M=Fe, Mn) Electrode Materials. *J. Electrochem. Soc.* **2005**, *152* (5), A913.

(21) Bramnik, N. N.; Bramnik, K. G.; Baehtz, C.; Ehrenberg, H. Study of the effect of different synthesis routes on Li extraction-insertion from $LiCoPO_4$. *J. Power Sources* **2005**, *145*, 74–81.

(22) Bramnik, N. N.; Nikolowski, K.; Baehtz, G.; Bramnik, K. G.; Ehrenberg, H. Phase transitions occurring upon lithium insertion-extraction of $LiCoPO_4$. *Chem. Mater.* **2007**, *19* (2), 908–915.

(23) Xu, Y.-N. Comparative studies of the electronic structure of $LiFePO_4$, $FePO_4$, $Li3PO_4$, $LiMnPO_4$, $LiCoPO_4$, and $LiNiPO_4$. *J. Appl. Phys.* **2004**, *95* (2004), 6583.

(24) Dimesso, L.; Becker, D.; Spanheimer, C.; Jaegermann, W. Investigation of graphitic carbon foams/$LiNiPO_4$ composites. *J. Solid State Electrochem.* **2012**, *16* (12), 3791–3798.

(25) Minakshi, M.; Singh, P.; Appadoo, D.; Martin, D. E. Synthesis and characterization of olivine $LiNiPO_4$ for aqueous rechargeable battery. *Electrochim. Acta* **2011**, *56* (11), 4356–4360.

(26) Omenya, F.; Chernova, N. a.; Wang, Q.; Zhang, R.; Whittingham, M. S. The structural and electrochemical impact of li and fe site substitution in $LiFePO_4$. *Chem. Mater.* **2013**, *25*, 2691–2699.

(27) Xu, Y.-N.; Chung, S.-Y.; Bloking, J. T.; Chiang, Y.-M.; Ching, W. Y. Electronic Structure and Electrical Conductivity of Undoped $LiFePO_4$. *Electrochem. Solid-*

State Lett. **2004**, *7* (6), A131.

(28) Wang, D.; Wu, X.; Wang, Z.; Chen, L. Cracking causing cyclic instability of $LiFePO_4$ cathode material. *J. Power Sources* **2005**, *140* (1), 125–128.

(29) Maccario, M.; Croguennec, L.; Desbat, B.; Couzi, M.; Le Cras, F.; Servant, L. Raman and FTIR Spectroscopy Investigations of Carbon-Coated Li_xFePO_4 Materials. *J. Electrochem. Soc.* **2008**, *155*, A879.

(30) Yang, S.; Zhou, X.; Zhang, J.; Liu, Z. Morphology-controlled solvothermal synthesis of $LiFePO_4$ as a cathode material for lithium-ion batteries. *J. Mater. Chem.* **2010**, *20* (37), 8086.

(31) Xu, K. Nonaqueous Liquid Electrolytes for Lithium-Based Rechargeable Batteries Nonaqueous Liquid Electrolytes for Lithium-Based Rechargeable Batteries. *Chem. Rev.* **2004**, *104* (September), 4303.

(32) Yazami, R.; Universitaire, D. A reversible graphite-lithium negative electrode for electrochemical generators. *J. Power Sources* **1983**, *9*, 365–371.

(33) Ohzuku, T. Formation of Lithium-Graphite Intercalation Compounds in Nonaqueous Electrolytes and Their Application as a Negative Electrode for a Lithium Ion (Shuttlecock) Cell. *J. Electrochem. Soc.* **1993**, *140* (9), 2490.

(34) Rosamaría Fong, Ulrich von Sacken, J. R. D. Studies of Lithium Intercalation into Carbons Using Nonaqueous Electrochemical Cells. *J. Electrochem. Soc.* **1990**, *137* (7), 2009–2013.

(35) Marom, R.; Amalraj, S. F.; Leifer, N.; Jacob, D.; Aurbach, D. A review of advanced and practical lithium battery materials. *J. Mater. Chem.* **2011**, *21* (27), 9938.

(36) Li, W.; Mckinnon, W. R.; Dahn, J. R. Lithium Intercalation from Aqueous Solutions. *J. Electrochem. Soc.* **1994**, *141* (9), 2310–2316.

(37) Peled, E. Improved Graphite Anode for Lithium-Ion Batteries Chemically. *J.*

Electrochem. Soc. **1996**, *143* (1), L4.

(38) Bohn, P.; Barragan, S. A. G.; Komsiyska, L.; Wittstock, G. Performance and the Characteristics of Thermally Stressed Anodes in Lithium Ion Cells. *J. Electrochem. Soc.* **2015**, *162* (2), A3110–A3115.

(39) Downie, L. E.; Krause, L. J.; Burns, J. C.; Jensen, L. D.; Chevrier, V. L.; Dahn, J. R. In Situ Detection of Lithium Plating on Graphite Electrodes by Electrochemical Calorimetry. *J. Electrochem. Soc.* **2013**, *160* (4), A588–A594.

(40) Nitta, N.; Yushin, G. High-Capacity Anode Materials for Lithium-Ion Batteries : Choice of Elements and Structures for Active Particles. *Part. Part. Syst. Charact.* **2014**, *31*, 317–336.

(41) Obrovac, M. N.; Chevrier, V. L. Alloy Negative Electrodes for Li-Ion Batteries. *Chem. Rev.* **2014**, *114*, 11444–11502.

(42) Li, H.; Shi, L.; Lu, W.; Huang, X.; Chen, L. Studies on Capacity Loss and Capacity Fading of Nanosized SnSb Alloy Anode for Li-Ion Batteries. *J. Electrochem. Soc.* **2001**, *148* (8), A915–A922.

(43) Zhang, T.; Fu, L. J.; Gao, J.; Wu, Y. P.; Holze, R.; Wu, H. Q. Nanosized tin anode prepared by laser-induced vapor deposition for lithium ion battery. *J. Power Sources* **2007**, *174* (2), 770–773.

(44) Kasavajjula, U.; Wang, C.; Appleby, A. J. Nano- and bulk-silicon-based insertion anodes for lithium-ion secondary cells. *J. Power Sources* **2007**, *163* (2), 1003–1039.

(45) Baggetto, L.; Allcorn, E.; Manthiram, A.; Veith, G. M. Cu_2Sb thin films as anode for Na-ion batteries. *Electrochem. commun.* **2013**, *27*, 168–171.

(46) Allcorn, E.; Manthiram, A. High-rate, high-density FeSb–TiC–C nanocomposite anodes for lithium-ion batteries. *J. Mater. Chem. A* **2015**, *3* (7), 3891–3900.

(47) Allcorn, E.; Kim, S. O.; Manthiram, A. Lithium diffusivity in antimony-based

intermetallic and FeSb–TiC composite anodes as measured by GITT. *Phys. Chem. Chem. Phys.* **2015**, *17* (43), 28837–28843.

(48) Allcorn, E.; Kim, S. O.; Manthiram, A. Thermal stability of active/inactive nanocomposite anodes based on Cu_2Sb in lithium-ion batteries. *J. Power Sources* **2015**, *299*, 501–508.

(49) Manthiram, A.; Goodenough, J. B. Lithium insertion into $Fe_2(SO_4)_3$ framworks. *J. Power Sources* **1989**, *26*, 403–408.

(50) Manthiram, A.; Goodenough, J. B. Lithium insertion into $Fe_2(MO_4)_3$ frameworks: Comparison of M = W with M = Mo. *J. Solid State Chem.* 1987, pp 349–360.

(51) Okada, S.; Sawa, S.; Egashira, M.; Yamaki, J. I.; Tabuchi, M.; Kageyama, H.; Konishi, T.; Yoshino, A. Cathode properties of phospho-olivine $LiMPO_4$ for lithium secondary batteries. *J. Power Sources* **2001**, *97–98*, 430–432.

(52) Clemens, O.; Bauer, M.; Haberkorn, R.; Springborg, M.; Beck, H. P. Synthesis and Characterization of Vanadium-Doped $LiMnPO_4$-Compounds: $LiMn(PO_4)_x(VO_4)_{1-x}$ (0.8 <= x <= 1.0). *Chem. Mater.* **2012**, *24*, 4717–4724.

(53) Chen, J.; Wang, S.; Whittingham, M. S. Hydrothermal synthesis of cathode materials. *J. Power Sources* **2007**, *174*, 442–448.

(54) Deniard, P.; Dulac, a. M.; Rocquefelte, X.; Grigorova, V.; Lebacq, O.; Pasturel, a.; Jobic, S. High potential positive materials for lithium-ion batteries: Transition metal phosphates. *J. Phys. Chem. Solids* **2004**, *65*, 229–233.

(55) Johannes, M. D.; Hoang, K.; Allen, J. L.; Gaskell, K. Hole polaron formation and migration in olivine phosphate materials. *Phys. Rev. B - Condens. Matter Mater. Phys.* **2012**, *85*, 1–6.

(56) Jähne, C.; Neef, C.; Koo, C.; Meyer, H.-P.; Klingeler, R. A new $LiCoPO_4$ polymorph via low temperature synthesis. *J. Mater. Chem. A* **2013**, *1*, 2856.

(57) Amador, U.; Gallardo-Amores, J. M.; Heymann, G.; Huppertz, H.; Morán, E.; Arroyo y de Dompablo, M. E. High pressure polymorphs of $LiCoPO_4$ and $LiCoAsO_4$. *Solid State Sci.* **2009**, *11*, 343–348.

(58) Murugan, a V.; Muraliganth, T.; Manthiram, a. Comparison of Microwave Assisted Solvothermal and Hydrothermal Syntheses of $LiFePO_4$ / C Nanocomposite Cathodes for Lithium Ion Batteries. *J. Phys. Chem. C* **2008**, *112*, 14665–14671.

(59) Kim, S.-H.; Lee, S. Y.; Yi, G.-R.; Pine, D. J.; Yang, S.-M. Microwave-assisted self-organization of colloidal particles in confining aqueous droplets. *J. Am. Chem. Soc.* **2006**, *128* (33), 10897–10904.

(60) Zhang, Y.; Feng, H.; Wu, X.; Wang, L.; Zhang, A.; Xia, T.; Dong, H.; Liu, M. One-step microwave synthesis and characterization of carbon-modified nanocrystalline $LiFePO_4$. *Electrochim. Acta* **2009**, *54*, 3206–3210.

(61) Wen, H.; Cao, M.; Sun, G.; Xu, W.; Wang, D.; Zhang, X.; Hu, C. Hierarchical three-dimensional cobalt phosphate microarchitectures: Large-scale solvothermal synthesis, characterization, and magnetic and microwave absorption properties. *J. Phys. Chem. C* **2008**, *112*, 15948–15955.

(62) Murugan, A. V.; Muraliganth, T.; Ferreira, P. J.; Manthiram, A. Dimensionally Modulated, Single-Crystalline $LiMPO_4$ (M= Mn, Fe, Co, and Ni) with Nano-Thumblike Shapes for High-Power Energy Storage. *Inorg. Chem.* **2009**, *48* (3), 946–952.

(63) Baker, R. W.; Lokhandwala, K. Natural gas processing with membranes: An overview. *Ind. Eng. Chem. Res.* **2008**, *47*, 2109–2121.

(64) Nakamoto, K. *Infrared and Raman Spectra of Inorganic and Coordination Compounds*, 6th ed.; Wiley: New York, NY, 2008.

(65) Paques-Ledent, M. T.; Tarte, P. Vibrational studies of olivine-type compounds--II

Orthophosphates , -arsenates and -vanadates $A^{I}B^{II}X^{V}O4$. *Spectrochim. Acta Part A* **1974**, *30* (1973), 673–689.

(66) Markevich, E.; Sharabi, R.; Haik, O.; Borgel, V.; Salitra, G.; Aurbach, D.; Semrau, G.; Schmidt, M. a.; Schall, N.; Stinner, C. Raman spectroscopy of carbon-coated $LiCoPO_4$ and $LiFePO_4$ olivines. *J. Power Sources* **2011**, *196*, 6433–6439.

(67) Wu, J.; Dathar, G. K. P.; Sun, C.; Theivanayagam, M. G.; Applestone, D.; Dylla, A. G.; Manthiram, A.; Henkelman, G.; Goodenough, J. B.; Stevenson, K. J. In situ Raman spectroscopy of $LiFePO_4$: size and morphology dependence during charge and self-discharge. *Nanotechnology* **2013**, *24*, 424009.

(68) Hautier, G.; Jain, A.; Ong, S. P.; Kang, B.; Moore, C.; Doe, R.; Ceder, G. Phosphates as Lithium-Ion Battery Cathodes: An Evaluation Based on High-Throughput ab Initio Calculations. *Chem. Mater.* **2011**, *23*, 3495–3508.

(69) Allen, J. L.; Allen, J. L.; Delp, S. A.; Jow, T. R. Electrolyte Optimization of a Substituted-$LiCo_{1-x}Fe_xPO_4$ Cathode. *ECS Trans.* **2014**, *61* (27), 63–68.

(70) Han, D. W.; Kang, Y. M.; Yin, R. Z.; Song, M. S.; Kwon, H. S. Effects of Fe doping on the electrochemical performance of $LiCoPO_4$/C composites for high power-density cathode materials. *Electrochem. commun.* **2009**, *11* (1), 137–140.

(71) Wang, F.; Yang, J.; NuLi, Y.; Wang, J. Highly promoted electrochemical performance of 5 V $LiCoPO_4$ cathode material by addition of vanadium. *J. Power Sources* **2010**, *195* (19), 6884–6887.

(72) Xing, L. Y.; Hu, M.; Tang, Q.; Wei, J. P.; Qin, X.; Zhou, Z. Improved cyclic performances of $LiCoPO_4$/C cathode materials for high-cell-potential lithium-ion batteries with thiophene as an electrolyte additive. *Electrochim. Acta* **2012**, *59*, 172–178.

(73) Wolfenstine, J.; Read, J.; Allen, J. L. Effect of carbon on the electronic conductivity and discharge capacity $LiCoPO_4$. *J. Power Sources* **2007**, *163*, 1070–1073.

(74) Yamada, a.; Chung, S. C.; Hinokuma, K. Optimized $LiFePO_4$ for Lithium Battery Cathodes. *J. Electrochem. Soc.* **2001**, *148* (3), A224–A229.

(75) Herle, P. S.; Ellis, B.; Coombs, N.; Nazar, L. F. Nano-network electronic conduction in iron and nickel olivine phosphates. *Nat. Mater.* **2004**, *3*, 147–152.

(76) Harrison, K. L.; Manthiram, A. Microwave-assisted solvothermal synthesis and characterization of various polymorphs of $LiVOPO_4$. *Chem. Mater.* **2013**, *25*, 1751–1760.

(77) Harrison, K. L.; Bridges, C. a; Paranthaman, M. P.; Segre, C. U.; Katsoudas, J.; Maroni, V. a; Idrobo, J. C.; Goodenough, J. B.; Manthiram, A. Temperature Dependence of Aliovalent-Vanadium Doping in $LiFePO_4$ Cathodes. *Chem. Mater.* **2013**, *25*, 768–781.

(78) Omenya, F.; Chernova, N. a.; Zhang, R.; Fang, J.; Huang, Y.; Cohen, F.; Dobrzynski, N.; Senanayake, S.; Xu, W.; Whittingham, M. S. Why substitution enhances the reactivity of $LiFePO_4$. *Chem. Mater.* **2013**, *25*, 85–89.

(79) Gutierrez, A.; Qiao, R.; Wang, L.; Yang, W.; Wang, F.; Manthiram, A. High-Capacity, Aliovalently Doped Olivine $LiMn_{1-3x/2}V_xPO_4$ Cathodes without carbon coating. *Chem. Mater.* **2014**, *4* (26), 3018–3026.

(80) Kreder, K. J.; Assat, G.; Manthiram, A. Microwave-Assisted Solvothermal Synthesis of Three Polymorphs of $LiCoPO_4$ and Their Electrochemical Properties. *Chem. Mater.* **2015**, *27* (16), 5543–5549.

(81) Assat, G.; Manthiram, A. Rapid Microwave-Assisted Solvothermal Synthesis of Non-Olivine Cmcm Polymorphs of $LiMPO_4$ (M = Mn, Fe, Co, and Ni) at Low Temperature and Pressure. *Inorg. Chem.* **2015**, *54* (20), 10015–10022.

(82) Omenya, F.; Chernova, N. a.; Upreti, S.; Zavalij, P. Y.; Nam, K.-W.; Yang, X.-Q.; Whittingham, M. S. Can Vanadium Be Substituted into $LiFePO_4$? *Chem. Mater.* **2011**, *23*, 4733–4740.

(83) Ma, J.; Li, B.; Du, H.; Xu, C.; Kang, F. The Effect of Vanadium on Physicochemical and Electrochemical Performances of $LiFePO_4$ Cathode for Lithium Battery. *J. Electrochem. Soc.* **2011**, *158*, A26.

(84) Chung, S.-Y.; Chiang, Y.-M. Microscale Measurements of the Electrical Conductivity of Doped $LiFePO_4$. *Electrochem. Solid-State Lett.* **2003**, *6* (12), A278.

(85) Wolfenstine, J. Electrical conductivity of doped $LiCoPO_4$. *J. Power Sources* **2006**, *158* (2 SPEC. ISS.), 1431–1435.

(86) Huang, X.; Ma, J.; Wu, P.; Hu, Y.; Dai, J.; Zhu, Z.; Chen, H.; Wang, H. Hydrothermal synthesis of $LiCoPO_4$ cathode materials for rechargeable lithium ion batteries. *Mater. Lett.* **2005**, *59* (3), 578–582.

(87) Rogers, R. E.; Clarke, G. M.; Matthew, O. N.; Ganter, M. J.; DiLeo, R. a.; Staub, J. W.; Forney, M. W.; Landi, B. J. Impact of microwave synthesis conditions on the rechargeable capacity of $LiCoPO_4$ for lithium ion batteries. *J. Appl. Electrochem.* **2013**, *43*, 271–278.

(88) Allen, J. L.; Allen, J. L.; Thompson, T.; Delp, S. A.; Wolfenstine, J.; Jow, T. R. Cr and Si Substituted-$LiCo_{0.9}Fe_{0.1}PO_4$: Structure, full and half Li-ion cell performance. *J. Power Sources* **2016**, *327*, 229–234.

(89) Kreder, K. J.; Assat, G.; Manthiram, A. Aliovalent Substitution of V^{3+} for Co^{2+} in $LiCoPO_4$ by a Low-Temperature Microwave-Assisted Solvothermal Process. *Chem. Mater.* **2016**, *28* (6), 1847–1853.

(90) Vetter, J.; Novak, P.; Wagner, M. R.; Veit, C.; Moller, K. C.; Besenhard, J. O.; Winter, M.; Wohlfahrt-Mehrens, M.; Vogler, C.; Hammouche, A. Ageing mechanisms in lithium-ion batteries. *J. Power Sources* **2005**, *147* (1–2), 269–281.

(91) Aurbach, D.; Markovsky, B.; Levi, M. .; Levi, E.; Schechter, A.; Moshkovich, M.; Cohen, Y. New insights into the interactions between electrode materials and electrolyte solutions for advanced nonaqueous batteries. *J. Power Sources* **1999**,

81–82, 95–111.

(92) Zhang, S. S. A review on electrolyte additives for lithium-ion batteries. *J. Power Sources* **2006**, *162* (2 SPEC. ISS.), 1379–1394.

(93) Aono, H. Ionic Conductivity of Solid Electrolytes Based on Lithium Titanium Phosphate. *J. Electrochem. Soc.* **1990**, *137* (4), 1023.

(94) Aono, H.; Sugimoto, E.; Sadaoka, Y.; Imanaka, N.; Adachi, G. The Electrical Properties of Ceramic Electrolytes for $LiM_xTi_{2-x}(PO_4)_3 + yLi_2O$, M = Ge, Sn, Hf, and Zr Systems. *Electrochem. Sci. Technol.* **1993**, *140*, 1827–1832.

(95) Ishikawa, M.; Sugimoto, T.; Kikuta, M.; Ishiko, E.; Kono, M. Pure ionic liquid electrolytes compatible with a graphitized carbon negative electrode in rechargeable lithium-ion batteries. *J. Power Sources* **2006**, *162* (1), 658–662.

(96) Armand, M.; Endres, F.; MacFarlane, D. R.; Ohno, H.; Scrosati, B. Ionic-liquid materials for the electrochemical challenges of the future. *Nat. Mater.* **2009**, *8* (8), 621–629.

(97) Armand, M.; Tarascon, J.-M. Building better batteries. *Nature* **2008**, *451* (7179), 652–657.

(98) Edström, K.; Herstedt, M.; Abraham, D. P. A new look at the solid electrolyte interphase on graphite anodes in Li-ion batteries. *J. Power Sources* **2006**, *153* (2), 380–384.

(99) Sengwa, R. J.; Kaur, K.; Chaudhary, R. Dielectric properties of low molecular weight poly (ethylene glycol) s. *Polym Int* **2000**, *608* (January), 599–608.

(100) Prabu, M.; Selvasekarapandian, S.; Reddy, M. V.; Chowdari, B. V. R. Impedance studies on the 5-V cathode material, $LiCoPO_4$. *J. Solid State Electrochem.* **2012**, *16* (5), 1833–1839.

(101) Bramnik, N. N.; Nikolowski, K.; Trots, D. M.; Ehrenberg, H. Thermal Stability of

$LiCoPO_4$ Cathodes. *Electrochem. Solid-State Lett.* **2008**, *11*, A89.

(102) Taberna, P. L.; Mitra, S.; Poizot, P.; Simon, P.; Tarascon, J.-M. High rate capabilities Fe_3O_4-based Cu nano-architectured electrodes for lithium-ion battery applications. *Nat. Mater.* **2006**, *5* (7), 567–573.

(103) Zhang, H.; Yu, X.; Braun, P. V. Three-dimensional bicontinuous ultrafast-charge and -discharge bulk battery electrodes. *Nat. Nanotechnol.* **2011**, *6* (5), 277–281.

(104) Gowda, S. R.; Leela, A.; Reddy, M.; Pushparaj, V.; Herle, S.; Gopalakrishnan, K.; Gordon, J.; Gullapalli, H.; Zhan, X.; Ajayan, P. M. Three dimensionally engineered porous silicon electrodes for Li ion battery Three dimensionally engineered porous silicon electrodes for Li ion battery. *Nano Lett.* **2012**, *12*, 6060–6065.

(105) Arthur, T. S.; Bates, D. J.; Cirigliano, N.; Johnson, D. C.; Malati, P.; Mosby, J. M.; Perre, E.; Rawls, M. T.; Prieto, A. L.; Dunn, B. Three-dimensional electrodes and battery architectures. *MRS Bull.* **2011**, *36* (7), 523–531.

(106) Pikul, J. H.; Gang Zhang, H.; Cho, J.; Braun, P. V; King, W. P. High-power lithium ion microbatteries from interdigitated three-dimensional bicontinuous nanoporous electrodes. *Nat. Commun.* **2013**, *4*, 1732.

(107) Yang, G. F.; Song, J. S.; Kim, H. Y.; Joo, S. K. Metal Foam as Positive Electrode Current Collector for $LiFePO_4$ -Based Li-Ion Battery. *Jpn. J. Appl. Phys.* **2013**, *52* (10S), 10MB13.

(108) Zhou, C.; Zhang, Y.; Li, Y.; Liu, J. Construction of High-Capacitance 3D CoO@Polypyrrole Nanowire Array Electrode for Aqueous Asymmetric Supercapacitor. *Nano Lett.* **2013**, *13*, 2078–2085.

(109) Xiao, J.; Wan, L.; Yang, S.; Xiao, F.; Wang, S. Design hierarchical electrodes with highly conductive $NiCo_2S_4$ nanotube arrays grown on carbon fiber paper for high-performance pseudocapacitors. *Nano Lett.* **2014**, *14* (2), 831–838.

(110) Wei, D.; Scherer, M. R. J.; Bower, C.; Andrew, P.; Ryhanen, T.; Steiner, U. A nanostructured electrochromic supercapacitor. *Nano Lett.* **2012**, *12* (4), 1857–1862.

(111) Wang, Y.; Wang, G.; Wang, H.; Cai, W.; Zhang, L. One-pot synthesis of nanotube-based hierarchical copper silicate hollow spheres. *Chem. Commun. (Camb).* **2008**, *2* (48), 6555–6557.

(112) Zhang, H.; Braun, P. V. Three-Dimensional Metal Scaffold Supported Bicontinuous Silicon Battery Anodes. *Nano Lett.* **2012**, *12*, 2778–2783.

(113) Notten, P. H. L.; Roozeboom, F.; Niessen, R. A. H.; Baggetto, L. 3-D integrated all-solid-state rechargeable batteries. *Adv. Mater.* **2007**, *19* (24), 4564–4567.

(114) Chamran, F.; Yeh, Y.; Min, H. S.; Dunn, B.; Kim, C. J. Fabrication of high-aspect-ratio electrode arrays for three-dimensional microbatteries. *J. Microelectromechanical Syst.* **2007**, *16* (4), 844–852.

(115) Min, H. S.; Park, B. Y.; Taherabadi, L.; Wang, C.; Yeh, Y.; Zaouk, R.; Madou, M. J.; Dunn, B. Fabrication and properties of a carbon/polypyrrole three-dimensional microbattery. *J. Power Sources* **2008**, *178* (2), 795–800.

(116) Keiji Nagai, Daisuke Wada, Mitsuo Nakai, T. N. Electrochemical Fabrication of Low Density Metal Foam with Mono-dispersed-sized Micro- and Submicro-Meter Pore. *Fusion Sci. Technol.* **2009**, *49*, 686–690.

(117) Tappan, B. C.; Huynh, M. H.; Hiskey, M. A.; Chavez, D. E.; Luther, E. P.; Mang, J. T.; Son, S. F. Ultralow-Density Nanostructured Metal Foams : Combustion Synthesis, Morphology, and Composition. *J. Am. Chem. Soc.* **2006**, *128*, 6589–6594.

(118) Bryce C, T.; Stephen A, S.; Luther, E. P. Nanoporous metal foams. *Angewandte Chemie - International Edition*. 2010, pp 4544–4565.

(119) Walsh, D.; Arcelli, L.; Ikoma, T.; Tanaka, J.; Mann, S. Dextran templating for the

synthesis of metallic and metal oxide sponges. *Nat. Mater.* **2003**, *2* (6), 386–390.

(120) Jiang, P.; Cizeron, J.; Bertone, J. F.; Colvin, V. L. Preparation of macroporous metal films from colloidal crystals. *Journal of the American Chemical Society*. 1999, 7957–7958.

(121) Yan, H.; Blanford, C. F.; Holland, B. T.; Parent, M.; Smyrl, W. H.; Stein, A. Chemical synthesis of periodic macroporous NiO and metallic Ni. *Adv. Mater.* **1999**, *11* (12), 1003–1006.

(122) Erlebacher, J.; Aziz, M. J.; Karma, a; Dimitrov, N.; Sieradzki, K. Evolution of nanoporosity in dealloying. *Nature* **2001**, *410* (6827), 450–453.

(123) Ding, Y.; Erlebacher, J. Nanoporous metals with controlled multimodal pore size distribution. *J. Am. Chem. Soc.* **2003**, *125* (26), 7772–7773.

(124) Leventis, N.; Chandrasekaran, N.; Sotiriou-Leventis, C.; Mumtaz, A. Smelting in the age of nano: iron aerogels. *J. Mater. Chem.* **2009**, *19* (1), 63–65.

(125) Friedrich, M.; Gálvez-Ruiz, J. C.; Klapötke, T. M.; Mayer, P.; Weber, B.; Weigand, J. J. BTA copper complexes. *Inorg. Chem.* **2005**, *44* (22), 8044–8052.

(126) Geisberger, G.; Klapötke, T. M.; Stierstorfer, J. Copper bis(1-methyl-5-nitriminotetrazolate): A promising new primary explosive. *Eur. J. Inorg. Chem.* **2007**, No. 30, 4743–4750.

(127) Hammerl, A.; Holl, G.; Kaiser, M.; Klapötke, T. M.; Mayer, P.; Nöth, H.; Piotrowski, H.; Suter, M. New hydrazinium salts of 5,5'-azotetrazolate. *Zeitschrift fur Naturforsch. - Sect. B J. Chem. Sci.* **2001**, *56* (9), 857–870.

(128) Zhou, W.; Zheng, K.; He, L.; Wang, R.; Guo, L.; Chen, C.; Han, X.; Zhang, Z. Ni/Ni3C core-shell nanochains and its magnetic properties: One-step synthesis at low temperature. *Nano Lett.* **2008**, *8* (4), 1147–1152.

(129) Wang, C.; Han, X.; Zhang, X.; Hu, S.; Zhang, T.; Wang, J.; Du, Y.; Wang, X.; Xu, P.

Controlled synthesis and morphology-dependent electromagnetic properties of hierarchical cobalt assemblies. *J. Phys. Chem. C* **2010**, *114* (35), 14826–14830.

(130) Liu, W.; Herrmann, A. K.; Bigall, N. C.; Rodriguez, P.; Wen, D.; Oezaslan, M.; Schmidt, T. J.; Gaponik, N.; Eychmuller, A. Noble metal aerogels-synthesis, characterization, and application as electrocatalysts. *Acc. Chem. Res.* **2015**, *48* (2), 154–162.

(131) Dong, H.; Chen, Y.; Feldmann, C. Polyol synthesis of nanoparticles: status and options regarding metals, oxides, chalcogenides, and non-metal elements. *Green Chem.* **2015**, *17*, 4107–4132.

(132) Luo, X.; Chen, Y.; Yue, G. H.; Peng, D. L.; Luo, X. Preparation of hexagonal close-packed nickel nanoparticles via a thermal decomposition approach using nickel acetate tetrahydrate as a precursor. *J. Alloys Compd.* **2009**, *476* (1–2), 864–868.

(133) Corporation, E. A. ERG Duocel - Surface Areas http://www.ergaerospace.com/surface-area.html (accessed Jan 8, 2016).

(134) Erri, P.; Nader, J.; Varma, A. Controlling combustion wave propagation for transition metal/alloy/cermet foam synthesis. *Adv. Mater.* **2008**, *20* (7), 1243–1245.

(135) Derrien, B. G.; Hassoun, J.; Panero, S.; Scrosati, B. Nanostructured Sn – C Composite as an Advanced Anode Material in High-Performance Lithium-Ion Batteries. *Adv. Mater.* **2007**, *19*, 2336–2340.

(136) Cao, F. F.; Deng, J. W.; Xin, S.; Ji, H. X.; Schmidt, O. G.; Wan, L. J.; Guo, Y. G. Cu-Si nanocable arrays as high-rate anode materials for lithium-ion batteries. *Adv. Mater.* **2011**, *23* (38), 4415–4420.

(137) Kreder, K. J.; Manthiram, A. Metal nanofoams via a facile microwave-assisted solvothermal process. *Chem. Commun.* **2017**, *53*, 865–868.

(138) Xia, X.; Leo, C. V. Di; Gu, X. W.; Greer, J. R. In Situ Lithiation − Delithiation of Mechanically Robust Cu-Si Core-Shell Nanolattices in a Scanning Electron Microscope. *ACS Energy Lett.* **2016**, *1*, 492–499.

(139) Ulus, A.; Rosenberg, Y.; Burstein, L.; Peled, E. Tin Alloy-Graphite Composite Anode for Lithium-Ion Batteries. *J. Electrochem. Soc.* **2002**, *149* (5), A635–A643.

(140) Wang, Y.; Lee, J. Y.; Deivaraj, T. C. Tin Nanoparticle Loaded Graphite Anodes for Li-Ion Battery Applications. *J. Electrochem. Soc.* **2004**, *151* (11), A1804–A1809.

(141) Kumar, T. P.; Ramesh, R.; Lin, Y. Y.; Fey, G. T. Tin-filled carbon nanotubes as insertion anode materials for lithium-ion batteries. *Electrochem. commun.* **2004**, *6*, 520–525.

(142) Ng, S.; Wang, J.; Wexler, D.; Konstantinov, K.; Guo, Z. Highly Reversible Lithium Storage in Spheroidal Carbon-Coated Silicon Nanocomposites as Anodes for Lithium-Ion Batteries. *Angew. Chemie* **2006**, *45*, 6896–6899.

(143) Chan, C. K.; Peng, H.; Liu, G. A. O.; Mcilwrath, K.; Zhang, X. F.; Huggins, R. A.; Cui, Y. I. High-performance lithium battery anodes using silicon nanowires. *Nat. Nanotechnol.* **2008**, *3*, 31–35.

(144) Zhang, X.; Patil, P. K.; Wang, C.; Appleby, A. J.; Little, F. E.; Cocke, D. L. Electrochemical performance of lithium ion battery, nano-silicon-based, disordered carbon composite anodes with different microstructures. *J. Power Sources* **2004**, *125*, 206–213.

(145) Guo, Z. P.; Milin, E.; Wang, J. Z.; Chen, J.; Liu, H. K. Silicon / Disordered Carbon Nanocomposites for Lithium-Ion Battery Anodes. *J. Electrochem. Soc.* **2005**, *152* (11), A2211–A2216.

(146) Hu, R.; Shi, Q.; Wang, H.; Zeng, M.; Zhu, M. Influences of Composition on the Electrochemical Performance in Immiscible Sn - Al Thin Films as Anodes for Lithium Ion Batteries. *J. Phys. Chem. C* **2009**, *113*, 18953–18961.

(147) Wang, J.; Wang, Y.; Zhang, P.; Zhang, D.; Ren, X. Preparation and electrochemical properties of binary Si_xSb immiscible alloy for lithium ion batteries. *J. Alloys Compd.* **2014**, *610*, 308–314.

(148) Yang, J.; Winter, M.; Besenhard, J. O. Small particle size multiphase Li-alloy anodes for lithium-ion- batteries. *Solid State Ionics* **1996**, *90*, 281–287.

(149) Kuksenko, S. P. Aluminum Foil as Anode Material of Lithium – Ion Batteries : Effect of Electrolyte Compositions on Cycling Parameters. *Russ. J. Electrochem.* **2013**, *49* (1), 67–75.

(150) Nyholm, L.; Oltean, G.; Tai, C.; Edstr, K. On the origin of the capacity fading for aluminium negative electrodes in Li-ion batteries. *J. Power Sources* **2014**, *269*, 266–273.

(151) Ji, B.; Zhang, F.; Sheng, M.; Tong, X.; Tang, Y. A Novel and Generalized Lithium-Ion-Battery Configuration utilizing Al Foil as Both Anode and Current Collector for Enhanced Energy Density. *Adv. Mater.* **2016**, *29* (7), 1–7.

(152) Woo, S.; Mcdowell, M. T.; Berla, L. A.; Nix, W. D.; Cui, Y. Fracture of crystalline silicon nanopillars during electrochemical lithium insertion. *Proc. Natl. Acad. Sci.* **2012**, *109* (11), 4080–4085.

(153) Wood, D. L.; Li, J.; Daniel, C. Prospects for reducing the processing cost of lithium ion batteries. *J. Power Sources* **2015**, *275*, 234–242.

Vita

Karl Kreder was born in Honolulu, Hawaii. In 2008 he graduated from Purdue University with a Bachelor's degree in Mechanical engineering. Subsequently, he moved to San Antonio, TX where he worked for Southwest Research Institute (SwRI) as a Research Engineer. At Southwest Research Institute he started the Energy Storage System Evaluation and Safety consortium which performed testing, characterization, and research on large format lithium ion batteries for >10 KWH energy storage. In 2012, he joined Dr. Arumugam Manthiram's research group at the University of Texas at Austin pursuing his doctoral degree. His research focused on the developing new materials to improve the performance of lithium ion batteries.

Email Address: karl.kreder@gmail.com

This dissertation was typed by the author.